Lawrence Berkeley National Laboratory

Final Report

Delayed Gamma-Ray Spectroscopy for Non-Destructive Assay of Nuclear Materials

Project: LB12-DelayedGamma-PD2Lb

Bernhard Ludewigt
Lawrence Berkeley National Laboratory

Vladimir Mozin
Lawrence Livermore National Laboratory

Luke Campbell
Pacific Northwest National Laboratory

Andrea Favalli
Los Alamos National Laboratory

Alan W. Hunt, Edward T.E. Reedy, Heather A. Seipel
Idaho State University

Submitted to the

Office of Defense Nuclear Nonproliferation Research and Development (NA-22)
National Nuclear Security Administration

June, 2015

Disclaimers

Copyright Notice

Summary

High-energy, beta-delayed gamma-ray spectroscopy is a potential, non-destructive assay techniques for the independent verification of declared quantities of special nuclear materials at key stages of the fuel cycle and for directly assaying nuclear material inventories for spent fuel handling, interim storage, reprocessing facilities, repository sites, and final disposal. Other potential applications include determination of MOX fuel composition, characterization of nuclear waste packages, and challenges in homeland security and arms control verification. Neutron induced fission generates a distribution of short-lived fission fragments with half-lives ranging from seconds and to tens of minutes providing "fingerprints" of the fissioning isotopes. Each fissionable isotope produces characteristic relative peak intensities so that the measured delayed gamma-ray spectrum can be analyzed as a superposition of contributions from individual isotopes. Isotopic fractions can determined if the response spectra of the individual isotopes are accurately known.

This project has been a collaborative effort of researchers from four National Laboratories, Lawrence Berkley National Laboratory (LBNL), Lawrence Livermore National Laboratory (LLNL), Los Alamos National Laboratory (LANL), Pacific Northwest National Laboratory (PNNL), and Idaho State University's (ISU) Idaho Accelerator Center (IAC). Experimental measurements at the Oregon State University (OSU) were also supported. The research included two key components, a strong experimental campaign to characterize the delayed gamma-ray signatures of the isotopes of interests and of combined targets, and a closely linked modeling effort to assess system designs and applications. Experimental measurements were performed to evaluate fission fragment yields, to test methods for determining isotopic fractions, and to benchmark the modeling code package. Detailed signature knowledge is essential for analyzing the capabilities of the delayed gamma technique, optimizing measurement parameters, and specifying neutron source and gamma-ray detection system requirements. The research was divided into three tasks: experimental measurements, characterization of fission yields, and development of analysis methods (task 1), modeling in support of experiment design and analysis and for the assessment of applications (task 2), and high-rate gamma-ray detector studies (task 3).

Experimental measurement campaigns were carried out at the IAC using a photo-neutron source and at OSU using a thermal neutron beam from the TRIGA reactor to characterize the emission of high-energy delayed gamma rays from ^{235}U, ^{239}Pu, and ^{241}Pu targets following neutron induced fission. Data were collected for pure and combined targets for several irradiation/spectroscopy cycle times ranging from 10/10 seconds to 15/30 minutes. The IAC data including raw list-mode data, accumulated spectra, laboratory notebooks and other ancillary data, are available to team members and other researchers for analysis. A plethora of delayed gamma-ray lines from short-lived fission products was identified in the 3-6 MeV energy range and examined for potential use in delayed gamma assays. The ^{235}U/^{239}Pu line ratios vary considerably with several lines much stronger for ^{235}U fission. For shorter irradiation/spectroscopy periods two lines of ^{106}Tc with a half-life of 36 s are prominent in the ^{239}Pu spectra but nearly absent in the ^{235}U spectra and thus a strong indicator of ^{239}Pu fission. For best utilization of delayed gamma-rays from fragments with short half-lives and for maximizing the sensitivity of a ^{235}U/^{239}Pu measurement, 1 to 2 minutes long irradiation/spectroscopy periods appear optimal.

The delayed gamma-ray signature of ^{241}Pu, a significant fissile constituent in spent fuel, was measured and compared to ^{239}Pu. The ^{241}Pu/^{239}Pu ratios varied between 0.5 and 1.2 for ten prominent lines in the 2700-3600 keV energy range. Such significant differences in relative peak intensities make it possible to determine relative fractions of these isotopes in a mixed sample. Also measured were combined ^{235}U, ^{239}Pu, and ^{241}Pu targets to experimentally test the sensitivities of a delayed gamma assay.

A method for determining fission product yields by fitting the energy and time dependence of the delayed gamma-ray emission was developed and demonstrated on a limited ^{235}U data set. Significant discrepancies with values in the ENDF/B-VII.1 nuclear data library were found. Future work should include fitting more data sets over larger energy ranges to reduce uncertainties in the extracted fission yields. By applying the fitting procedure to the full energy and temporal range of the measured data, improved fission product yields could be obtained for all three isotopes, ^{235}U, ^{239}Pu, and ^{241}Pu.

De-convolution methods for determining fissile fractions were developed and tested on the experimental data. Using a set of selected well-identified peaks above 3 MeV yielded good results, whereas spectral component analysis methods using larger sections of the delayed gamma spectra to lower statistical uncertainties suffered from systematic errors.

The use of high count-rate LaBr$_3$ detectors was investigated as a potential alternative to HPGe detectors for delayed gamma-ray spectroscopy in applications, where the high count-rate capability may outweigh the lower energy resolution. Characterization of gamma-ray spectroscopy with a LaBr$_3$ scintillation detector found excellent spectroscopic performance at count-rates exceeding 2 Mcps. Measured ^{235}U and ^{239}Pu delayed gamma-ray spectra exhibited significant differences in relative peak intensities indicating the possible use of LaBr$_3$ detector for delayed gamma assay but further assessment of measurement sensitivities and systematic uncertainties is needed.

Modeling capabilities were added to an existing framework and codes were adapted as needed for analyzing experiments and assessing application-specific assay concepts including simulation of measurements over many short irradiation/spectroscopy cycles. The code package was benchmarked against the data collected at the IAC for small targets and the assembly-scale data collected at LANL. A study of delayed gamma-ray spectroscopy for nuclear safeguards was performed for a variety of assemblies in the extensive NGSI spent fuel library. The modeling results indicate that delayed gamma-ray responses can be collected from spent fuel assemblies with statistical quality sufficient for analyzing their isotopic composition using a 10^{11} n/s neutron generator and COTS detector instrumentation.

A de-convolution analysis of the delayed gamma-ray response spectra modeled for spent fuel assemblies was performed using the same method that was applied to the experimental spectra. At least 12 DG peaks in the energy region between 3 and 4.5 MeV were identified as sensitive to the fissionable isotopic content of the fuel and modeled assay results were processed to determine the relative fissile isotopic compositions. The baseline de-convolution algorithm was calibrated assuming preliminary measurements of fresh LEU and MOX assemblies with known fissile material compositions. The analysis method demonstrates that assembly-averaged relative fissile isotopic fractions in measured fuel assemblies can be determined with uncertainties on the order of 10% for Pu-239 and U-235. A major contribution to the uncertainty can be attributed to the fact that the detectors are mostly sensitive to the outer few rows of pins while the burnup and thus the isotopic concentrations may vary considerably across an assembly. For the simulated measurements on model assemblies of the NGSI Spent Fuel Libraries, uncertainties in the U-235, Pu-239, and Pu-241 relative abundances were approximately 5% when averaged over all detector positions around an assembly. Overall, high-energy, β-delayed gamma-ray spectroscopy has been shown to be a potential method for determining the relative fissile content of spent nuclear fuel assemblies, and special nuclear materials in general. Although the methodology for the absolute normalization of the delayed gamma-ray response may not be straightforward, this technique may be used in combination with other measurements in an effort to achieve detailed fissile material composition characterization.

Acknowledgements

Table of Content

I. Introduction

The project titled "Delayed Gamma-ray Spectroscopy for Non-Destructive Assay of Nuclear Materials" has been a collaborative effort of researchers from four National Laboratories, Lawrence Berkley National Laboratory (LBNL), Lawrence Livermore National Laboratory (LLNL), Los Alamos National Laboratory (LANL), Pacific Northwest National Laboratory (PNNL), and Idaho State University's (ISU) Idaho Accelerator Center (IAC). The study addressed the need for improved non-destructive assay techniques for quantifying the actinide composition of spent nuclear fuel and for the independent verification of declared quantities of special nuclear materials at key stages of the fuel cycle. High-energy, delayed gamma-ray spectroscopy following neutron irradiation is a potential technique for directly assaying spent fuel assemblies and achieving the safeguards goal of quantifying nuclear material inventories for spent fuel handling, interim storage, reprocessing facilities, repository sites, and final disposal. Other potential applications include determination of MOX fuel composition, characterization of nuclear waste packages, and challenges in homeland security and arms control verification.

In active interrogation techniques neutrons or photons are used to probe materials containing fissionable isotopes. Induced fission reactions produce highly excited fission fragment that emit prompt secondary radiation in the first $\sim 10^{-12}$ s and beta-delayed neutrons and gamma rays over much longer time periods. While delayed gamma-rays from long-lived fission fragments have long been used in safeguards applications, actively inducing fission opens up the use of delayed gamma-rays from short lived fission fragments with half-live ranging from seconds and to tens of minutes. [1]. Delayed gamma-ray spectroscopy is especially interesting for safeguards applications because the emission spectra provide fingerprints of the various fissioning isotopes. Each fissionable isotope produces characteristic relative peak intensities so that the delayed gamma-ray spectrum can be analyzed as a superposition of contributions from individual isotopes, e.g., ^{235}U, ^{239}Pu, ^{241}Pu and ^{238}U in spent fuel, and the isotopic fractions determined if the delayed gamma-ray spectra of the individual isotopes are accurately known. The gamma-rays from the short lived fragments tend to have higher energies that extend far beyond the intense passive background from long-lived fission products in, for example, spent nuclear fuel, making a delayed gamma assay possible. [2].

The objective of this project was to develop delayed gamma-ray spectroscopy and to assess the potential and merits of the method in safeguards. The research had two key components: a strong experimental campaign to characterize the delayed gamma-ray signatures for specific isotopes and combined targets, and a closely linked modeling effort to assess system designs and applications. Experimental data were collected to determine relative fission yields, to evaluate nuclear data libraries for gaps and accuracy, to test de-convolution methods for determining isotopic fractions, and to validate modeling predictions. Detailed signature knowledge is essential for analyzing the delayed gamma technique and its capabilities, optimizing measurement parameters, and specifying neutron source and gamma-ray detection system.

The research was divided into three tasks:

Task 1 (Section II.) focused on the experimental measurement of the high-energy delayed gamma-ray emission of three fissile isotopes of interest in nuclear safeguards (^{235}U, ^{239}Pu, ^{241}Pu), combined targets, and a mockup fuel assembly. A method for determining fission yields by fitting measured time-energy dependent delayed gamma-ray emission data was developed, and methods for de-convolving delayed gamma-ray spectra and determining isotopic fractions were tested on combined target spectra.

Task 2 (Section III.) included development of modeling tools, simulations in support of the experimental program, and modeling and assessment of application specific delayed gamma-ray assay scenarios.

Task 3 (Section IV.) addressed the need for high-rate spectroscopy detectors for applications that involve highly radioactive materials, such as spent nuclear fuel. Fast LaBr$_3$ scintillation detectors were characterized and tested in delayed gamma experiments at the IAC and at LANL as a potential alternative to germanium detectors.

II. Experimental Delayed Gamma-ray Measurements

Several experimental campaigns were performed at the Idaho Accelerator Center (IAC), the Oregon State University (OSU), and at the Los Alamos National Laboratory (LANL):

- Sets of high-energy delayed gamma-ray spectra were collected at the IAC for ^{235}U, ^{238}U, ^{239}Pu, ^{241}Pu targets and combinations of these isotopes at irradiation/spectroscopy times ranging from 10/10 seconds to 15/30 minutes times.

- At OSU the short-lived delayed gamma-ray signatures of ^{235}U and ^{239}Pu were measured following irradiation in the purely thermal neutron beam from OSU's TRIGA reactor.

- A first experimental test of the delayed gamma technique at the assembly level was performed at LANL using a neutron generator and a mock-up assembly composed of enriched and depleted uranium pins.

The data analysis included the development of a method for determining relative fission yields by fitting time-dependent delayed-gamma emission data using maximum likelihood estimation. In addition, deconvolution methods for determining isotopic fractions from measured delayed-gamma spectra were developed and tested using the measured data.

Thermal neutron fission is dominant for the three fissile isotopes ^{235}U, ^{239}Pu and ^{241}Pu but strong resonances at 0.3 eV in both, ^{239}Pu and ^{241}Pu, contribute significantly to the fissions of these isotopes. Measurements on the fissile isotopes at both, purely thermal neutron energies (OSU TRIGA reactor) and at the IAC with a moderated neutron spectrum, similar to a reactor spectrum, may show differences due to resonance fission. Together, these measurements are expected to allow better characterization of thermal and resonance fission of the common fissile isotopes.

II.1. Experiments at the Idaho Accelerator Center (IAC)

The experimental tasks included six experimental campaigns in which delayed gamma-ray spectra from neutron-induced fission were experimentally measured. In all of these campaigns, the fissile targets consisted of ^{235}U, ^{239}Pu, ^{241}Pu and combinations of these isotopes. The spectroscopic data were collected with HPGe detectors for best energy resolution but LaBr$_3$ detectors were also tested in three of the experimental campaigns. The main objectives of the experimental and subsequent data analysis tasks were:
- **Observation and identification of discrete delayed gamma-rays from short-lived fragments**. Discrete delayed gamma-ray lines with energies greater than ~2.6 MeV were observed. The majority of the fission fragments that emit high-energy delayed gamma-rays tend to come from short-lived fission fragments (i.e. tens of minutes and less). Fission fragments were identified based on yields and gamma-ray branching ratios.
- **Fissile sensitivity of the discrete delayed gamma-rays**. Discrete delayed gamma-ray lines were sought that served as a particularly strong indicator of a specific isotope. While lines strongly indicating ^{235}U fission (e.g. ^{90}Rb) were readily seen in the initial

measurements, delayed gamma-rays lines that were significantly stronger for [239]Pu than [235]U were only found at the shorter irradiation/detection cycle times.

- **Irradiation/detection periods**. Delayed gamma data were collected at different irradiation/detection time periods included 15/30 min, 5/5 min, 90/90 s, 60/60 s and 10/10 s. For the three longest cycle times (15/30 min, 5/5 min and 90/90 s) the sample was shuttled between the irradiation and spectroscopy stations. For measurements at the shortest cycle times (60/60 s and 10/10 s) the detector was located adjacent to the sample in at the irradiation station (i.e. the sample was stationary).
- **Data analysis algorithms**. Data analysis algorithms were developed and tested for de-convoluting measured delayed gamma-ray spectra and determining fissile isotopic fractions.

In support of the primary objectives, an automated system was constructed to shuttle the samples from the irradiation position to the spectroscopy station in order to collect clean spectra for shorter irradiation/spectroscopy cycles. Furthermore, there was an ongoing effort to increase the data throughput and achieve higher count rate capabilities. Early in the project a faster analog data acquisition system was implemented and a digital data acquisition system was tested in the later campaigns.

II.1.1. Experimental Setup

The core components of the neutron irradiation setup used in all campaigns are seen in the schematic representation in Figure 1. A pulsed S-band radiofrequency linac produced 15 MeV electrons in 4 μs long pulses containing typically 120 to 145 nC of charge that impinged on a 2.2 mm tungsten bremsstrahlung radiator at repetition rates of 15 to 264 Hz. Electrons that were not absorbed in the radiator struck a 5.08 cm thick aluminum beam stop immediately following the radiator. The high-energy photon beam traversed through a 15.2 cm thick Pb collimator with a 6.03 cm inner diameter that was inset in a large lead wall that shielded the fissile target from direct bremsstrahlung photons to prevent photofission. The bremsstrahlung beam then impinged on a 25.4 cm thick and 8.9 cm diameter beryllium cylinder located 58.8 cm from the bremsstrahlung radiator. This Be neutron converter was surrounded by a large amount of neutron moderating C_2H_4 (polyethylene), measuring ~57.8 cm wide by ~40.6 cm deep and ~60 cm tall.

Within the neutron moderating polyethylene, the fissile targets were approximately centered on the detector side of the pile, ~17.5 cm from the Be neutron converter, as seen in Figure 1. The targets consisted of [235]U in uranium oxide pellets, [239]Pu in plutonium metal foils and [241]Pu in oxidized Am/Pu metal lumps. The actinide isotopics and additional information for each fissile sample is presented in Table I. A total of six ~43% enriched uranium oxide pellets, with 464 mg of [235]U each, were available. These six pellets were placed in two small plastic vials with each vial containing three pellets. A total of nine [239]Pu metal disks were available with each disk containing ~970 mg of [239]Pu accounting for ~94% of the actinides in the sample. These disks were nuclear accident dosimeters (NADs) with the plutonium oxide clad in copper and each NAD was inside a plastic coin case [3]. The single [241]Pu sample consisted of oxidized Am/Pu metal lumps containing ~254 mg of [241]Pu. The [241]Pu accounted for only ~20% of the actinides in the sample; the dominate actinide was [241]Am accounting for ~65% of the actinides. The Pu/Am oxide was contained in a glass vial that was placed in an Al capsule, which was inside a steel container. Combinations of [235]U, [239]Pu and/or [241]Pu were created by varying the number of uranium oxide pellets and plutonium disks. For targets containing only [235]U and/or [239]Pu, a foam physical support kept the target's constituents within close proximity to each other, as seen in Figure 2 allowing it to be irradiated in a small compartment in the polyethylene moderation pile that was 2.5 cm wide by 20 cm long and 10 cm tall. When the target contained [241]Pu, additional fissile samples were directly attached to the

SADZ container. Since this container was considerably larger than the foam support, the irradiation compartment in the polyethylene moderation pile had to be increased to 10 cm wide by 20 cm long and 10 cm tall.
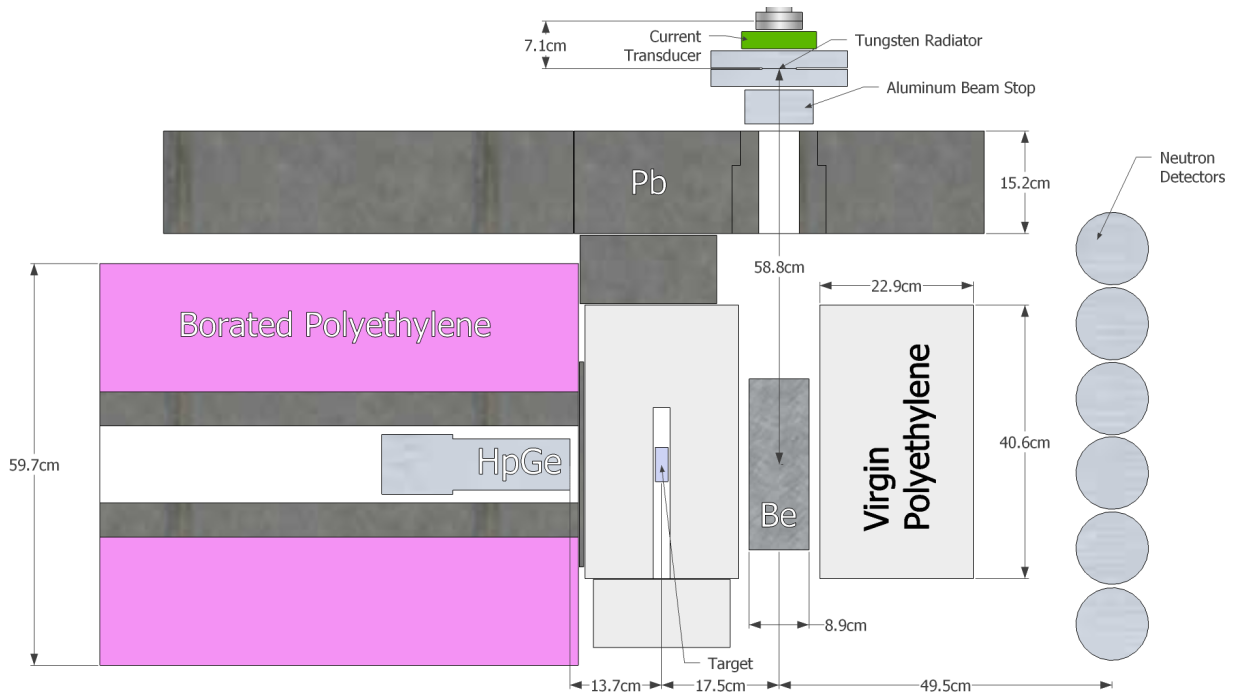
Figure 1. Schematic diagram of the experimental setup. The HPGe detector was positioned as shown in the diagram for the 60/60 s and 10/10 s irradiation/spectroscopy cycle times. For the 90/90 s, 5/5 min and 15/30 min measurements the 40% relative efficiency n-type HPGe detector was located behind a shielding wall in an adjacent room and the fissile target was shuttled to the detector after each irradiation period.

Figure 2. Schematic diagrams of the ^{235}U/^{239}Pu target with foam support.

Table I. Actinide isotopics and additional information for each of the fissile samples

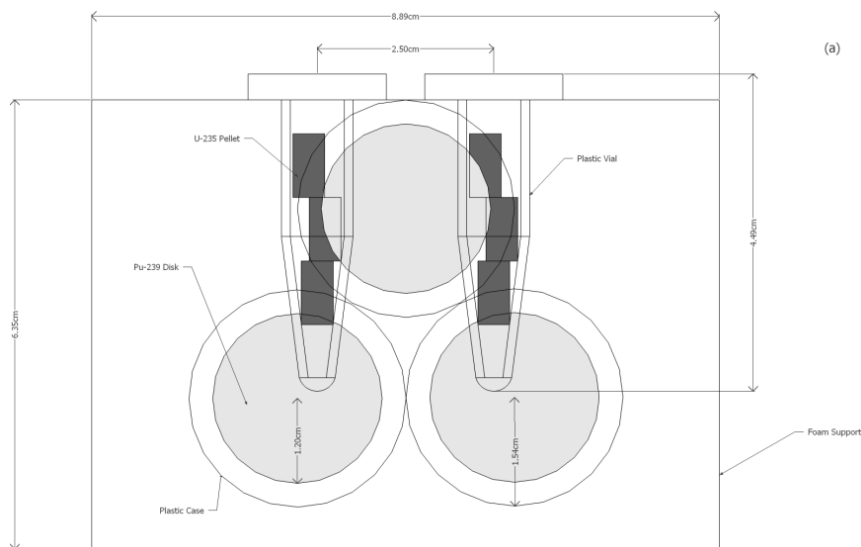|	^{235}U	^{239}Pu	^{241}Pu
Type	UO$_2$ pellet	PuO$_2$ NAD disks	Oxidized Pu/Am metal
Number available	6	12	1
Cladding	None	Cu	--
Sample diameter	3.2 mm	2.4 cm incl. cladding	--
Sample thickness	6.3 mm	1 mm incl. cladding	--
Container	Plastic vial	Plastic coin case	SADZ container
^{235}U	464 mg	--	--
^{238}U	623 mg	--	--
^{238}Pu	--	55.3 mg	--
^{239}Pu	--	974 mg	10.0 mg
^{240}Pu	--	55 mg	154.0 mg
^{241}Pu	--	383 mg	253.9 mg
^{242}Pu	--	--	26 mg
^{241}Am	--	3.6 mg	835.7 mg

The measurement cycles consisted of irradiation and detection periods of varied lengths separated by the sample transfer time. A total of five different inspection cycles were utilized:

- **15/30 min**. Irradiation period of 15 min followed by a 30 min detection period. Sample was manually shuttled from the irradiation position to the detection position.
- **5/5 min**. Irradiation period of 5 min followed by a 5 min detection period. Sample was mechanically shuttled from the irradiation position to the detection position.
- **90/90 s**. Irradiation period of 90 s followed by a 90 s detection period. Sample was mechanically shuttled from the irradiation position to the detection position.
- **60/60 s**. Irradiation period of 60 s followed by a 60 s detection period. Sample was stationary and the HPGe detector was in situ with the sample in the irradiation position.
- **10/10 s**. Irradiation period of 10 s followed by a 10 s detection period. Sample was stationary and the HPGe detector was in situ with the sample in the irradiation position.

For the 60/60 and 10/10 s irradiation/detection periods, the HPGe detector was only ~13.7 cm from the stationary sample, as seen in Figure 1. The 40% relative efficiency n-type HPGe detector was shielded by ~5.08 cm thick Pb rings from the intense high-energy photon pulse created when the electron beam struck the bremsstrahlung radiator. Nevertheless, the HPGe detector was saturated for ~350 ms after each pulse. The front face of the detector was covered by a 6.35 mm Pb filter to absorb low-energy photons emitted from the target and surrounding material. For the 15/30 min, 5/5 min and 90/90 s irradiation/spectroscopy measurements, the HPGe detector was located in a well-shielded experimental room and the sample was shuttled to the detector after the irradiation. The detector to sample distance was kept the same at ~13.7 cm. The transit time from the irradiation to the detection position varied from initially ~35 s to 18 s after improvements to the transfer system. The measurement cycles were repeated for total measurement times of two to four hours per target.

The backbone of the mechanical shuttle that was used in the 5/5 min and 90/90 s irradiation/detection periods was a rail system held ~1.5 m off the floor by aluminum stands as seen in Figure 3. A chain was pulled through the rail by a digitally controlled motor with a coupled encoder, providing positioning accuracy with a few hundred micrometers. The transfer cart holding the sample was attached to this chain (similar to a cable car) and hence moved with the

chain. The entire length of travel was ~10 m and this distance could initially be traveled in ~35 s. By adding a second motor power supply, modifying the motor control software and changing the gear ratios, the transfer time was decreased to ~18 s. The transfer cart and sample moved between the irradiation and detection positions under remote control, eliminating the need to enter the accelerator hall or spectroscopy room.

   In most of the experiments, the two preamplifier outputs from the HPGe detector were sent to an analog multi-parameter data acquisition system, which recorded both energy and time information in an event by event mode. One of the acquisition channels was configured for high-speed spectroscopy with a 3 µs time constant gated integrating amplifier and a 900 ns fixed dead-time analog to digital converter. The other acquisition channel used an amplifier with a 6 µs Gaussian shaping time and a 100 MHz Wilkinson analog to digital converter. The high-speed spectroscopy channel was able to handle data throughput rates in excess of 64k cps. In contrast, the slow channel could only handle data through put rates up to ~15k cps but provided better energy resolution. In addition to the detector information, a variety of timing data was also recorded including, time stamps from the accelerator gun trigger, end of irradiation period and end of travel. This allowed both, energy and time information of the gamma rays detected by the HPGe detector to be examined. In general, the data taken with the fast spectroscopy channel were used for analysis because dead times for the slow channel often exceeded 30% while providing only slightly better energy resolution.
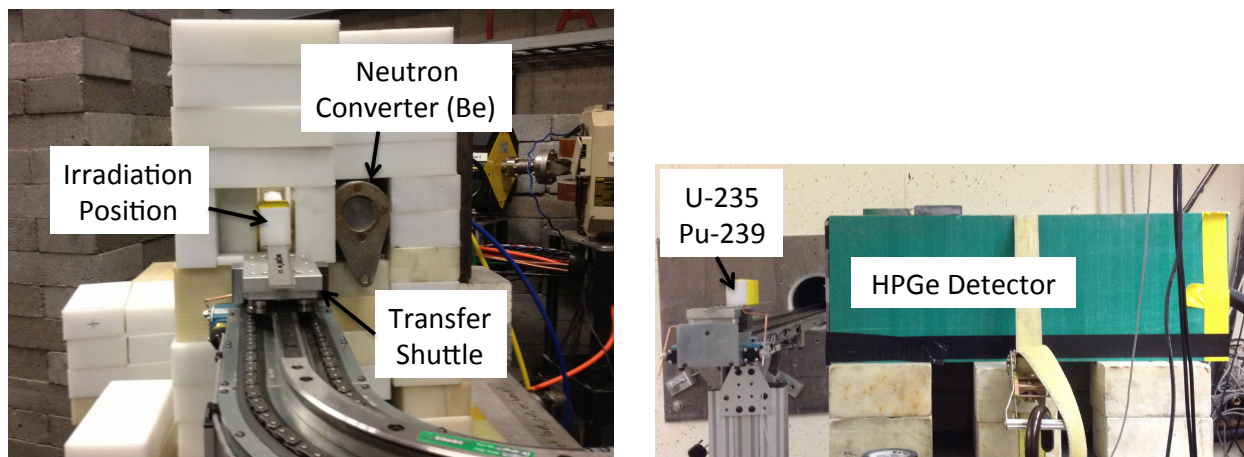

Figure 3. Experimental setup with the sample transfer system installed. On left: Irradiation station with the sample in irradiation position. On right: Spectroscopy station with sample positioned in front of the shielded HPGe detector. The sample is transported from the irradiation station to the measurement station via transfer rail through the hole in the ~1.8 m concrete wall that separates the accelerator hall and the spectroscopy station.

II.1.2. Delayed Gamma-ray Measurements on ^{235}U and ^{239}Pu Targets

   Data sets for irradiation/detection periods of 10/10 s, 60/60 s, 90/90 s, 5/5 min and 15/30 min were collected for pure targets containing 2.8 g of ^{235}U or 2.9 g of ^{239}Pu and combined targets containing 2.8 g of ^{235}U and up to 4.8 g of ^{239}Pu as listed in tables II and III. After collecting the spectra, basic data processing was performed in order to create a set of standardized delayed

gamma-ray spectra to be used in further data analysis and deconvolution algorithm development. This processing consisted of the following steps:

- **Gain drift adjustment**. Inevitably, gain drifts occurred during the long collection times and from run to run. Hence, each spectrum was corrected for any gain drift by using a standard set of strong peaks.
- **Irradiation intensity normalization**. Each spectrum was normalized to the intensity of the neutron irradiation by dividing the number of detected photons by the total charge on the radiator, which is a proxy for the neutron fluence.
- **High-energy photon intensity normalization**. The spectra were also normalized by the number of photons detected between 3 and 6 MeV as a proxy for the number of induced fissions.
- **Rebinning of spectra**. Each spectrum was collected with 8192 channels and rebinned into 4096 channels. This resulted in smoothing and a decrease of statistical fluctuations.

Table II. Data file identifiers for the three complete data sets in which the targets were shuttled from the irradiation to the detection position. These irradiation/detection periods included 90/90 s, 5/5 min and 15/30 min.

Target Composition	90/90 s	5/5 min	15/30 min
2.8 g ^{235}U	20131118-110	20131118-100	20120618-012-017 20120909-066-070
2.8 g ^{235}U + 1.0 g ^{239}Pu	20131118-113	20131118-105	20120909-008-012
2.8 g ^{235}U + 2.9 g ^{239}Pu	20131118-112	20131118-104	20120618-022-028
2.8 g ^{235}U + 4.8 g ^{239}Pu	--	--	20120909-022-026
2.9 g ^{239}Pu	20131118-111	20131118-103	20120909-013-018

Table III. Data file identifiers for the two complete data sets in which the spectra were collected in situ with the irradiation.

Target Composition	10/10 s	60/60 s
2.8 g ^{235}U	20120618-038	20120909-047
2.8 g ^{235}U + 1.0 g ^{239}Pu	20120618-047	20120909-054
2.8 g ^{235}U + 2.9 g ^{239}Pu	20120618-045	20120909-059
2.8 g ^{235}U + 4.8 g ^{239}Pu	20120618-051-052	20120909-053
2.9 g ^{239}Pu	20120618-039-040	20120909-046

As a result of this processing the data are available with identical energy calibration and histogram binning as raw gamma-ray counts normalized to the neutron fluence or the integrated high-energy photon yield. Furthermore, the spectra are available with 4096 or 8192 channels. The data file identifiers for the complete sets are presented in Table II (shuttled samples) and Table III (in situ measurements). These spectra, raw binary data, laboratory notebooks and other ancillary data have all been uploaded to a data server and team members or other researchers may request an account/password in order to access the data that they need.

It is important to note that the data were taken in list-mode. Energy and time were recorded for every detected γ ray, i.e., the temporal information of the delayed gamma-ray emission is available and not just accumulated energy spectra. These list-mode data can be used to perform a time-dependent analysis, such as the fission yield analysis developed by Luke Campbell [4] and described in section II.3.1.

Discrete delayed gamma-rays from short-lived fission fragments can be identified based on the peaks in the spectra of Figures 4-6 and the fissile sensitivity of theses peaks can qualitatively been evaluated. These figures compare the high-energy spectra from the pure 2.8 g ^{235}U and 2.9 g ^{239}Pu targets for the 15/30 min, 5/5 min, and 90/90 s irradiation/detection cycles. For these measurements the targets were shuttled from the irradiation position to the spectroscopy station. A plethora of discrete gamma-rays lines are seen over the entire energy range with 16 of the 26 identified discrete delayed gamma-ray lines between ~2650 to ~3650 keV. The dominant fission fragments responsible for the gamma-ray lines were identified with the aid of a simplified model for calculating delayed gamma-ray spectra, which combined the cumulative fragment yield from ENDF/B-VII.1 with decay data from the ENSDF database [5].
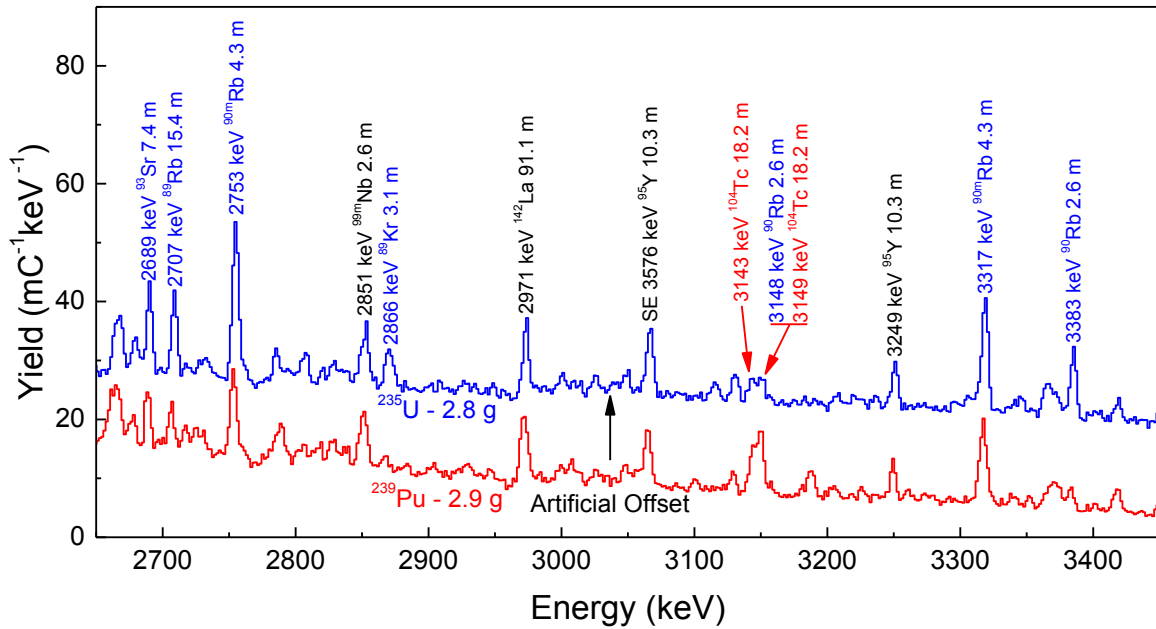

Figure 4a. Delayed gamma ray spectra from 2650 to 3450 keV for targets containing ~2.8 g of ^{235}U (blue) or ~2.9 g of ^{239}Pu target (red) irradiated by moderated neutrons. The irradiation/detection periods were 15/30 min and the total data collection time was ~3 hr. The ^{235}U spectrum is artificially shifted up to allow an easy comparison of the two spectra. The spectra are normalized to the total electron charge on the radiator as a proxy for the neutron fluence. The labels identify the likely fission fragment responsible for the discrete gamma ray and have been color coded to indicate which isotope has a larger cumulative fragment yield. A black label indicates that the cumulative fragment yields are nearly equal for ^{235}U and ^{239}Pu thermal neutron fission.
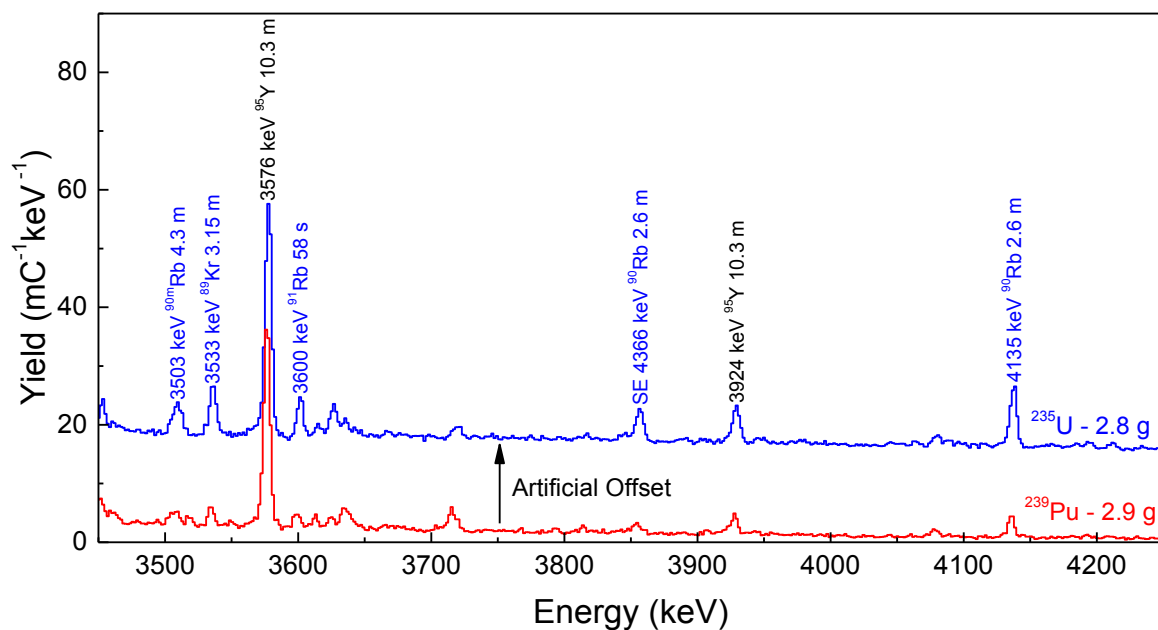
8

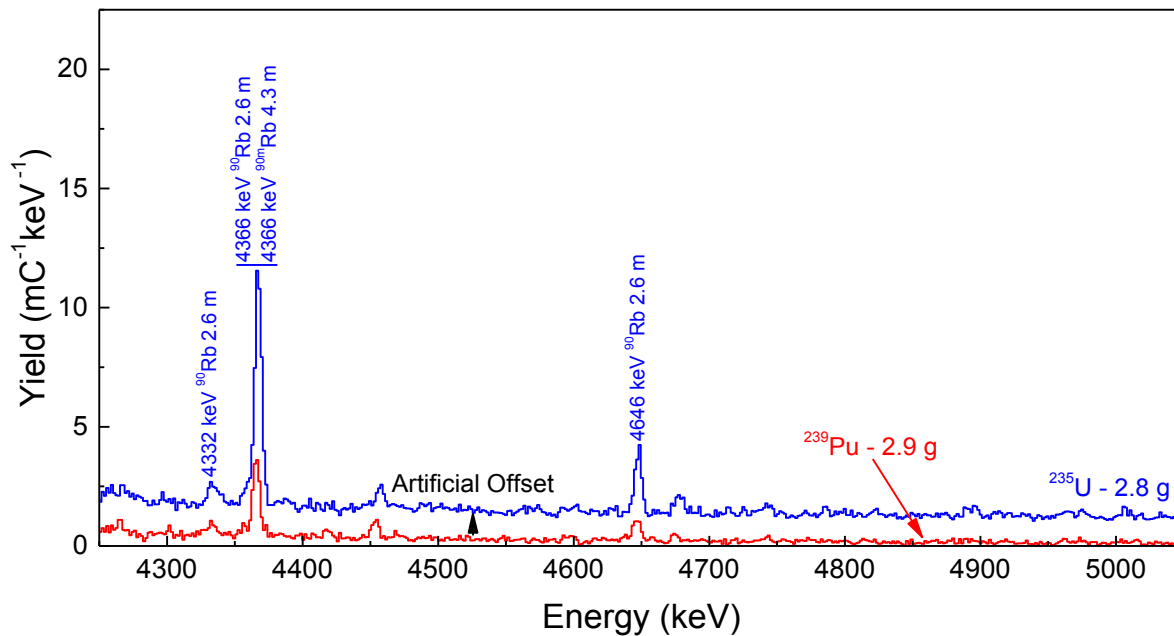Figure 4b. Delayed gamma-ray spectra as in figure 4a from 3450 to 4250 keV.

Figure 4c. Delayed gamma-ray spectra as in figure 4a from 4250 to 5050 keV.
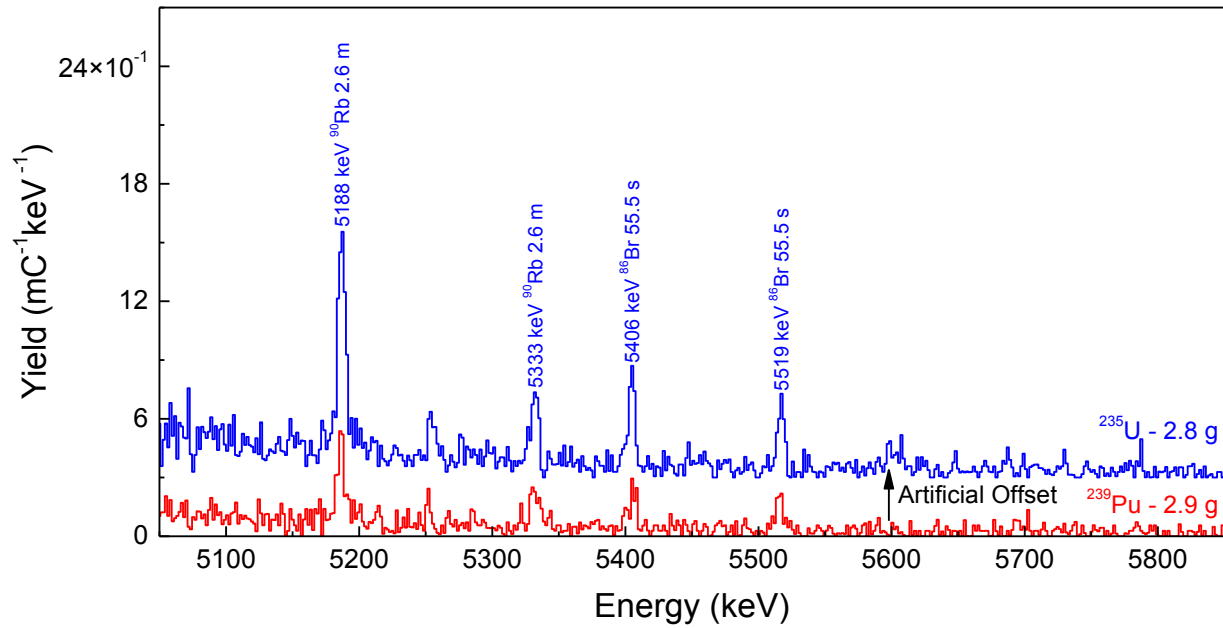
9

Figure 4d. Delayed gamma-ray spectra as in figure 4a from 5050 to 5850 keV.

Figure 5a. Delayed gamma-ray spectra from 2650 to 3450 keV for targets containing ~2.8 g of ^{235}U (blue) or ~2.9 g of ^{239}Pu target (red) irradiated by moderated neutrons. The irradiation/detection periods were 5/5 min and the total data collection time was ~2.25 hr. The ^{235}U spectrum is artificially shifted up to allow an easy comparison of the two spectra. The spectra are normalized to the total electron charge on the radiator as a proxy for the neutron fluence. The labels identify the likely fission fragment responsible for the discrete gamma ray and have been color coded to indicate which isotope has a larger cumulative fragment yield. A black label indicates that the cumulative fragment yields are nearly equal for ^{235}U and ^{239}Pu thermal neutron fission.

Figure 5b. Delayed gamma-ray spectra as in figure 5a from 3450 to 4250 keV.

Figure 5c. Delayed gamma-ray spectra as in figure 5a from 4250 to 5050 keV.

Figure 5d. Delayed gamma-ray spectra as in figure 5a from 5050 to 5850 keV.
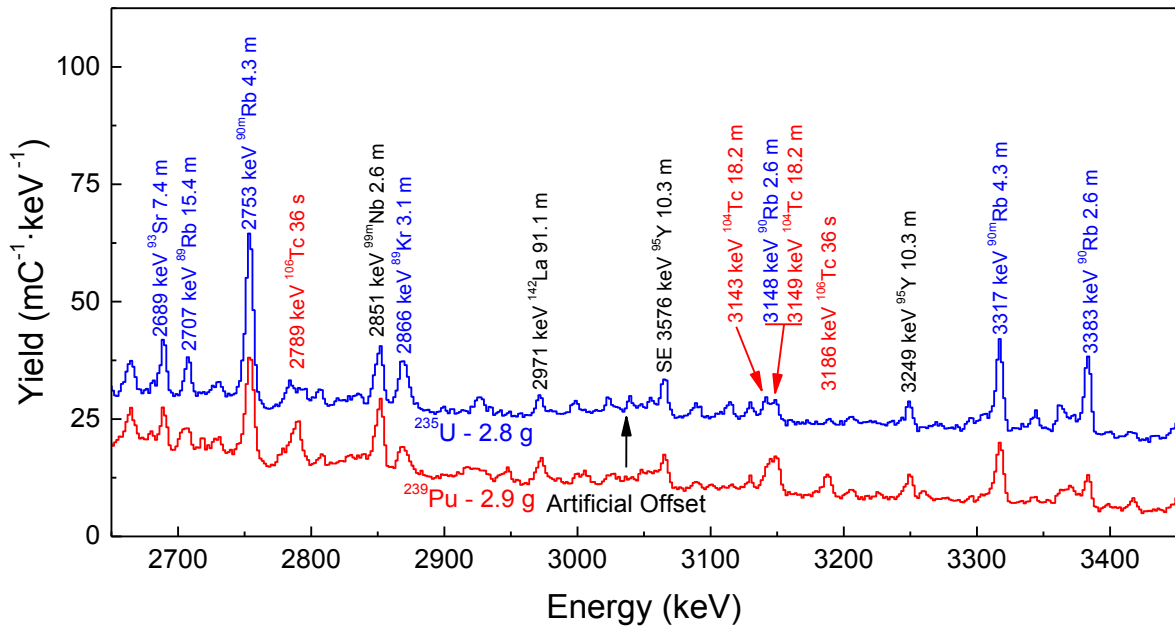

Figure 6a. Delayed gamma-ray spectra from 2650 to 3450 keV for targets containing ~2.8 g of ^{235}U (blue) or ~2.9 g of ^{239}Pu target (red) irradiated by moderated neutrons. The irradiation/detection periods were 90/90 s and the total data collection time was ~1.62 hr. The ^{235}U spectrum is artificially shifted up to allow an easy comparison of the two spectra. The spectra are normalized to the total electron charge on the radiator as a proxy for the neutron fluence. The labels identify the likely fission fragment responsible for the discrete gamma ray and have been color coded to indicate which isotope has a larger cumulative fragment yield. A black label indicates that the cumulative fragment yields are nearly equal for ^{235}U and ^{239}Pu thermal neutron fission.
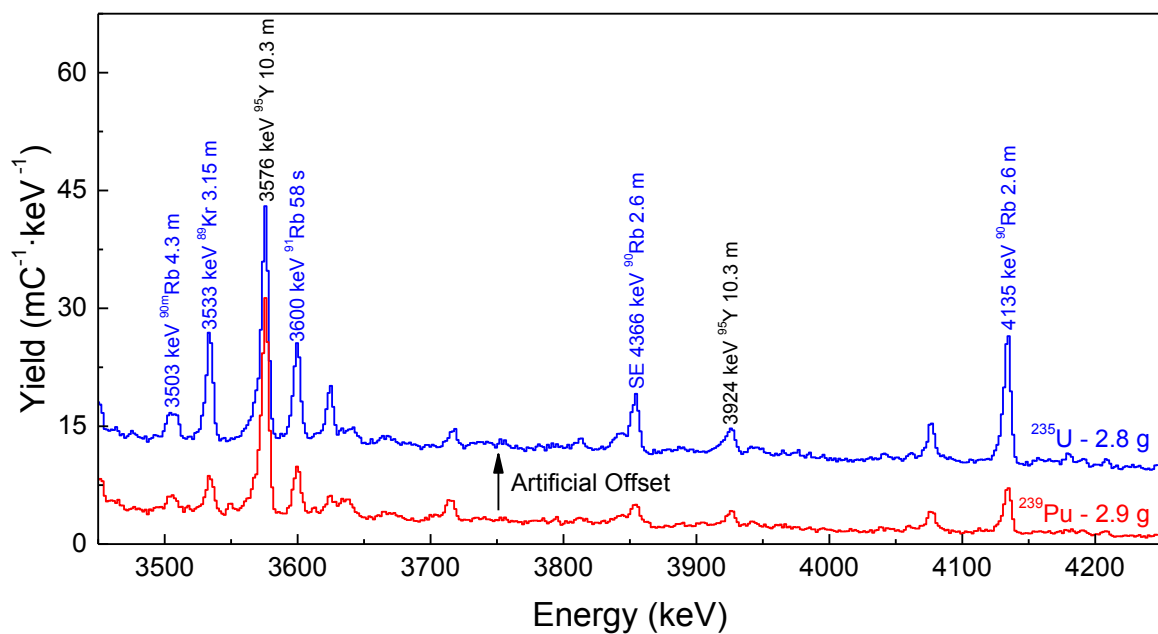
Figure 6b. Delayed gamma-ray spectra as in figure 6a from 3450 to 4250 keV.
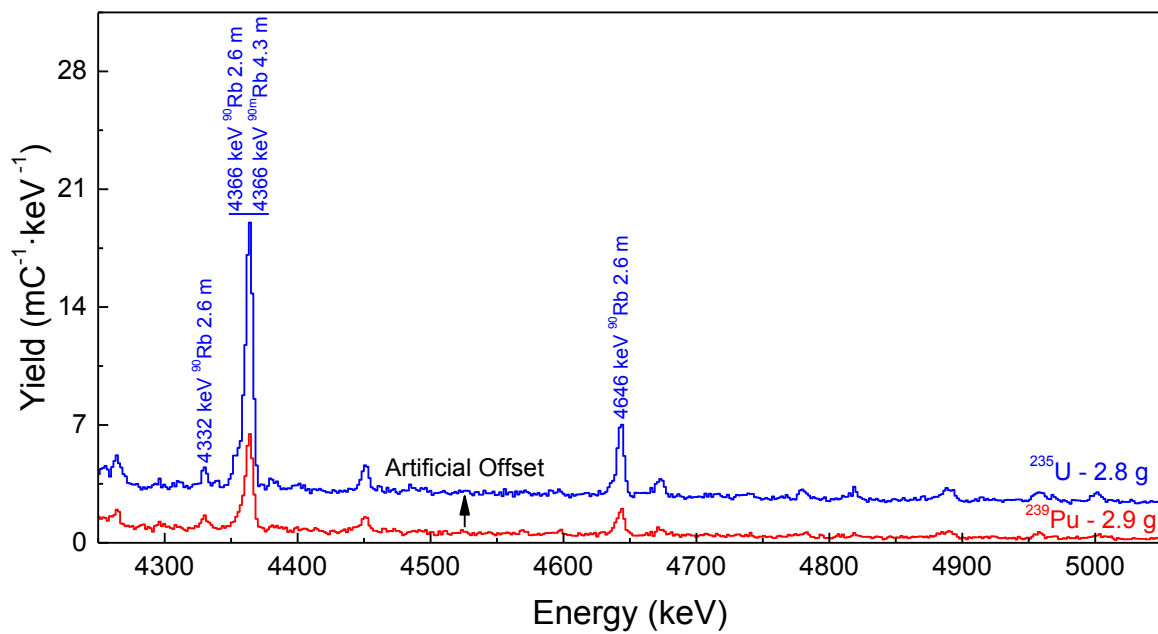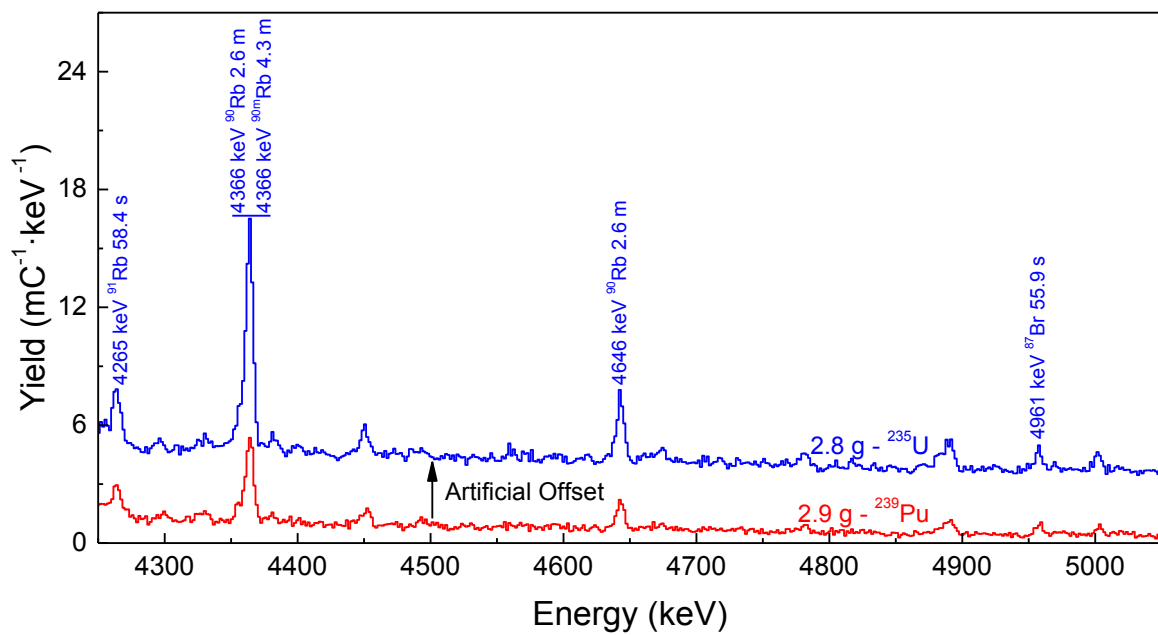

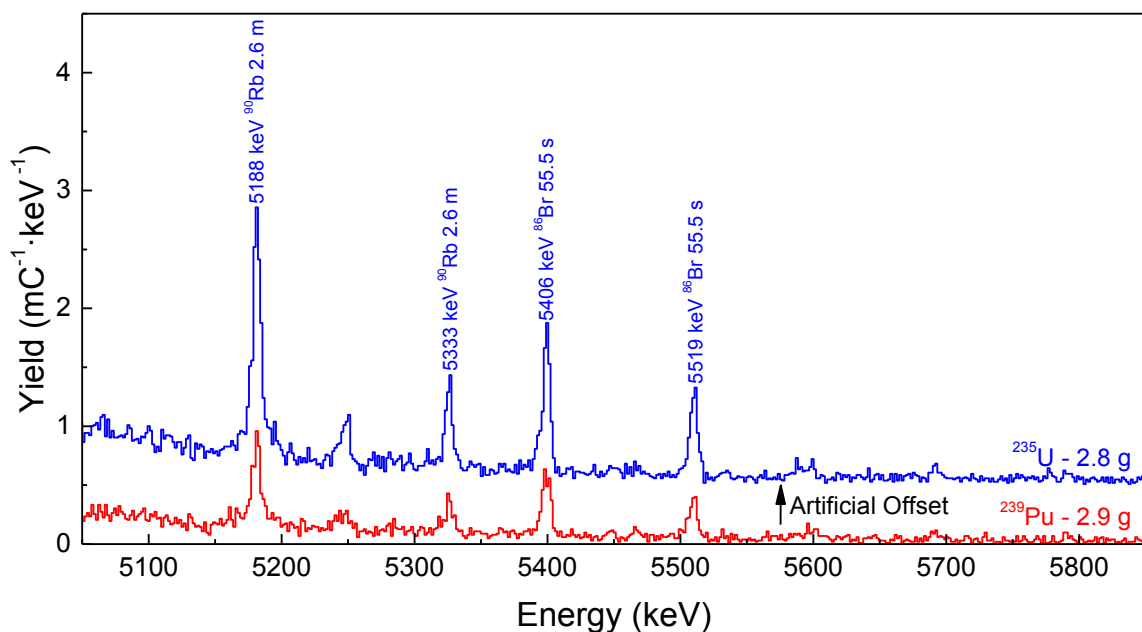Figure 6c. Delayed gamma-ray spectra as in figure 6a from 4250 to 5050 keV.

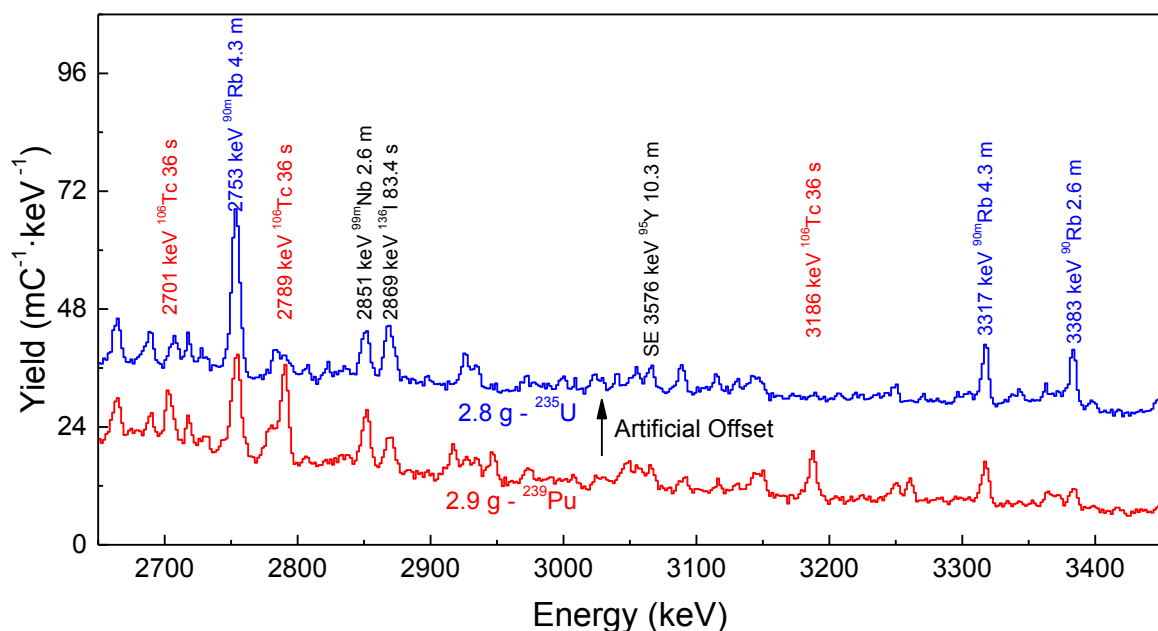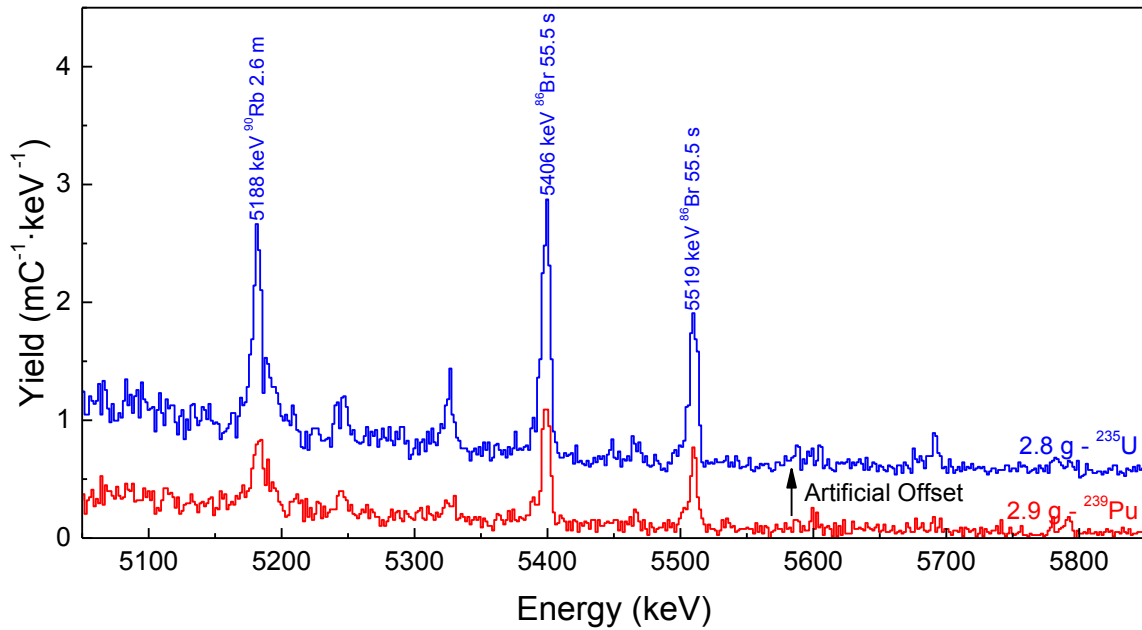Figure 6d. Delayed gamma-ray spectra as in figure 6a from 5050 to 5850 keV.
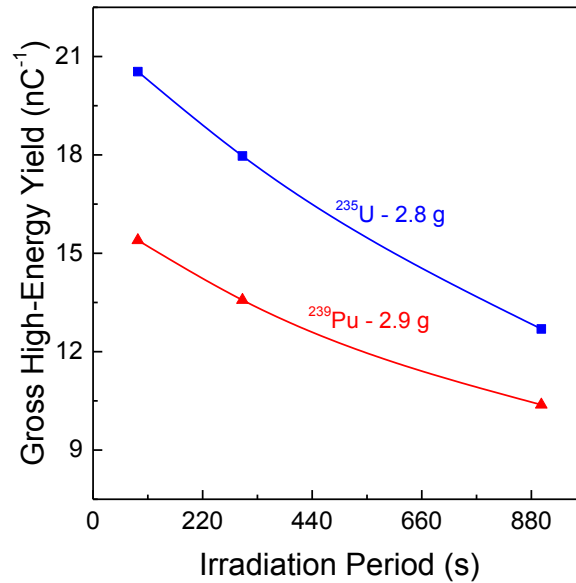
Figure 7. Gross high-energy gamma-ray yield integrated from 3 MeV to 6 MeV as a function of the irradiation time from the 2.8 g [235]U and 2.9 g [239]Pu targets. The irradiation detection periods (data points) were 90/90 s, 5/5 min and 15/30 min.

Most useful for safeguards applications are high-energy gamma-rays from short-lived fission fragment in a low background region. Their intensity is dependent on the fissile mass in the sample. Figure 7 shows the gross gamma-ray yield between 3 and 6 MeV from the pure 2.8 g [235]U and 2.9 g [239]Pu targets for the 90/90 s, 5/5 min and 15/30 min irradiation/detection periods. This gross high-energy yield is normalized to per unit electron charge on the bremsstrahlung radiator as a proxy for the neutron fluence on the sample. Hence the number of high-energy gamma-rays detected with the 90/90 s irradiation/detection period is ~50% greater than the 15/30 min

irradiation detection period. The ratio of the ^{235}U yield to the ^{239}Pu yield was on average 1.3 (i.e. the yield from ^{235}U is 1.3 times larger than the yield from ^{239}Pu). This agrees well with expectations when taking the differences in fission cross sections and fissile masses into account.

The larger gross high-energy gamma-ray yields for the shorter irradiation/detection periods suggest better statistics in determining the fissile content for a given neutron fluence but do not necessarily indicate an enhanced capability to quantify the relative ^{235}U and ^{239}Pu fractions in a sample. Discrete delayed gamma-rays that provide a strong indicator of ^{235}U and/or ^{239}Pu fission make it easier to quantify the fissile fractions. In Figures 4 through 6, the identified discrete delayed gamma-ray lines have been color coded to indicate when the cumulative fragment yield is over ~1.5 time larger from ^{235}U (blue label) or ^{239}Pu (red label), according to the ENDF/B-VII.1 database [6]. Starting with the 15/30 min irradiation/detection periods in the most populous spectral region from 2650 to 3450 keV in Figure 4, there are a number of similarities and differences that may be exploitable for determining the quantity of ^{235}U and/or ^{239}Pu. There are up to 6 discrete gamma-ray lines from precursor fragments ^{89}Rb, ^{89}Kr, ^{90}Rb, ^{90m}Rb and ^{93}Sr that are significantly stronger in the fission of ^{235}U. Furthermore ^{90}Rb emits gamma-rays with energies up to 5333 keV, with very intense high-energy lines at 4135 and 4366 keV. For these higher-energy lines of ^{90}Rb the intensity from the pure ^{235}U target is ~3 time larger than from the ^{239}Pu target, which is in agreement with the ENDF/B-VII.1 database value of 3±0.5 [6].

At higher-energy regions of the spectra, the density of discrete lines decreases drastically with many of them arising from ^{90}Rb fission fragments. First, figures 4b and 4c spanning from 3450 to 5050 keV contain additional discrete gamma-ray lines from ^{89}Kr, ^{90}Rb and ^{90m}Rb. Furthermore, a strong discrete gamma-ray line from ^{95}Y with 10.3 min half-life is observed at 3576 keV with a smaller line at 3924 keV. The ^{95}Y fission fragment is one of the most abundant fragments with a cumulative yield of ~6.4% for ^{235}U fissions and 4.7% for ^{239}Pu. The observed ^{235}U/^{239}Pu ratio is in agreement with the ENDF/B-VII.1 database value of 1.3±0.3. Finally in this region, a small discrete gamma-ray line at 3600 keV from ^{91}Rb is observed, which has a half-life of only 58 s, and is ~3.4 times stronger for ^{235}U fission compared to ^{239}Pu. The highest energy region from 5050 to 5850 keV in Figure 4d has two additional lines from ^{90}Rb at 5188 and 5333 keV and two lines at 5406 and 5519 keV from ^{86}Br, which has a short half-life of 55.5 s. While these highest-energy discrete delayed gamma-ray lines have low yields, they are in a very clean region of the spectra with little background or interferences.

While the discrete delayed gamma-ray lines from ^{90}Rb and ^{90m}Rb provided strong indicators of ^{235}U fission, there were no strong indicators for ^{239}Pu fission when using the 15/30 min irradiation/detection periods. There are two ^{104}Tc discrete gamma-rays at 3143 and 3149 keV with the parent having a half-life of 18.3 min that are stronger from ^{239}Pu fission. The cumulative yield data from ENDF/B-VII.1 supports this with a cumulative yield of 6.1% for ^{239}Pu fission and 1.9% for ^{235}U fission; 3.2 times larger from ^{239}Pu. While the yield of ^{104}Tc is large for ^{239}Pu fission, the branching ratio to the high-energy gamma-ray lines is low at 0.8% and 1.16%, respectively. Furthermore, there is a minor ^{90}Rb line also at 3149 keV creating an interference with the peaks from ^{104}Tc. There are stronger ^{104}Tc discrete gamma-ray lines at energies below 2600 keV but these lines are in the higher background region riddled with interferences.

For shorter irradiation/spectroscopy periods two small lines of ^{106}Tc with a half-life of 36 s become prominent in ^{239}Pu at 2789 and 3186 keV that are nearly absent in the ^{235}U spectrum, as seen in Figures 5a and 6a. This is in agreement with the ENDF/B-VII.1 database that gives the ^{106}Tc yield as ~10 times larger for ^{239}Pu than ^{235}U. The ^{235}U fission spectrum exhibits a feature at 2789 keV but that arises primarily from minor lines at 2783 and 2790 keV from ^{91}Rb with a half-life

of 58 s. Furthermore, [106]Tc also emits a minor gamma-ray at 2777 keV with a branching ratio approximately 3 times smaller than the 2789 keV, resulting in the low-energy shoulder observed in the [239]Pu spectrum.

The relative strength of other lines in the spectra also change with decreasing irradiation/spectroscopy cycle times. To more easily see these changes, Figures 8 and 9 compare the energy spectra using 15/30 min, 5/5 min and 90/90 sec irradiation/spectroscopy periods from the 2.8 g [235]U target (Figures 8a-d) and the 2.9 g [239]Pu target (Figures 9a-d). Short half-lives (e.g. [91]Rb, [106]Tc, etc…) decays generate the strongest signals in short cycle time measurements whereas fission fragments with long half-lives (e.g. [95]Y, [142]La etc…) are dominant for longer irradiation/spectroscopy periods. To more quantitatively observe these changes, Figure 10a shows the integrated intensity of three lines measured for the 2.8 g [235]U sample (i.e. Figure 8b), the 3600 keV line from [91]Rb with a 58 s half-life, the 3576 keV line from [95]Y with a 10.3 min half-life and the 4135 keV line from [90]Rb with a 2.6 min half-life as a function of the irradiation period. The yield of the 3600 keV gamma-ray from [91]Rb (58 s half-life) increases by a factor of ~2.8 going from the 15/30 min to the 90/90 sec cycle. In contrast to the short half-life [91]Rb fragment, the yield of the 3576 keV gamma-ray from [95]Y (10.3 min half-life) decreases by a factor of ~3.2 from the 15/30 min to the 90/90 sec cycle. The yield of the 4135 keV gamma-ray from [90]Rb (2.6 min half-life) was highest at the 5/5 min irradiation/spectroscopy period, ~33% and ~69% above those of the 90/90 s and 15/30 min cycles, respectively.

Figure 8a.   Delayed gamma-ray spectra from 2650 to 3450 keV for the ~2.8 g [235]U target irradiated by moderated neutrons. This figure compares the 15/30 min (blue), 5/5 min (red) and 90/90 sec (black) irradiation/detection periods with the latter two spectra artificially shifted up for clarity. The spectra are normalized to the total electron charge on the radiator as a proxy for the neutron fluence. The labels identify the likely fission fragment responsible for the discrete gamma ray and have been color coded to indicate which isotope has a larger cumulative fragment yield with a blue label for [235]U and red for [239]Pu. A black label indicates that the cumulative fragment yields are nearly equal for [235]U and [239]Pu thermal neutron fission.

Figure 8b. Delayed gamma-ray spectra as in figure 8a from 3450 to 4250 keV.

Figure 8c. Delayed gamma-ray spectra as in figure 8a from 4250 to 5050 keV.

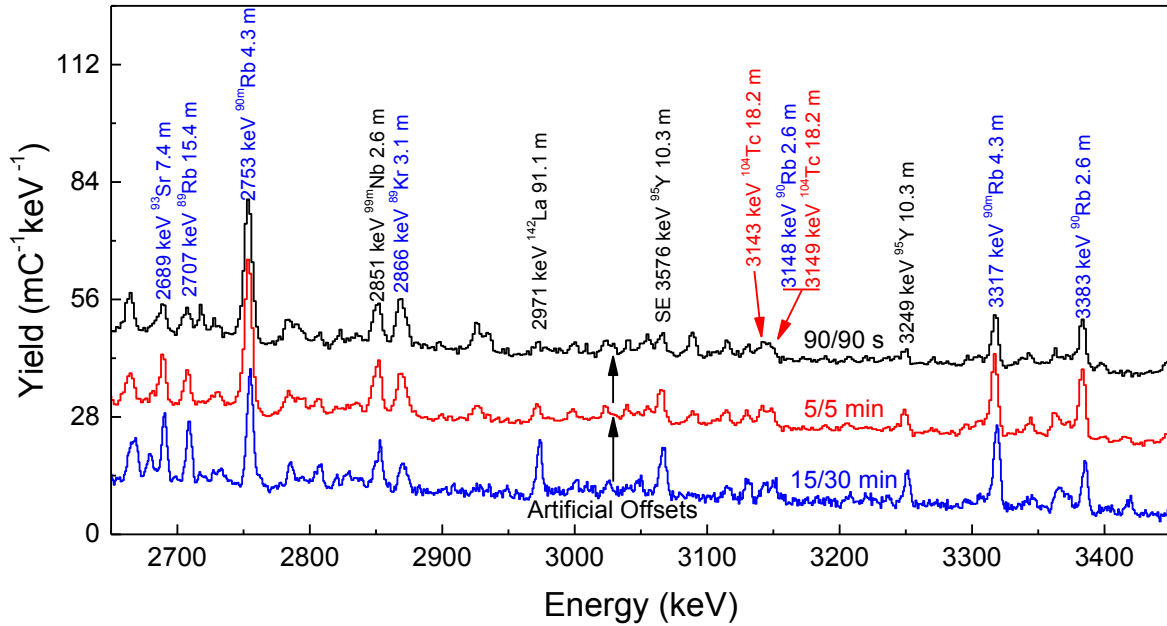Figure 8d. Delayed gamma-ray spectra as in figure 8a from 5050 to 5850 keV.

Figure 9a. Delayed gamma-ray spectra from 2650 to 3450 keV for the ~2.9 g ^{239}Pu target irradiated by moderated neutrons. This figure compares the 15/30 min (blue), 5/5 min (red) and 90/90 sec (black) irradiation/detection periods with the latter two spectra artificially shifted up for clarity. The spectra are normalized to the total electron charge on the radiator as a proxy for the neutron fluence. The labels identify the likely fission fragment responsible for the gamma-ray line and have been color coded to indicate which isotope has a larger cumulative fragment yield with a blue label for ^{235}U and red for ^{239}Pu. A black label indicates that the cumulative fragment yields are nearly equal for ^{235}U and ^{239}Pu thermal neutron fission.
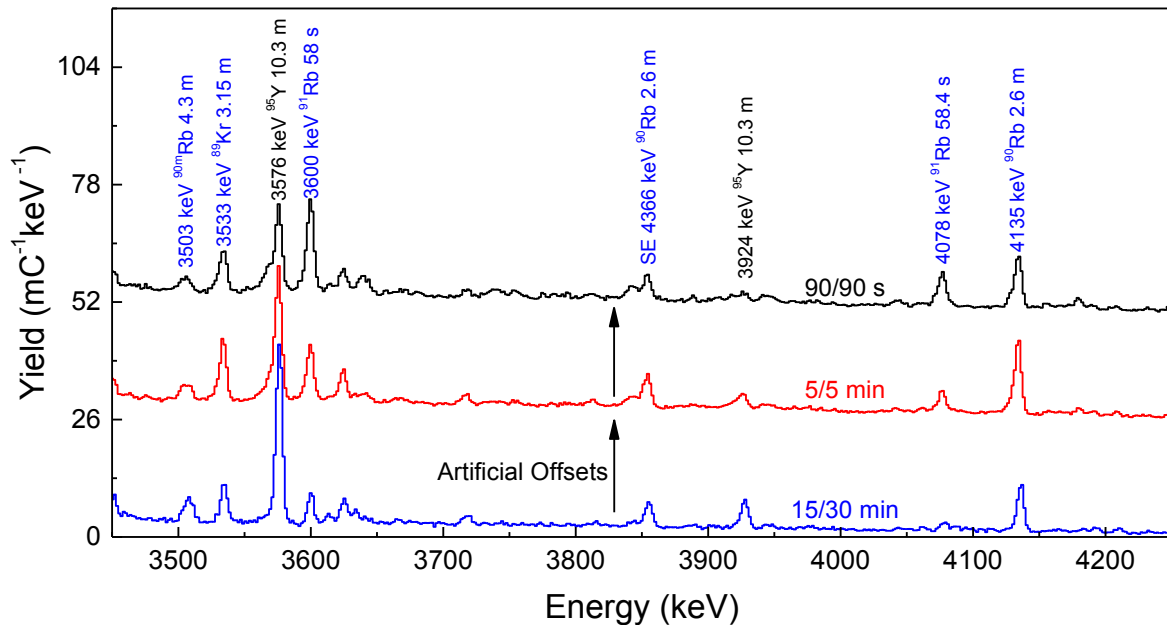
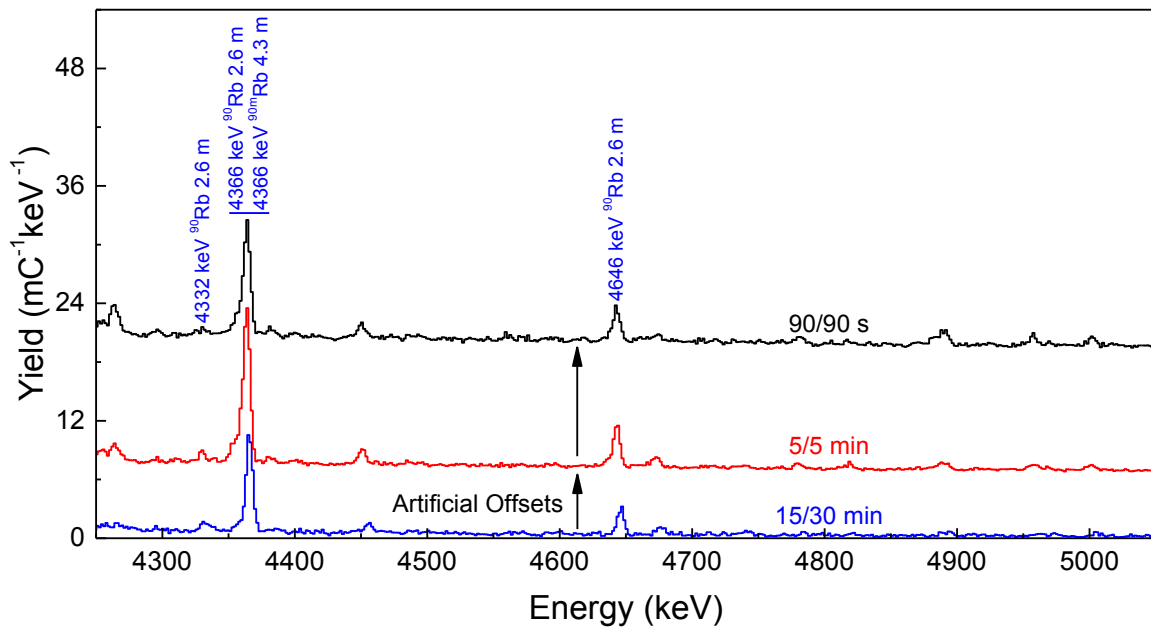Figure 9b. Delayed gamma-ray spectra as in figure 9a from 3450 to 4250 keV.

Figure 9c. Delayed gamma-ray spectra as in figure 9a from 4250 to 5050 keV.
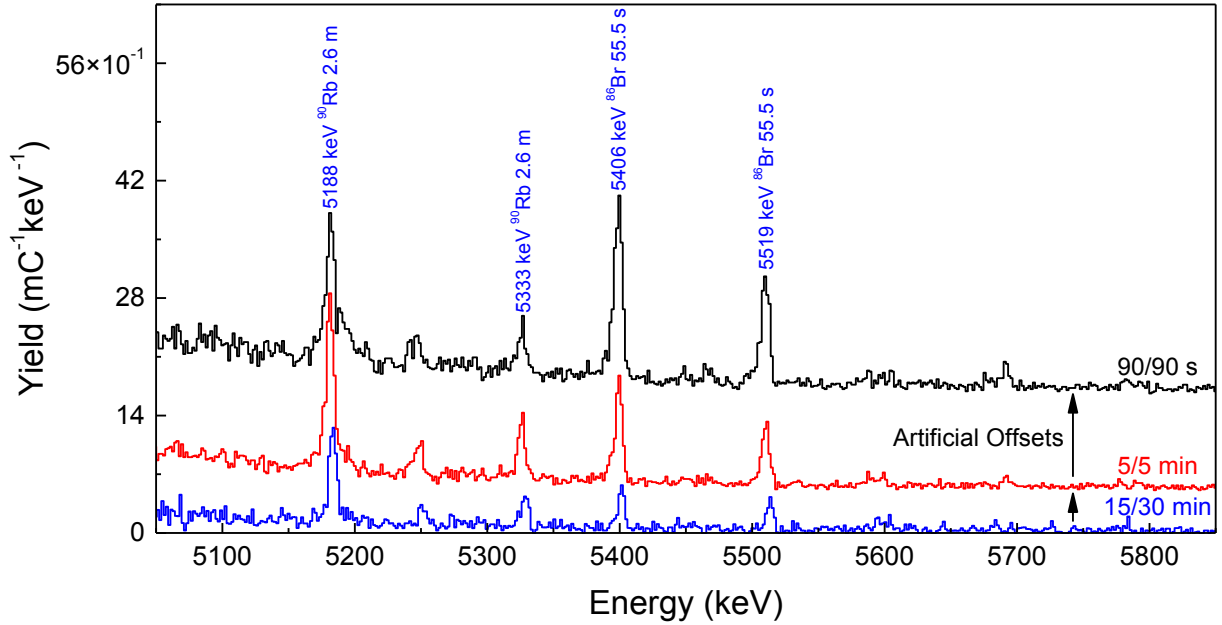
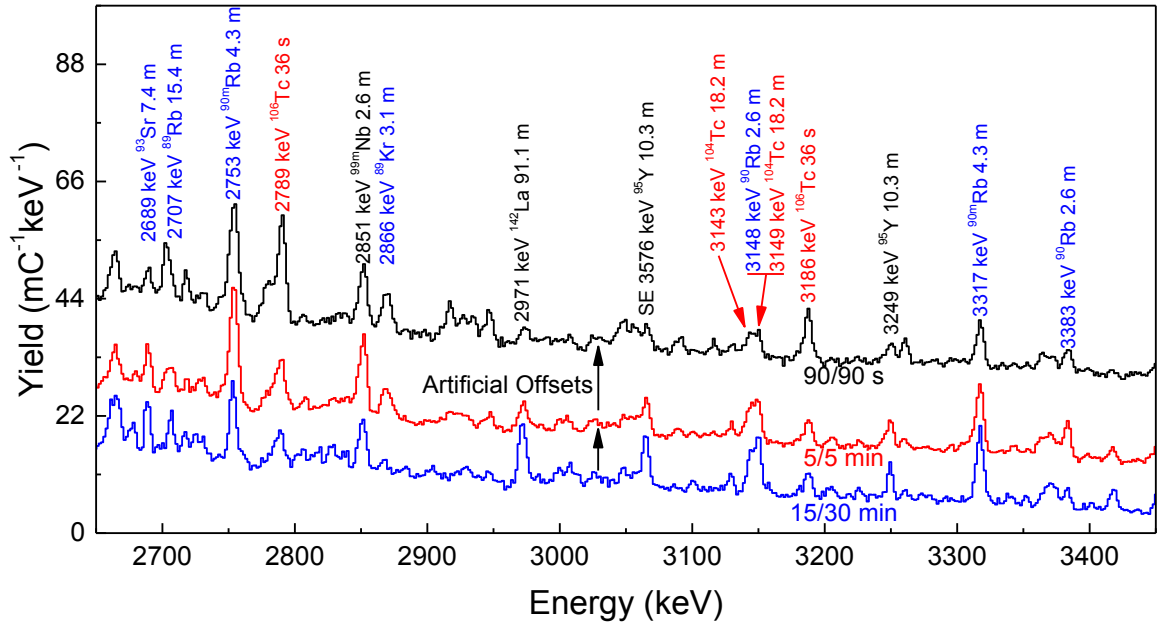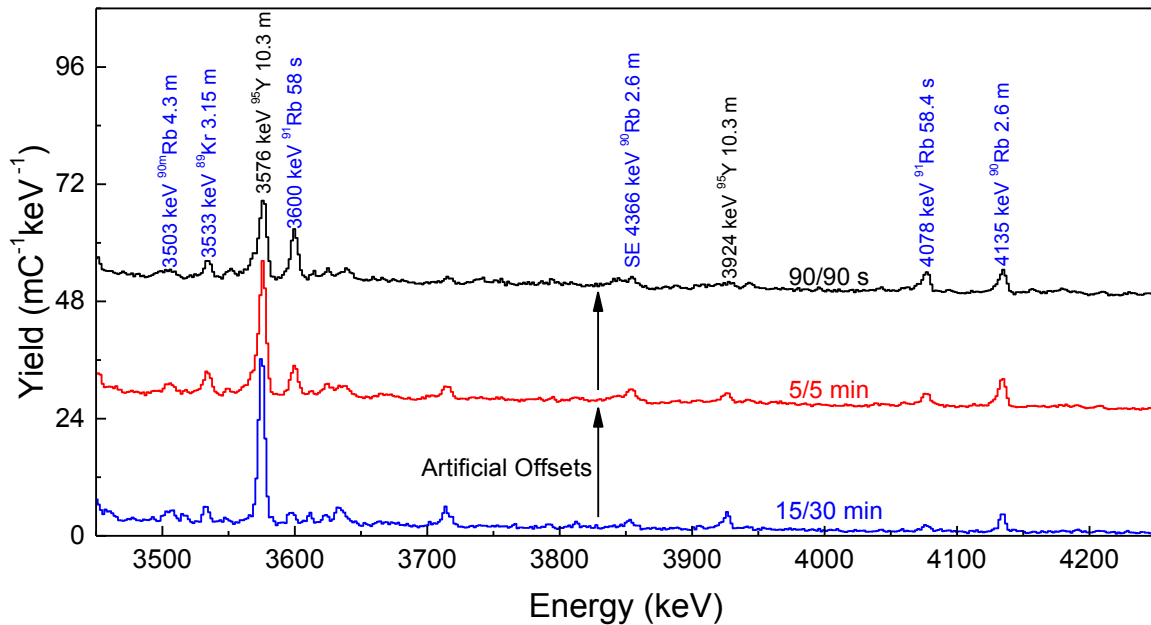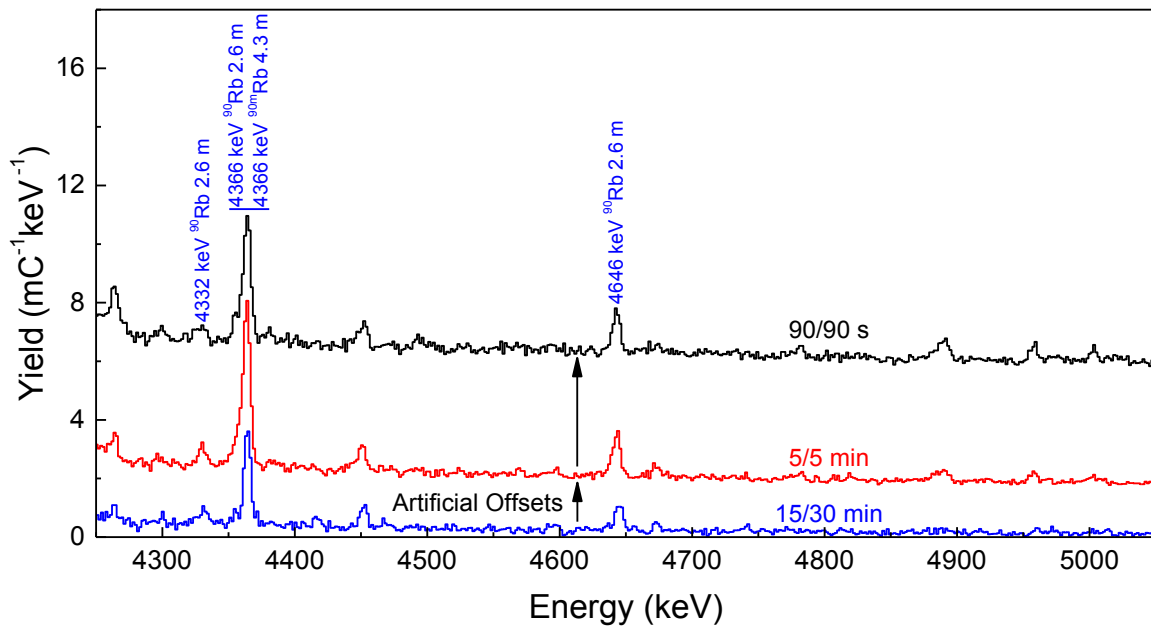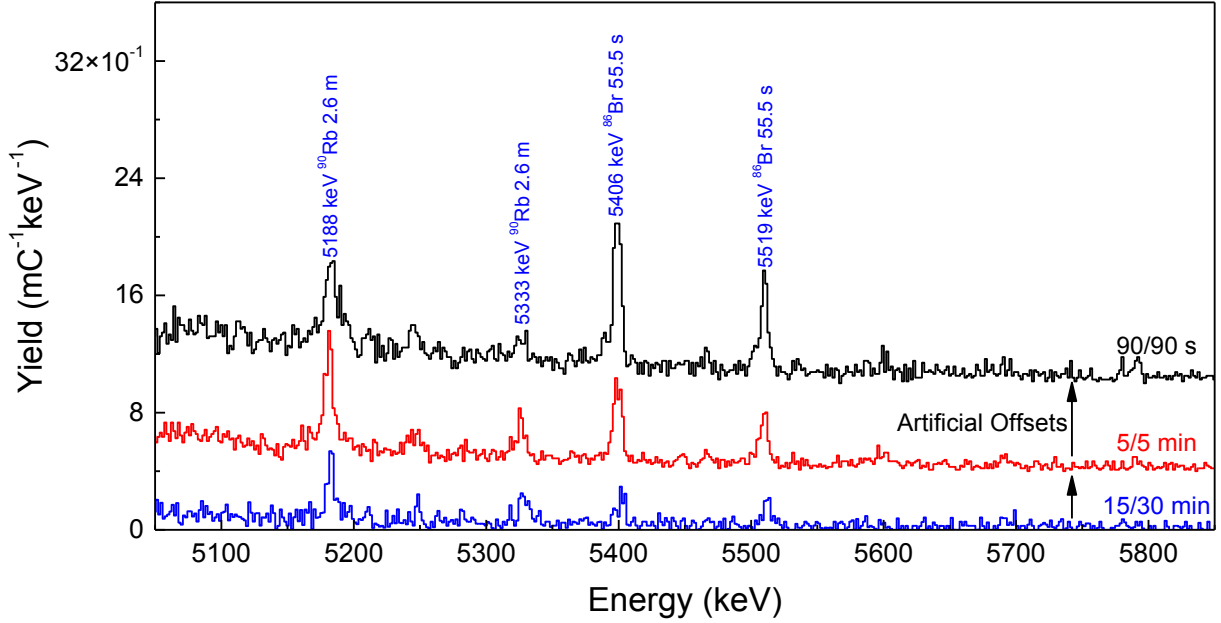Figure 9d. Delayed gamma-ray spectra as in figure 9a from 5050 to 5850 keV.

The change of the discrete gamma-ray yields with the irradiation/spectroscopy periods is governed by standard production and exponential decay of the radioisotopes. For fission fragments, the production and decay is complicated by the fragment of interest being fed by fragments farther from the valley of stability but the basic behaviors can be understood in a simple model in which this feeding is neglected. A simple schematic of the irradiation/detection periods is shown in Figure 10b. The first irradiation period ($k = 0$) begins at $t = 0$ and lasts for the irradiation period, t_p. After irradiation, there is a small gap before the detection period begins at $t = t_o$ accounting for the transit time with the detection period ending at t=t_f. After the detection period, there is another gap accounting for the transit time before the next irradiation period ($k = 1$) begins at $t = \Delta t$. This basic inspection cycle is then repeated with the second detection period beginning at $t = t_o + \Delta t$ and ending at $t = t_f + \Delta t$ followed by the third irradiation period ($k = 2$) beginning at $t = 2\Delta t$. In this way, the detection period after any of the irradiation pulses begins at $t = t_o + k\Delta t$ and ends at $t = t_f + k\Delta t$. Starting with the first irradiation period, $k = 0$, the number of radioisotopes of interest produced at the end of the irradiation period is given by

$$N_{0p} = \frac{P}{\lambda}\left(1 - e^{-\lambda t_p}\right) \tag{1}$$

where P is the production rate during the irradiation, λ is the decay rate of the fragment of interest. The number of gamma-rays detected is then given by

$$C_{0d} = \varepsilon\beta\frac{P}{\lambda}\left(1 - e^{-\lambda t_p}\right)\left[e^{-\lambda(t_o-t_p)} - e^{-\lambda(t_f-t_p)}\right] \tag{2}$$

where β is the branching ratio of the discrete gamma-ray and ε is the absolute photopeak detector efficiency. After the second irradiation period ($k = 1$), the number of gamma-rays detected between $t = t_o + \Delta t$ and $t = t_f + \Delta t$ is

$$C_{1d} = C_\infty\left[e^{-\lambda(t_o-t_p)} - e^{-\lambda(t_f-t_p)}\right] + C_\infty\left[e^{-\lambda(t_o+\Delta t-t_p)} - e^{-\lambda(t_f+\Delta t-t_p)}\right] \tag{3}$$

with

$$C_\infty = \varepsilon\beta\frac{P}{\lambda}\left(1 - e^{-\lambda t_p}\right) \tag{4}$$

20

The first term in Equation (3) represents gamma-rays from fission fragments produced in the $k = 1$ irradiation period and the second term represents gamma-rays from fission fragments produced in the $k = 0$ irradiation period. For an arbitrary number of irradiation periods, the number of gamma-rays detected between $t = t_o + k\Delta t$ and $t = t_f + k\Delta t$ is

$$C_{nd} = C_\infty \sum_{k=0}^{n} \left[e^{-\lambda(t_o + k\Delta t - t_p)} - e^{-\lambda(t_f + k\Delta t - t_p)} \right] \qquad (5)$$

which can be simplified to

$$C_{nd} = C_\infty \left[e^{-\lambda(t_o - t_p)} - e^{-\lambda(t_f - t_p)} \right] \sum_{k=0}^{n} \left(e^{-\lambda\Delta t} \right)^k \qquad (6)$$

The summation is nothing more than a geometric series with the solution resulting in

$$C_{nd} = C_\infty \left[e^{-\lambda(t_o - t_p)} - e^{-\lambda(t_f - t_p)} \right] \frac{1 - e^{-\lambda(n+1)\Delta t}}{1 - e^{-\lambda\Delta t}} \qquad (7)$$

for the number of gamma-rays detected after the $k = n$ irradiation period.

The experimental spectra were a summation of all detection periods and hence the total detected gamma-rays is found by summing Equation (7) over all irradiation/detection periods

$$C_{Td} = \sum_{n=0}^{n_T - 1} C_{nd} = C_\infty \left[e^{-\lambda(t_o - t_p)} - e^{-\lambda(t_f - t_p)} \right] \sum_{n=0}^{n_T - 1} \frac{1 - e^{-\lambda(n+1)\Delta t}}{1 - e^{-\lambda\Delta t}} \qquad (8)$$

Rearranging the term within the summation the total number of counts is given by

$$C_{Td} = C_\infty \frac{e^{-\lambda(t_o - t_p)} - e^{-\lambda(t_f - t_p)}}{1 - e^{-\lambda\Delta t}} \sum_{n=0}^{n_T - 1} \left[1 - e^{-\lambda\Delta t} \left(e^{-\lambda\Delta t} \right)^n \right] \qquad (9)$$

where n_T is the total number of irradiation/detection periods. The second term in the summation is another geometric series resulting in

$$C_{Td} = C_\infty \frac{e^{-\lambda(t_o - t_p)} - e^{-\lambda(t_f - t_p)}}{1 - e^{-\lambda\Delta t}} \left[n_p - e^{-\lambda\Delta t} \frac{1 - e^{-\lambda n_T \Delta t}}{1 - e^{-\lambda\Delta t}} \right] \qquad (10)$$

The detected gamma-rays can be normalized to the total electron charge on the radiator as a proxy for the neutron fluence as was done with the experimental spectra. Figure 11 shows the calculated yields for radioisotopes with a 58 s, 10.3 min and 2.6 min half-life as a function of the irradiation period. The qualitative behavior matches what was observed in Figure 10a for ^{91}Rb, ^{95}Y and ^{90}Rb, respectively. For a more quantitative comparison, the production and decay of ^{91}Kr ($t_{1/2} = 8.6$ s), ^{95}Sr ($t_{1/2} = 25.1$ s) and ^{90}Kr ($t_{1/2} = 32.3$ s) must be considered because they directly feed into ^{91}Rb, ^{95}Y and ^{90}Rb.
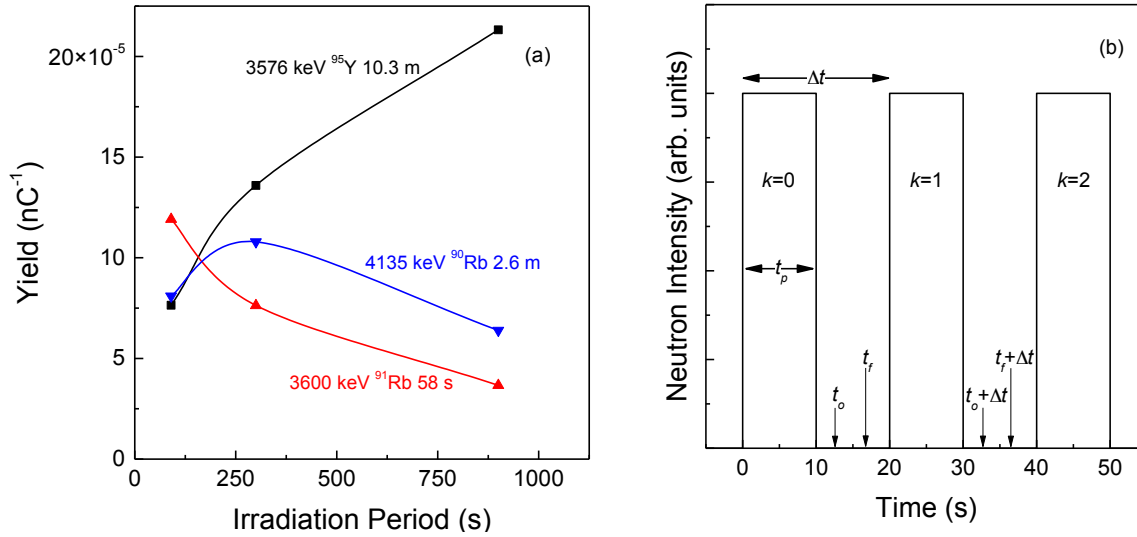
Figure 10. Integrated yield of discrete delayed gamma-ray lines from ^{91}Rb (▲), ^{95}Y (■) and ^{90}Rb (▼) as a function of the irradiation period (a) and a schematic of the irradiation/detection periods (b). The integrated yields were all measured from the 2.8 g ^{235}U sample (Figure 8b)
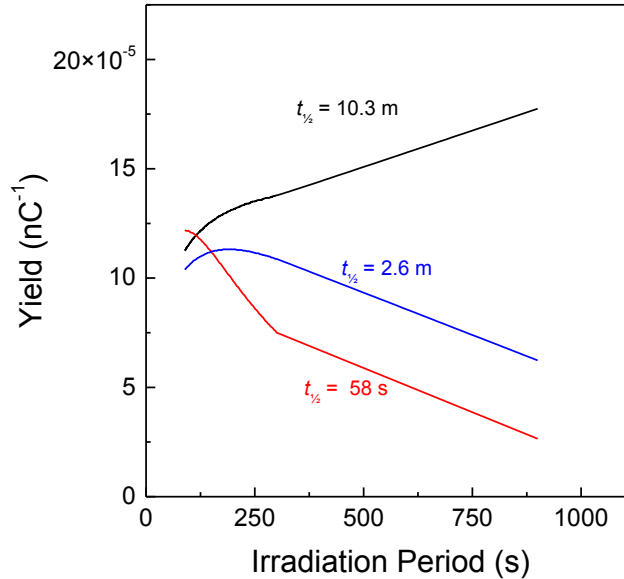
Figure 11. Calculated yields of discrete delayed gamma-ray lines from radioisotopes having half-lives of 58 s (red line), 10.3 min (black line) and 2.6 min (blue line) as a function of the irradiation period. These yields were calculated using Equation (10).

Sets of delayed gamma-ray spectra were also collected for 10/10 s and 60/60 s irradiation/spectroscopy periods for which the fissile sample and the HPGe detector were kept at the irradiation station as seen in Figure 1. Figure 12a compares the spectrum of a pure 2.9 g ^{239}Pu sample (2650 to 3450 keV) measured with sample and detector at the irradiation station (60/60 s irradiation/detection periods) to the spectrum taken when the sample was shuttled to the remote spectroscopy station (90/90 s irradiation/detection periods). The strong gamma-ray lines at 2800 and 3045 keV in the in situ spectrum were not observed when the sample was shuttled and measured at the spectroscopy station. These lines were due to true coincidences of 1293+1507 keV

gamma-rays or 1293+1752 keV gamma-rays from [116m]In, which has a half-life of 54.3 min. This radioisotope was produced by neutron activation of indium, [115]In(n,γ)[116m]In, that is used as a thermal coupler in the HPGe detector and thus is very close to the Ge crystal. Unfortunately, the coincidence line at 2800 keV is large enough and close enough to the 2789 keV line from [106]Tc to obscure this strong indicator of [239]Pu fission. To confirm these interferences, a spectrum without a fissile sample was collected with a 60/60 s irradiation period (overlaid in Figure 12). The coincidence lines from [116m]In are clearly visible in this background spectrum along with 1293, 1507 and 1752 keV gamma-rays at lower-energy regions of the spectrum. In addition, a line at 2754 keV was observed in this background spectrum from [24]Na, which has a half-life of 15 hr. This radioisotope was produced by the thermal neutron activation reaction [23]Na(n,γ)[24]Na with a cross section of ~530 mb. This [24]Na background line directly interferes with the 2753 keV [90m]Rb discrete gamma-ray. In addition, the baseline under the discrete gamma-ray lines in the situ spectra was a factor of ~2 larger than in those measured at the spectroscopy station. Figure 12b compares the spectra between 3450 and 4250 keV of a pure 2.8 g [235]U sample to the spectrum measured at the remote spectroscopy station. In order to avoid the activation issues of the in situ measurements, a mechanical sample shuttle was installed and used to transport the sample to the remote spectroscopy station.

Figure 12a. Delayed gamma-ray spectra from 2650 to 3450 keV for the ~2.9 g [239]Pu target irradiated by moderated neutrons. This figure compares the 90/90 sec (black) and 60/60 s (red) irradiation/detection periods. Overlaid on this graph is a spectrum without a fissile sample using a 60/60 s irradiation/detection periods (blue). In the 90/90 sec irradiation/detection periods the fissile sample was shuttle from the irradiation position to the detection position. In the 60/60 sec irradiation/detection periods the fissile sample was stationary and the detector was in situ with the irradiation setup. The spectra are normalized to the total electron charge on the radiator as a proxy for the neutron fluence. The labels identify the likely fission fragment responsible for the discrete gamma-ray and have been color coded to indicate which isotope has a larger cumulative fragment yield with a blue label for [235]U and red for [239]Pu. A black label indicates that the cumulative fragment yields are nearly equal for [235]U and [239]Pu thermal neutron fission. A magenta label indicates an activation product that is not a fission fragment.
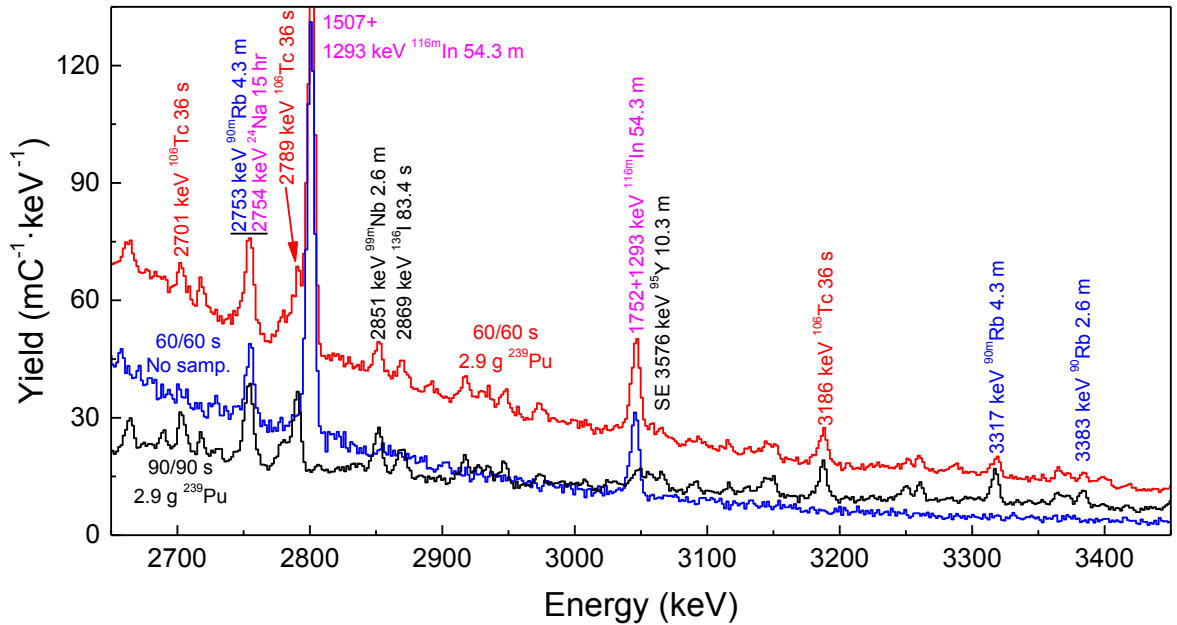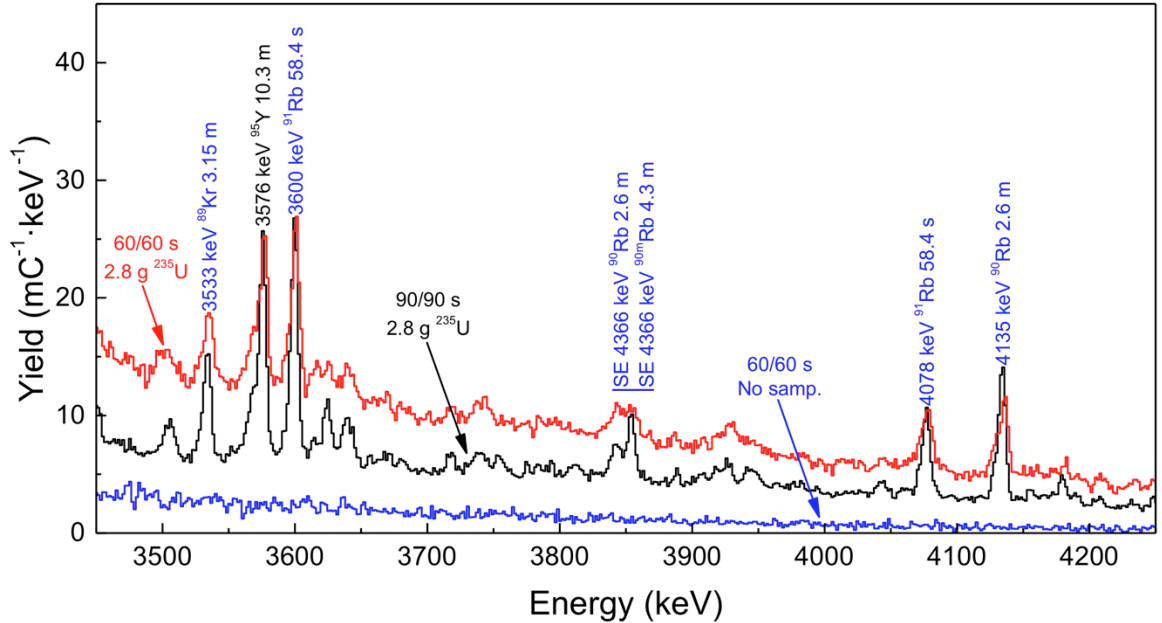
Figure 12b.   Delayed gamma-ray spectra from 3450 to 4250 keV for the ~2.8 g ^{235}U target irradiated by moderated neutrons. This figure compares the 90/90 sec (black) and 60/60 s (red) irradiation/detection periods. Overlaid on this graph is a spectrum without a fissile sample using a 60/60 s irradiation/detection periods (blue).   In the 90/90 sec irradiation/detection periods the fissile sample was shuttle from the irradiation position to the detection position. In the 60/60 sec irradiation/detection periods the fissile sample was stationary and the detector was in situ with the irradiation setup. The spectra are normalized to the total electron charge on the radiator as a proxy for the neutron fluence. The color code for the labels is the same as in figure 12a.

II.1.3. Measurement of Pu-241 Delayed Gamma-ray Signatures

The main goal of the experimental campaign was to measure the high-energy, delayed gamma-ray emission following thermal neutron induced fission of ^{241}Pu. In addition, delayed gamma-ray spectra of ^{239}Pu and combined targets of the two Pu isotopes and ^{235}U were measured to provide data for determining how well the isotopes could be distinguished in a delayed gamma assay. For all measurements 90/90 sec irradiation/spectroscopy cycle times were used that had previously been found to be well suited for distinguishing ^{239}Pu and ^{235}U. The samples were rapidly shuttled between the irradiation station and the location of the gamma-ray detectors (see Figure 13), which were in a separate, shielded room to prevented activation of the detector and of surrounding material, thereby mitigating interferences and minimizing the overall background.

The experimental setup used in this campaign was similar to that of previous experiments as seen in Figures 1 and 2. A pulsed S-band radiofrequency linac was operated at 15 MeV and its highest repetition rate of 264 Hz to maximize the fission yield in the relatively small ^{241}Pu sample. The ^{241}Pu target consisted of 254 mg ^{241}Pu with additional ~10 mg ^{239}Pu, ~154 mg ^{240}Pu, ~836 mg ^{241}Am and ~26 mg ^{242}Pu. The additional isotopes did not significantly contribute to the delayed gamma spectrum due to their much lower fission cross sections. The actinide sample was enclosed in a glass vial that was inside a aluminum container that was placed inside a sealed steel cylinder. Activation of the aluminum and of the manganese in the steel produced several strong ^{56}Mn and ^{28}Al peaks in the measured spectra as seen in Figure 14.
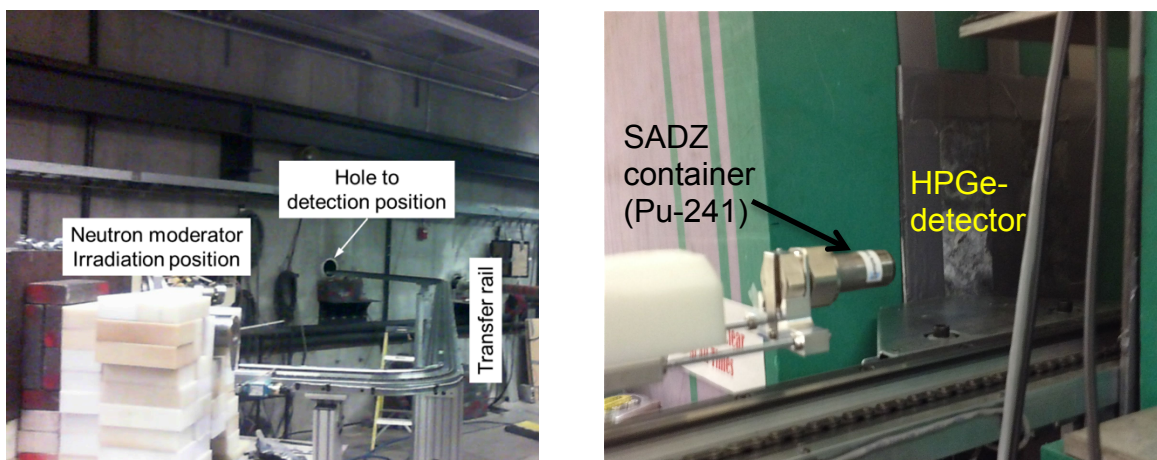
Figure 13. On left: Irradiation station. On right: SADZ (steel) container holding the ^{241}Pu sample near the delayed gamma measurement position in the spectroscopy room. Two HPGe detectors were positioned on either side of the track behind lead shielding and a LaBr$_3$ detector was mounted above the track.

After each 90 s irradiation period the target was transported to the measurement room via the automated transfer system in 17.5 s. Delayed gamma spectroscopy was performed with two 40% relative efficiency n-type HPGe detectors and a large LaBr$_3$(Ce) detector. The primary and the secondary HPGe detectors were positioned on opposite sides of the sample (see Figure 13) behind 6.35 mm thick Pb filters to attenuate low energy photons emitted from the target. The preamplifier signals were processed by an analog multi-parameter data acquisition system, which recorded both, energy and time information in an event-by-event mode. The HPGe data acquisition channels were configured for high-speed spectroscopy with a ~3.0 µs time constant, gated integrating amplifier and a 900 ns fixed dead time analog–to-digital converter. In addition, one of the other preamplifier outputs from the primary HPGe detector was sent to a fully digital Lynx (Canberra) data acquisition system.

The following targets were measured:
1. ^{241}Pu target, 254 mg
2. 254 mg of ^{241}Pu combined with 974 mg of ^{239}Pu
3. 254 mg of ^{241}Pu combined with 974 mg of ^{239}Pu and 2.8 g of ^{235}U.

An initial, preliminary data analysis has been performed. As seen in Figure 14, the ^{241}Pu spectrum is very similar to the ^{239}Pu spectrum but contains several additional peaks from the activation of Al and Mn in its aluminum and steel containers that must be excluded from the analysis. The identified delayed gamma-ray peaks appear in both spectra but at different strength. Table IV lists the integrated yields (preliminary) for the most prominent peaks for both isotopes. The ^{241}Pu/^{239}Pu ratios of the integrated yields (last column) vary between 1.2 and 0.5. The delayed gamma yields are also plotted in Figure 15 for easier visual comparison. The ^{106}Tc yield is higher for ^{241}Pu than for ^{239}Pu. In contrast, the yields for the Rb isotopes and ^{95}Y are lower for ^{241}Pu than for ^{239}Pu. These differences open the possibility of determining the relative ^{241}Pu and ^{239}Pu fractions in a mixed sample given sufficient counting statistics.
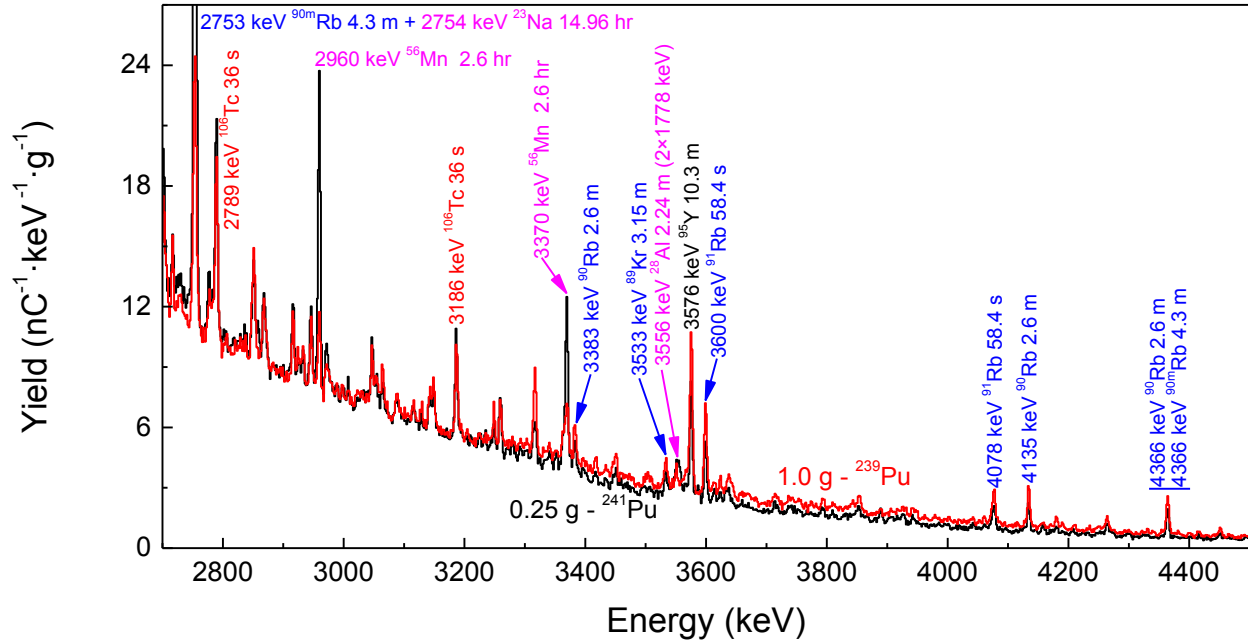
Figure 14. Delayed gamma-ray spectra from 2700 to 4500 keV for a targets containing ∼0.25 g ^{241}Pu (black line) and ∼1.0 g ^{239}Pu (red line) targets. The irradiation/spectroscopy times were 90/90 s and the total assay times ranged from 3 to 10 hr. The spectra are normalized to the total electron charge on the radiator as a proxy for the neutron fluence and the mass of the fissile constituent. The labels identify the likely fission fragment responsible for the discrete gamma-ray lines and several Mn and Al background lines (magenta) in the ^{241}Pu spectrum.

Table IV.   Integrated discrete delayed gamma-ray yields from the ^{241}Pu and ^{239}Pu targets (preliminary data).

| Discrete gamma-ray energy (keV)	^{241}Pu Discrete gamma-ray yield ($nC^{-1}\cdot g^{-1}$)	^{239}Pu Discrete gamma-ray yield ($nC^{-1}\cdot g^{-1}$)	^{241}Pu/^{239}Pu
2783 – ^{91}Rb	$(7.8\pm0.7)\times10^{-6}$	$(7.9\pm0.7)\times10^{-6}$	1.0
2789 – ^{106}Tc	$(4.60\pm0.09)\times10^{-5}$	$(3.92\pm0.09)\times10^{-5}$	1.2
2851 – ^{99m}Nb	$(1.74\pm0.08)\times10^{-5}$	$(2.15\pm0.08)\times10^{-5}$	0.8
2869 – ^{136}I	$(1.32\pm0.07)\times10^{-5}$	$(1.17\pm0.07)\times10^{-5}$	1.1
3186 – ^{106}Tc	$(2.23\pm0.07)\times10^{-5}$	$(1.90\pm0.07)\times10^{-5}$	1.2
3317 – ^{90m}Rb	$(8.8\pm0.6)\times10^{-6}$	$(1.90\pm0.07)\times10^{-5}$	0.5
3383 – ^{90}Rb	$(5.2\pm0.6)\times10^{-6}$	$(8.0\pm0.6)\times10^{-6}$	0.65
3533 – ^{89}Kr	$(3.9\pm0.4)\times10^{-6}$	$(5.1\pm0.5)\times10^{-6}$	0.76
3576 – ^{95}Y	$(2.62\pm0.06)\times10^{-5}$	$(3.81\pm0.07)\times10^{-5}$	0.69
3600 – ^{91}Rb	$(1.33\pm0.05)\times10^{-5}$	$(2.05\pm0.06)\times10^{-5}$	0.65
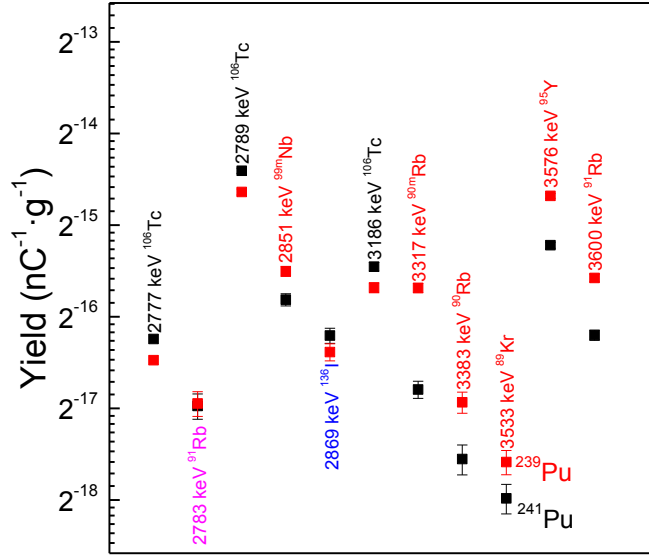
Figure 15. Integrated discrete delayed gamma-ray yields from the ^{241}Pu (■) and ^{239}Pu (■) targets. The yields are labeled with their energy and emitting fission fragment and ordered by gamma energy. The labels are color-coded in black for higher ^{241}Pu yield, in red for higher ^{239}Pu yield and blue for nearly identical yields. The 2783 keV discrete gamma-ray line from ^{91}Rb is color-coded magenta because the experimental data disagree with the expectation of a higher yield from ^{239}Pu. This needs to be further investigated and checked. The ^{106}Tc yield is higher for ^{241}Pu than for ^{239}Pu but the yields for the Rb isotopes and ^{95}Y are lower for ^{241}Pu than for ^{239}Pu.

II.2. Experiments at Oregon State University (OSU)

Several measurements were carried out at Oregon State University (OSU) on foils of fissionable material in a beam of thermal neutrons. These experiments allowed measurements of fission yields with a shorter half-life than those at IAC, and probed fission occurring under pure thermal neutron irradiation rather than the simulated reactor spectrum neutron irradiation of the IAC experiments.

II.2.1 Experimental Setup

Delayed gamma experiments were performed at OSU's 1.1 MWt TRIGA reactor with four available beam ports through the water tank and external radiation shields as schematically shown in Figure 16. Beam port #4 pierces the graphite neutron reflectors to allow a high thermal neutron flux. A bismuth filter in the port channel attenuates the gamma rays and x-rays; a sapphire filter preferentially attenuates the fast neutrons while passing the thermal neutrons. Lead and Boral rings are used to collimate the thermal neutron beam to a uniform 2 cm diameter within the target chamber. The neutron beam within the target chamber has a nearly uniform flux, with a thermal flux of 2.81(5) ·10^7 cm^{-2} s^{-1} and an epithermal to thermal flux ratio of 6.05(15)·10^{-4}. Neutrons passing through the target chamber encounter a beam stop and are absorbed [7].

The target chamber holds the sample during irradiation, and is viewed by a 36.5% relative efficiency co-axial high purity germanium (HPGe) detector at a distance of approximately 30 cm. This beam port and analysis station make up the Prompt Gamma Neutron Activation and Analysis (PGNAA) facility as seen in Figure 17. However, the delayed gamma-ray signal from beam-induced fission is too weak to give good data using the standard PGNAA setup. Consequently, a pneumatic

transfer line was installed to move irradiated samples from the beam to a location directly adjacent to the detector. The shuttle was made of high density polyethylene and would contain a foil of fissile material of a few tenths of a gram in mass. Transit times were 0.1 second.
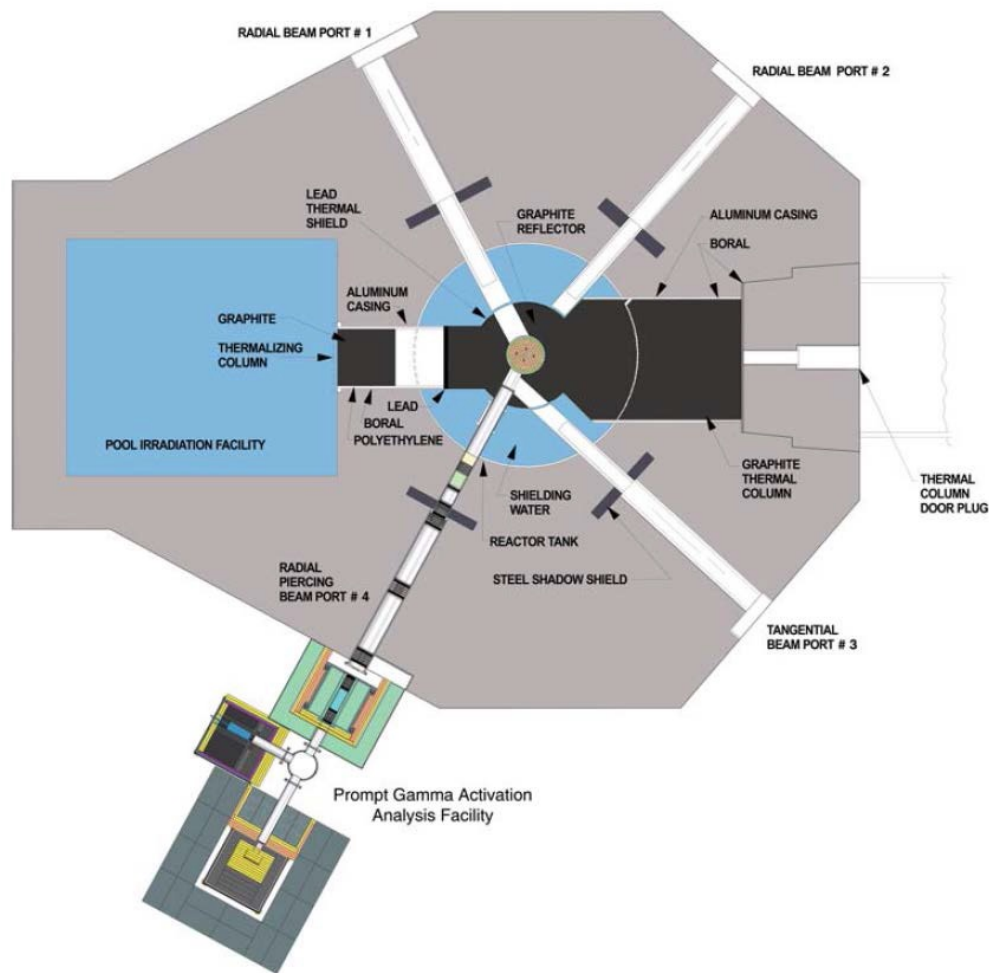
Figure 16. OSU's TRIGA reactor, showing beam ports and the PGNAA used during this investigation.
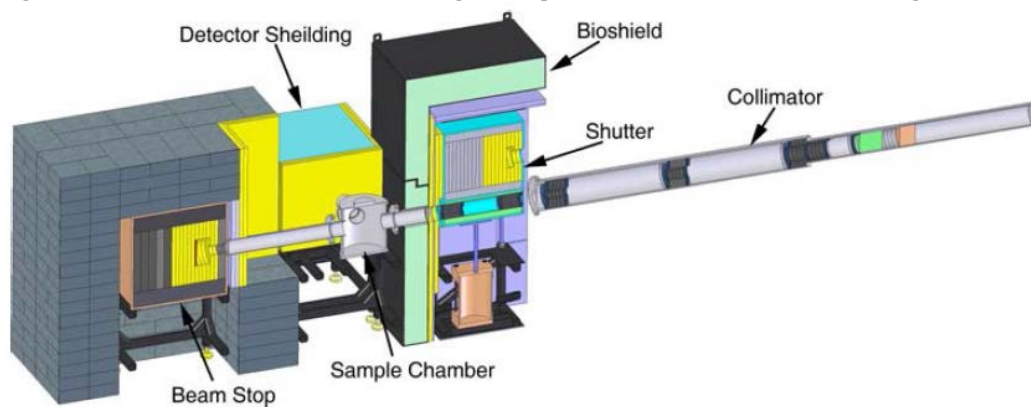
Figure 17. Schematic of beam port #4 and the PGNAA.

II.2.2 Delayed Gamma-ray Measurements

Two main groups of measurements were taken. In spring of 2012, several measurement sets were recorded using a 200 mg mass 93% enriched HEU foil. Of these, the set of measurements acquired on April 06, 2012, were the most useful, consisting of 5 sets of 20 cycles of 30 seconds of irradiation and 150 seconds of measurement. A measured delayed gamma spectrum is shown in Figure 18.

In June of 2014, additional sets of measurements were taken on the same HEU foil and on a 244.5 mg foil of 99.11% ^{239}Pu and on a DU sample. All samples were exposed to 20 cycles of 10 seconds of irradiation followed by 10 seconds of measurement, then 20 cycles of 1 minute of irradiation and 1 minute of measurement, and 12 cycles of 10 minutes of irradiation and 10 minutes of measurement. The 1 and 10 minute cycles gave spectra (Figures 19 and 20) with reasonable statistical noise and easily identifiable structures and peaks; the 10 second cycles contained enough noise that they are not visually revealing, whether statistically useful data on the very short-lived isotopes can be extracted from this information is as yet unknown as the data is still awaiting analysis.

29
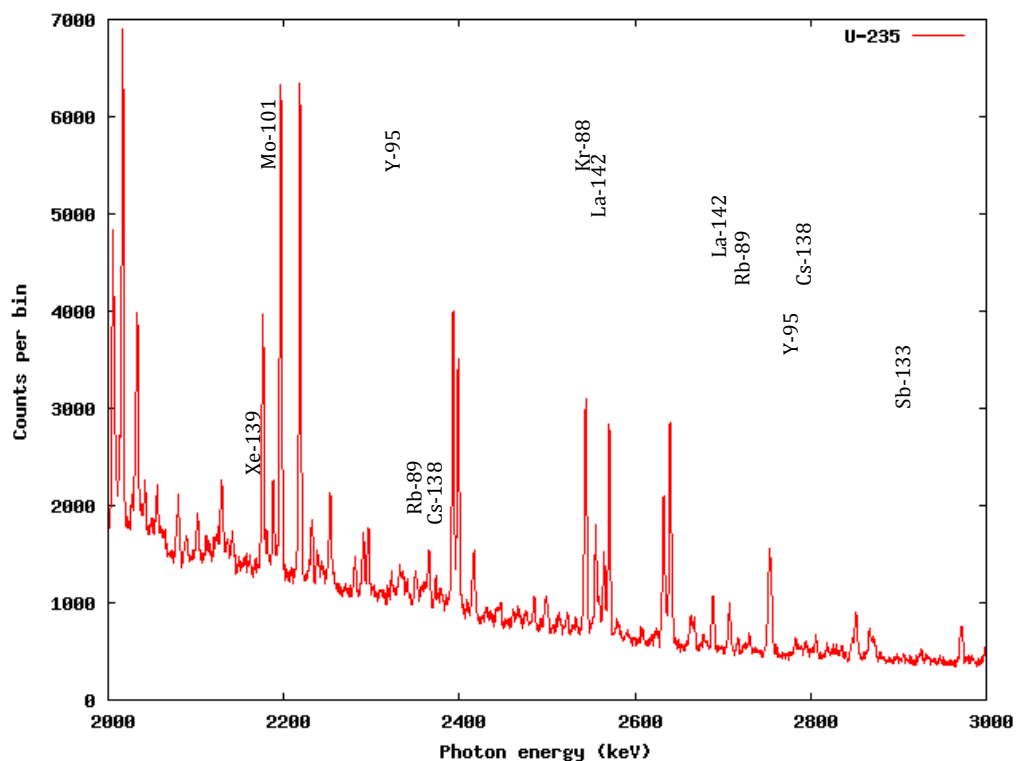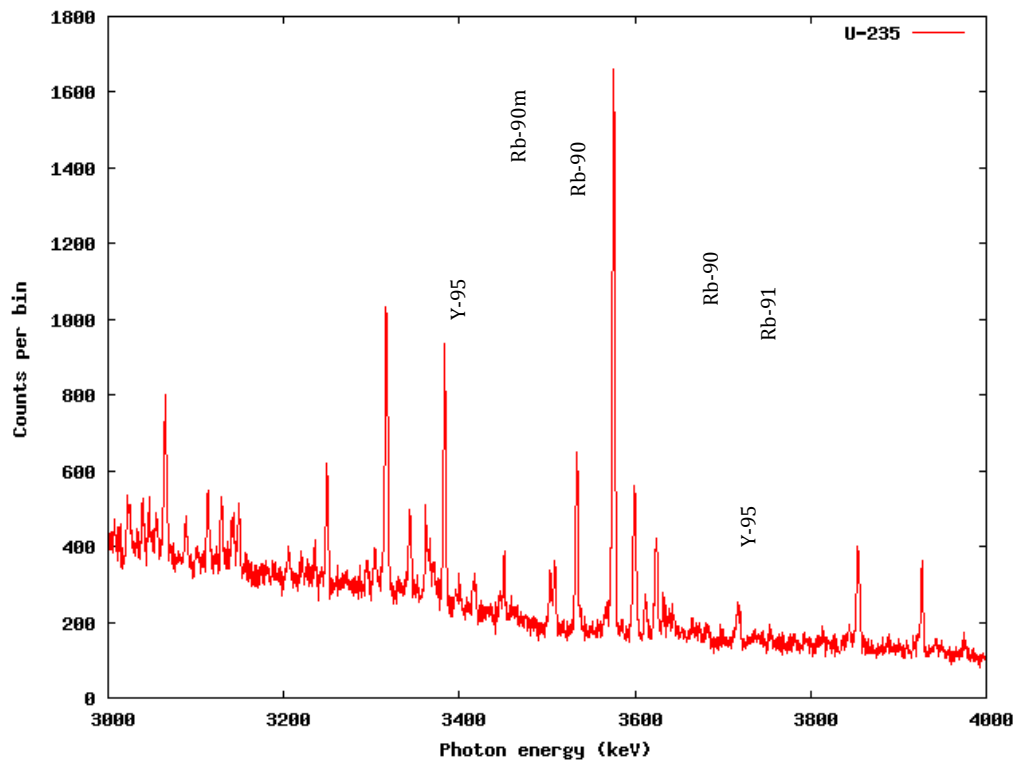
Figure 18. Delayed gamma spectra from thermal neutron irradiation of ^{235}U for 30 second irradiation, 150 second measurement cycles over the 2 to 4 MeV energy range. Many of the more prominent lines are labeled to show the fission product isotopes responsible.
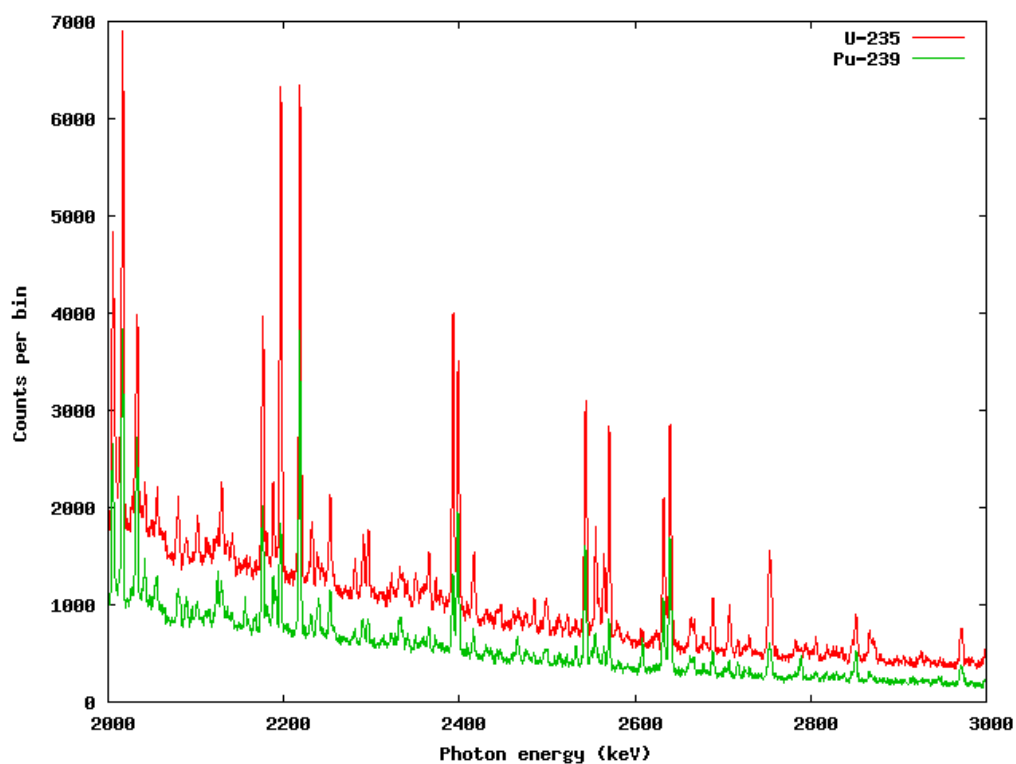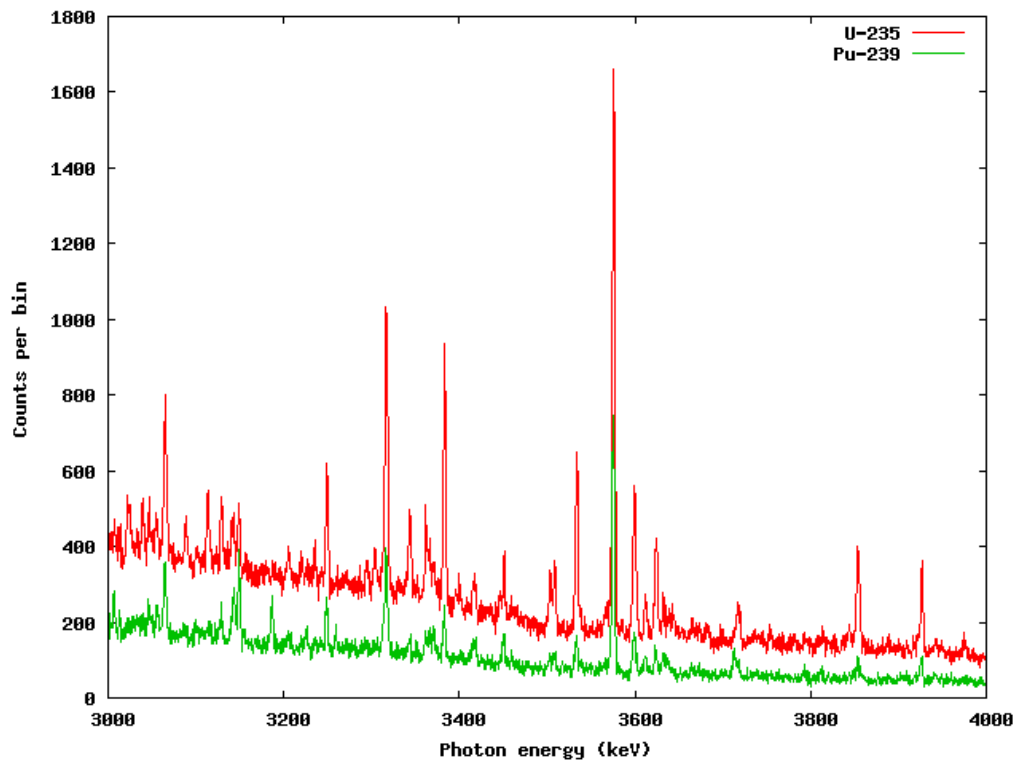
Figure 19. ^{239}Pu and ^{235}U delayed gamma spectra for 10 minute irradiation, 10 minute measurement cycles over the 2 to 4 MeV energy range. Differing relative peak heights allow ^{239}Pu and ^{235}U to be readily distinguished.
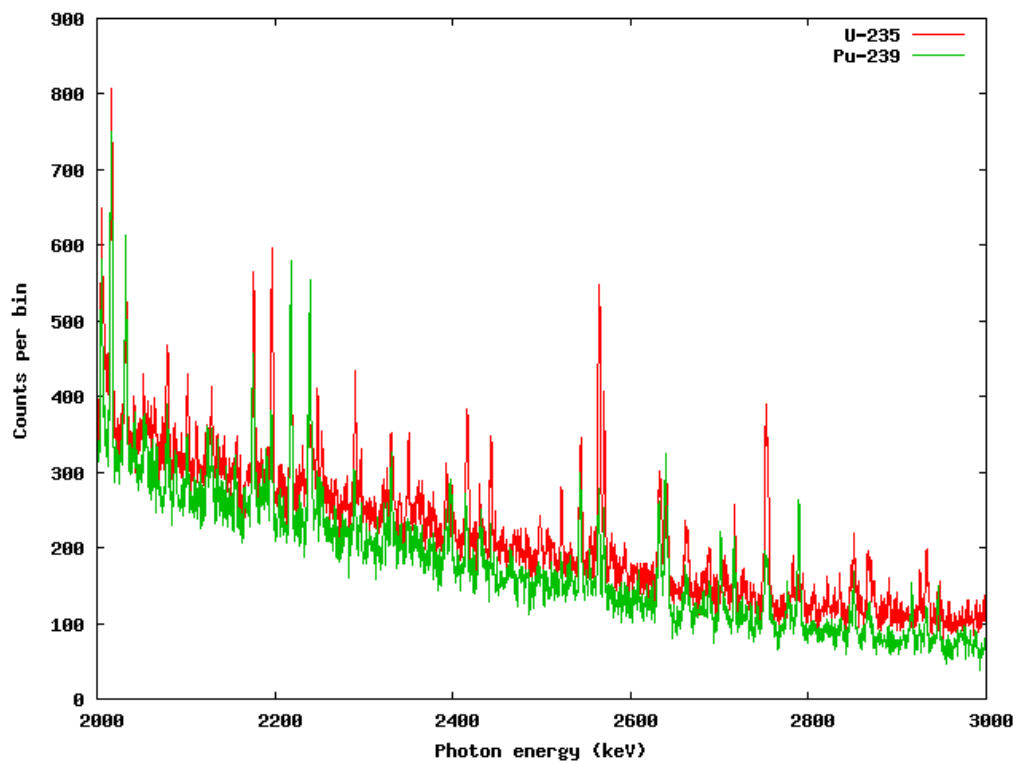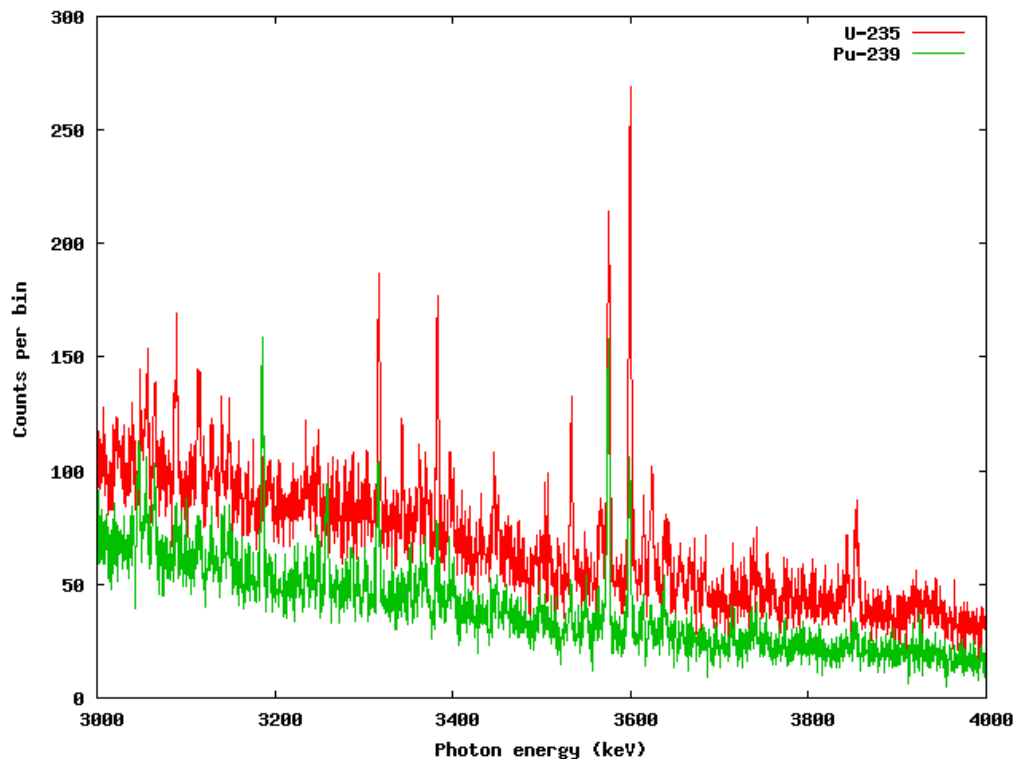
Figure 20. ²³⁹Pu and ²³⁵U delayed gamma spectra for 1 minute irradiation, 1 minute measurement cycles over the 2 to 4 MeV energy range. Although noisier than the 10 minute interval data, the two fissile isotopes can be distinguished and this data may help to pin down the yields of shorter-lived fission products.

II.3. Data Analysis

II.3.1. Determination of Fission Yields from Time-dependent Delayed Gamma-Ray Data

In order for the high-energy, delayed gamma-ray spectroscopy method to work well, the independent product yields have to be accurately known. However, fission yields of short-lived isotopes, i.e., with half-lives up to tens of minutes, listed in Evaluated Nuclear Data Files libraries have often large uncertainties in the range of tens of percent, or even factors of 2 or 3. A method has been developed for determining short-lived fission yields from the intensity and time dependence of the measured delayed gamma-ray emissions. More accurate fission yields will not only benefit safeguards applications but may also improve burnup-depletion codes used for reactor modeling or post-detonation forensics.

The analysis is possible because the delayed gamma data in the IAC and OSU experiments were recorded in list mode, i.e., time and energy of each gamma ray were recorded. Utilizing the time dependencies parent isotopes can be differentiated from their daughters and the contributions from different fission products with different half-lives to the same peak in the energy spectrum can be separated. In order to extract fission yields from the data, a physical model of a system of decaying and radiating isotopes interacting with the detector has been constructed. This model includes single and double escape peaks and simple fits to the background. The independent fission

yields, which are parameters in the physical model, were found by fitting the experimental data using a maximum-likelihood estimation method. Figure 21 shows a fit of the time dependence of the [91]Rb peak (3600 keV) count rate as an example.

The method was first applied to the delayed gamma data from the [235]U measurement at the Oregon State University. The physical model included 67 fission products. Isotope lifetimes and gamma-ray intensities were taken from the ENSDF library. The spectrum based on ENSDF/B-VI fission yields, and the spectrum based on fitted fission yields are compared in Figure 22 to the measured spectrum. Large discrepancies between the measured spectrum and the calculated one based on the ENSDF/B-VI data are clearly seen for a number of peaks indicating that some fission yields in the data libraries are very inaccurate. The spectrum based on the fitted fission yields reproduces the measurement much better. Figure 23 shows the fitted [235]U fission yields extracted from delayed gamma-ray measurements between 2.8 and 3.4 MeV and normalized to the cumulative [95]Y yield in comparison to the ENDF/B-VII data library values (blue line). The procedure is currently restricted to spectral regions with a linear energy dependence of the background so that the recorded data need to be broken up into multiple spectral regions for independent fitting. Future work should include fitting more data sets and larger energy ranges to improve the accuracy of the extracted fission yields. In addition, the fitting of the IAC and OSU data for [235]U, [239]Pu, and [241]Pu should be continued to extract improved fission yields for these nuclei.
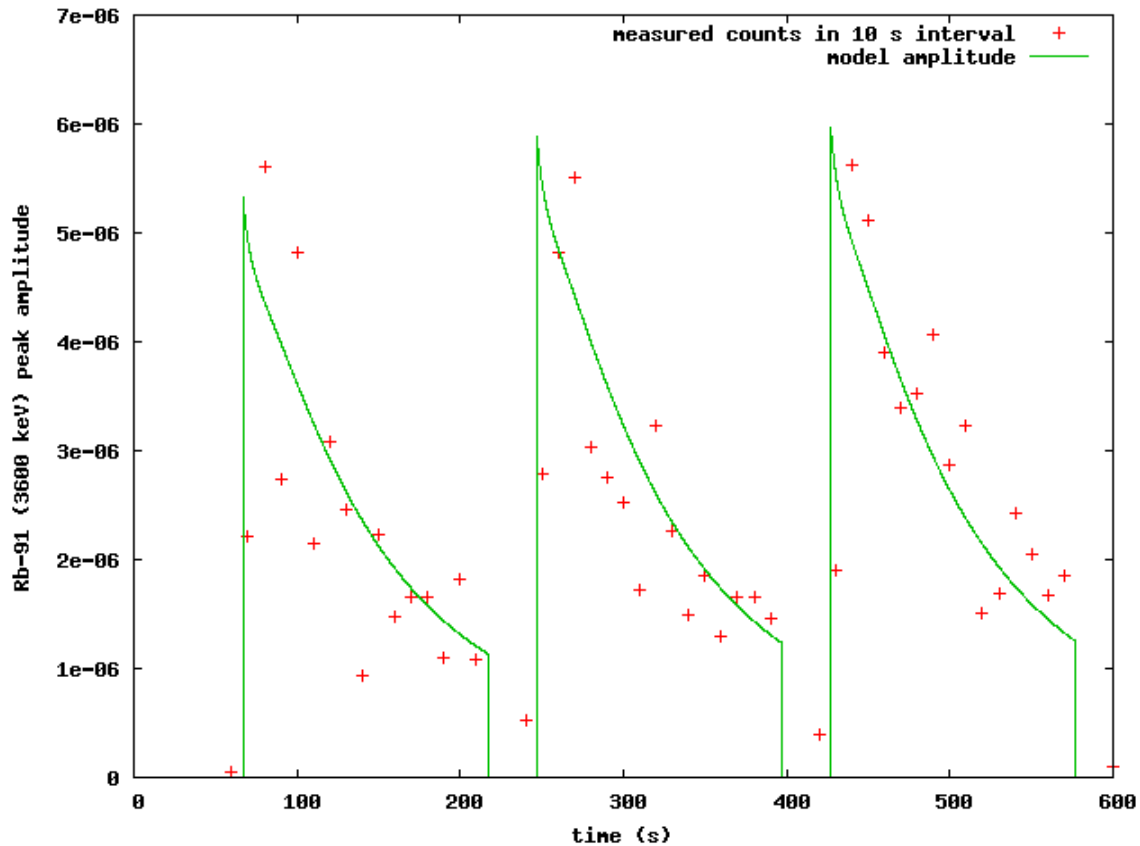
Figure 21. Fit of the time-dependence of the number of counts measured in 10 s intervals in the [91]Rb Peak at 3600 keV. The HEU sample was irradiated with thermal neutrons for 30 seconds and then counted for 150 seconds over 20 cycles with a HPGe detector. Only the first three cycles are shown.
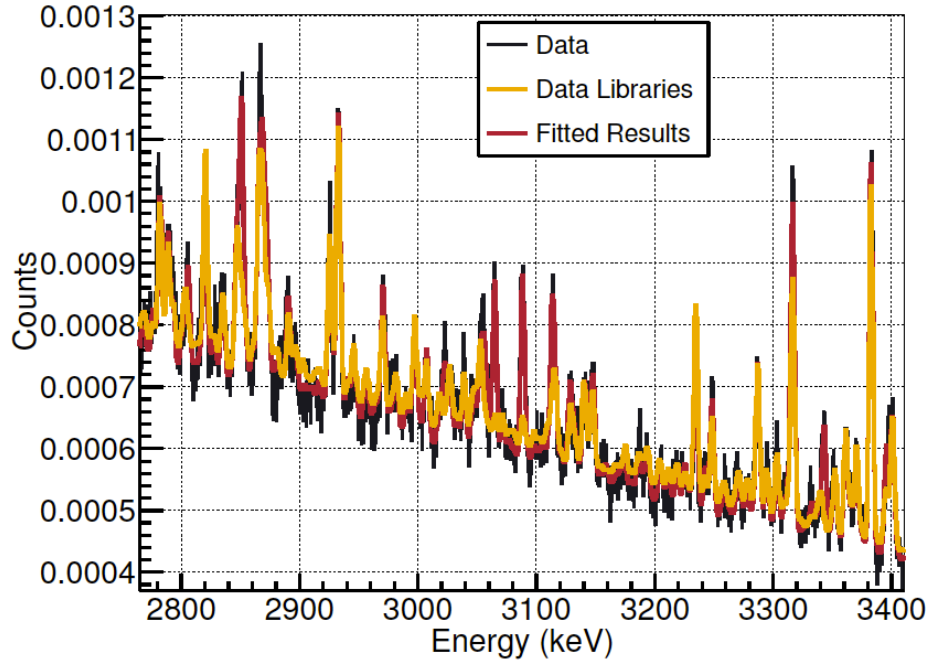
Figure 22. [235]U delayed gamma-ray spectrum measured at the Oregon State University from 2.8 and 3.4 MeV (black). Yellow and red lines show calculated spectra based on ENDF/B-VII data libraries (orange) and on the fitted fission yields (red).
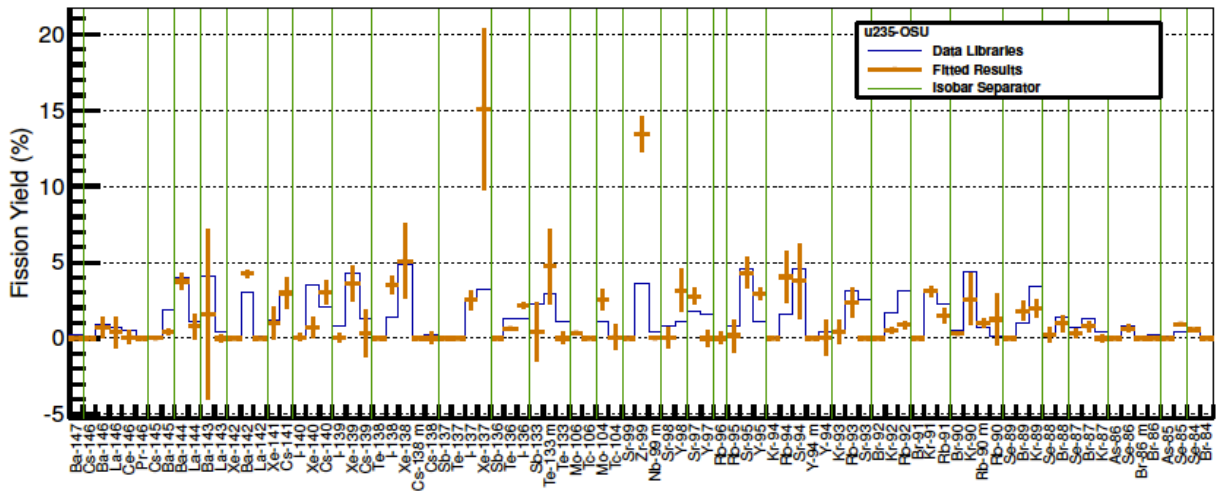
Figure 23. Fitted [235]U fission yields (orange) extracted from delayed gamma-ray measurements between 2.8 and 3.4 MeV normalized to the cumulative [95]Y yield, and ENDF/B-VII data library values (blue line). The large deviations for the [137]Xe and [99]Zr isotopes are due to overlapping gamma-ray peaks with similar half-lives.

The fission yield analysis has been described in detail by LW Campbell in the report PNNL-SA-99655 [8].

II.3.2. Determining Fissile Isotopic Fractions

As described in section II.1.2, numerous high-energy delayed gamma-ray lines from short-lived fission fragments were observed in the measured [235]U and [239]Pu spectra. The variation of [235]U/[239]Pu peak ratios, observed for all irradiation/spectroscopy cycle times, makes it possible to determine isotopic fractions from a delayed gamma measurement on an unknown mixture. The fission fragments producing stronger gamma-ray lines for [235]U included [89]Kr, [90]Rb, [90m]Rb and [91]Rb. All of these fragments have half-lives on the order of minutes and are clearly visible in the spectra for all measured irradiation/detection periods. The fission fragment strongly favoring [239]Pu, [106]Tc with a half-life of 36 s, produces strong lines at 2789 and 3186 keV at the shorter irradiation/spectroscopy cycles. Therefore, we focused our analysis on the 90/90 s irradiation/detection cycle data.

Several different techniques to deconvolve the spectra in order to extract the fissile constituents were investigated. The first approach tested was the Full Spectral Component Analysis (fSCA). This technique fits the measured spectra from mixed samples ($\Psi_{mix}(E_\gamma)$) as a linear combination of basis spectra from pure samples of [235]U ($\Psi_{235}(E_\gamma)$) and [239]Pu ($\Psi_{239}(E_\gamma)$) as written in the equation below.

$$\Psi_{mix}(E_\gamma) = \alpha_{235} \cdot \Psi_{235}(E_\gamma) + \alpha_{239} \cdot \Psi_{239}(E_\gamma),$$

The coefficients (α's) can be found by general linear regression techniques. The "Full Spectral" in fSCA refers to the utilization of a large contiguous section of the spectra. This technique has been applied quite successfully to delayed gamma-ray spectra from photo-fission and offers the potential advantage of better statistical results by utilizing the full signal embedded in the spectrum not just the counts in a few selected peaks. The agreement between the measured mixed sample spectra and the linear combinations appears to be quite good but the contribution of [239]Pu was over-predicted by ~10 percentage points at ~26% [239]Pu mass and by about half that amount at 51% [239]Pu mass. Possible causes for the observed deviations include spectral distortion due to increased detector count rate and pileup when fissile material was added.

The most robust method was the Peak Area Component Analysis (PACA) described below. For this method strong peaks with varying [235]U/[239]Pu ratios are selected for analysis. In order to work well, the peak areas must be carefully integrated. Using standard sideband subtraction or fitting a single Gaussians to a discrete gamma-rays line in order to extract the integrated yield proved to be problematic because of the rich and complex nature of the spectra. Many of the gamma-ray lines of interest are closely spaced and/or overlap, making baseline regions difficult to find for sideband subtraction and leading to poor single Gaussian fits. Hence, a multiple Gaussian fitting technique was developed to extracted the integrated yield from these rich and complex spectra. While multiple Gaussian fitting can lead to inconsistent results because the strong correlation between fit parameters, in this case the fit parameters can be highly constrained by the following:
- **Gaussian centroid**. The gamma-ray energies emitted by the fission fragments are known and available in the Table of Isotopes, ENSDF [6,9].
- **Gaussian standard deviation**. The energy resolution of the HPGe detector was well characterized.
- **Branching ratio**. The gamma-ray branching ratio from the fission fragments are known and available in the Table of Isotopes, ENSDF [6,9].
- **Detection efficiency**. The detection efficiency of the HPGe detector was well characterized.

These constraints allow the multiple Gaussian equation representing the spectrum to be written as

$$\Phi(E_\gamma) = \sum_f Y_f \cdot \left[\sum_l \varepsilon(E_{fl}) \beta_{fl} \frac{1}{\sigma(E_{fl})\sqrt{2\pi}} e^{-\frac{E_\gamma - E_{fl}}{2\sigma(E_{fl})^2}} \right] + \Phi_{bk}(E_\gamma) \qquad (11)$$

where the first sum is over the fission fragments of interest and the second sum is over the gamma-ray emission energies, E_{fl}. The indexes refer to the lth gamma-ray from the fth fission fragment. Furthermore, $\varepsilon(E_{fl})$ is the absolute detector efficiency, β_{fl} is the branching ratio, $\sigma(E_{fl})$ is the standard deviation (i.e. detector resolution) and $\Phi_{bk}(E_\gamma)$ is an equation that describes the spectrum's baseline. If enough fission fragments are considered and the relative intensities of the discrete delayed gamma-ray lines from a single fission fragment are coupled through $\varepsilon(E_{fl})$ and β_{fl}, a large energy region in the spectrum can be fit with the fission yields, Y_f, and the baseline, $\Phi_{bk}(E_\gamma)$, as the only free parameters. In practice, Equation (11) was applied to small energy regions (e.g. $\Delta E_\gamma \approx 60$ keV), which contained only a few discrete gamma-ray lines. Within these small regions, the detector efficiency, $\varepsilon(E_{fl})$, was considered a constant and the spectrum background, $\Phi_{bk}(E_\gamma)$, was assumed to be linear. This decoupled the relative gamma-ray line intensities from a single fission fragment when they were not in the same small region. Hence the Y_f's are not fission fragment yields but are instead discrete gamma-ray line intensities.
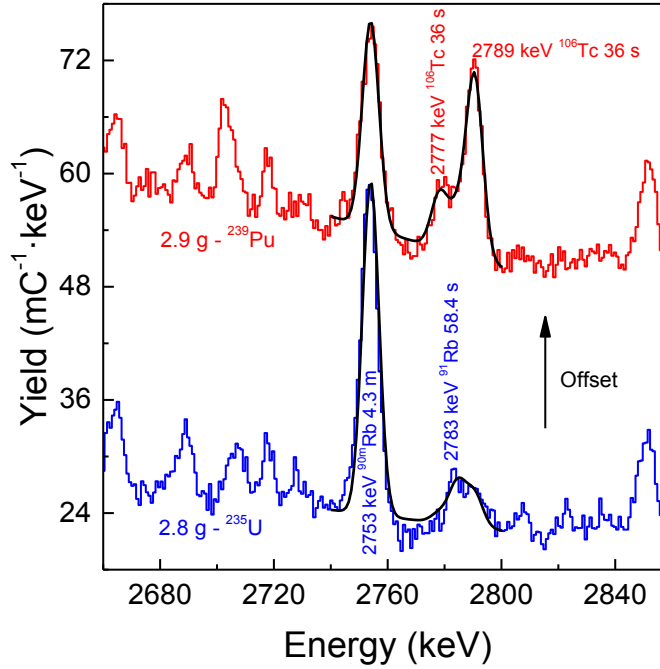
Figure 24. Delayed gamma-ray spectra from 2660 to 2860 keV for targets containing ~2.8 g of ^{235}U (blue) or ~2.9 g of ^{239}Pu target (red) irradiated by moderated neutrons. Overlaid on these spectra are the fits (black lines) from the multiple Gaussian fitting technique encapsulated in Equation (11). The irradiation/detection periods were 90/90 s and the total data collection time was ~1.62 hr. The ^{235}U spectrum is artificially shifted up to allow an easy comparison of the two spectra.

The multiple Gaussian fitting technique was applied to 12 gamma-ray lines from 8 different fission fragments. One of the more challenging small energy regions is presented in Figure 24, which compares the multiple Gaussian fits to spectra from the pure 2.8 g ^{235}U and 2.9 g ^{239}Pu samples. In addition to the primary gamma-ray lines at 2753 keV, ^{90m}Rb, and at 2789 keV, ^{106}Tc, this region also contained minor gamma-ray lines at 2777 keV from ^{106}Tc and 2783 keV from ^{91}Rb. The relative intensity between the two ^{106}Tc lines at 2777 and 2789 keV were coupled through
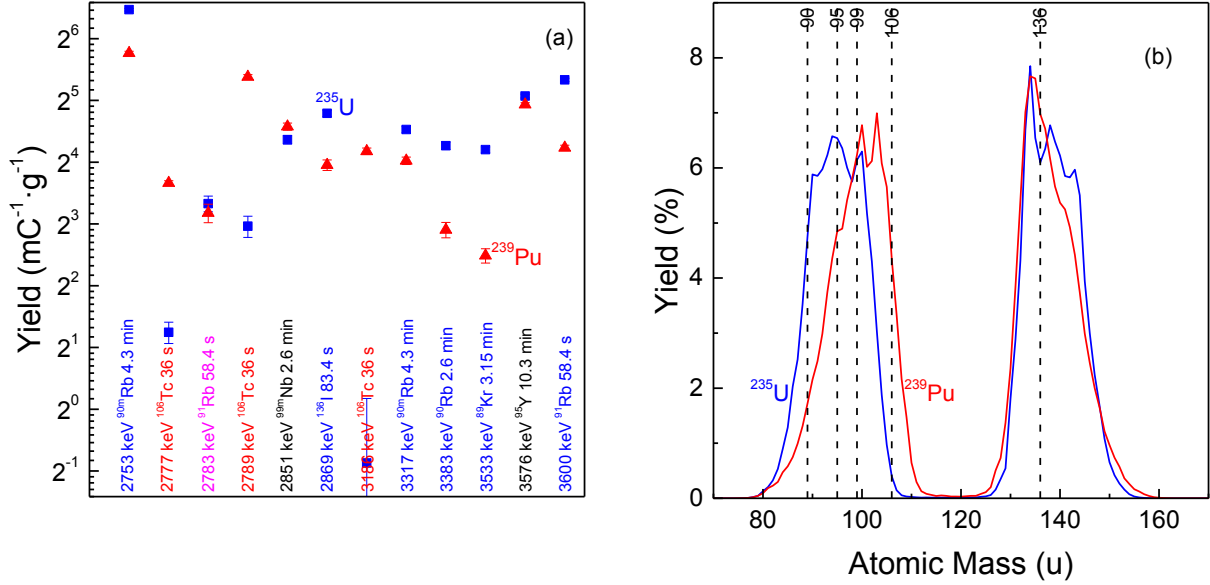
Figure 25. Integrated gamma-ray line yields from the 2.8 g ^{235}U (■) and 2.9 g ^{239}Pu (▲) samples utilizing the 90/90 s irradiation/detection periods (a) and the independent fission mass yields for ^{235}U (blue line) and ^{239}Pu (red line) from ENDF/B-VII.1 database [5]. In (a) the integrated yields are labeled with their energy and emitting fission fragment and ordered by gamma-ray energy. The labels are color-coded with blue for higher ^{235}U yield, red for higher ^{239}Pu yield and black for nearly identical yields. The 2783 keV discrete γ-ray line from ^{91}Rb is color-coded magenta because the experimental data disagrees with the expectation of a higher yield from ^{239}Pu.

their branching ratios, β_{fl}, which were 2.9% and 7.9% respectively. The multiple Gaussian fits look suitable with the largest discrepancy in the baseline region between the 2753 and 2777/2783 keV lines. However, in this region, the multiple Gaussian fit is only ~9% above the data. The integrated yields for all 11 gamma-ray lines are plotted in Figure 25 and are labeled with their corresponding fission fragment. The strongest ^{239}Pu fission indicator was the 3186 keV gamma-ray line from ^{106}Tc. This line is in a clean section of the spectra so that the integrated yield from the pure 2.8 g ^{235}U sample was statistically equivalent to zero. The other two gamma-rays from ^{106}Tc at 2777 and 2789 keV have interferences from ^{91}Rb, which is a strong indicator of ^{235}U fission and hence are only ~5.3 time larger from ^{239}Pu fission. The strongest ^{235}U fission indicator was the 3533 keV discrete gamma-ray line from ^{89}Kr, which was ~3.2 times larger for ^{235}U than ^{239}Pu. Other strong indicators of ^{235}U fission included the 3383 keV gamma-ray line from ^{90}Rb and the 3600 keV gamma-ray line from ^{91}Rb, which where ~2.6 and ~2.1 times larger from ^{235}U fission, respectively. There is one discrepancy, the gamma-ray line at 2783 keV from ^{91}Rb has an integrated yield that is approximately equal from ^{235}U and ^{239}Pu fission. However, this gamma-ray was in the ^{91}Rb ^{106}Tc triplet shown in Figure 24 and the multiple Gaussian fitting technique cannot resolve its contribution. Finally there are two lines, at 2851 from ^{99m}Nb and 3576 keV from ^{95}Y, with integrated yields that do not differ drastically between ^{235}U and ^{239}Pu fission.

Eleven of the twelve gamma-ray lines in Figure 25a are from fission fragments in the low-mass lobe of the fission fragment distribution. Consistent with the fission fragment mass distribution shown in Figure 25b, the strong indicators of ^{235}U fission were emitted by fragments with atomic masses on the lower edge of the low-mass lobe (^{89}Kr, ^{90}Rb and ^{91}Rb). In contrast, the strong indicator of ^{239}Pu fission is a fragment with an atomic mass on the higher edge of the low-mass lobe (^{106}Tc). As the mass of the initial fissioning isotope increases, the low-mass lobe shifts upwards to accommodate this increase in nuclear mass because the high-mass lobe is pinned by completely

filled nuclear shells with 50 protons or 82 neutrons for an atomic mass of 132 u. The isotopes ^{235}U and ^{239}Pu differ in nuclear mass by 4 nucleons and the low-mass centroid shifts this amount from ~95 u to ~99 u. The two fission fragments ^{99m}Nb and ^{95}Y, whose integrated yields do not differ drastically, are in the middle of the low-mass lobe.

In addition to collecting spectra from the pure 2.8 g ^{235}U and pure ^{239}Pu samples, spectra were also collected from mixtures of these two fissile isotopes, allowing data analysis techniques, which can determine the fissioning constituent, to be tested. Figure 26 shows the delayed gamma-ray spectra between 2650 and 5850 keV from the pure 2.8 g ^{235}U, 2.8 g ^{235}U + 1.0 g ^{239}Pu, 2.8 g ^{235}U + 2.9 g ^{239}Pu and pure 2.9 g ^{239}Pu samples for the 90/90 s irradiation/spectroscopy measurements. Spectra have been overlaid (in red) on the combined targets showing the superposition spectra formed by linear combination of the pure spectra with the weight of each determined by the peak area contribution analysis.

Figure 26a. Delayed gamma-ray spectra from 2750 to 3450 keV for targets containing 2.8 g ^{235}U, 2.8 g ^{235}U + 1.0 g ^{239}Pu, 2.8 g ^{235}U + 2.9 g ^{239}Pu and 2.9 g ^{239}Pu using the 90/90 s irradiation/detection period. The spectra are normalized to the total electron charge on the radiator as a proxy for the neutron fluence and an artificial offset has been added to distinguish spectra from different samples. Each spectrum's respective sample has been labeled near the corresponding spectrum. Spectra have been overlaid (in red) on the combined targets showing the superposition spectra formed by linear combination of the pure spectra with the weight of each determined by the peak area contribution analysis.
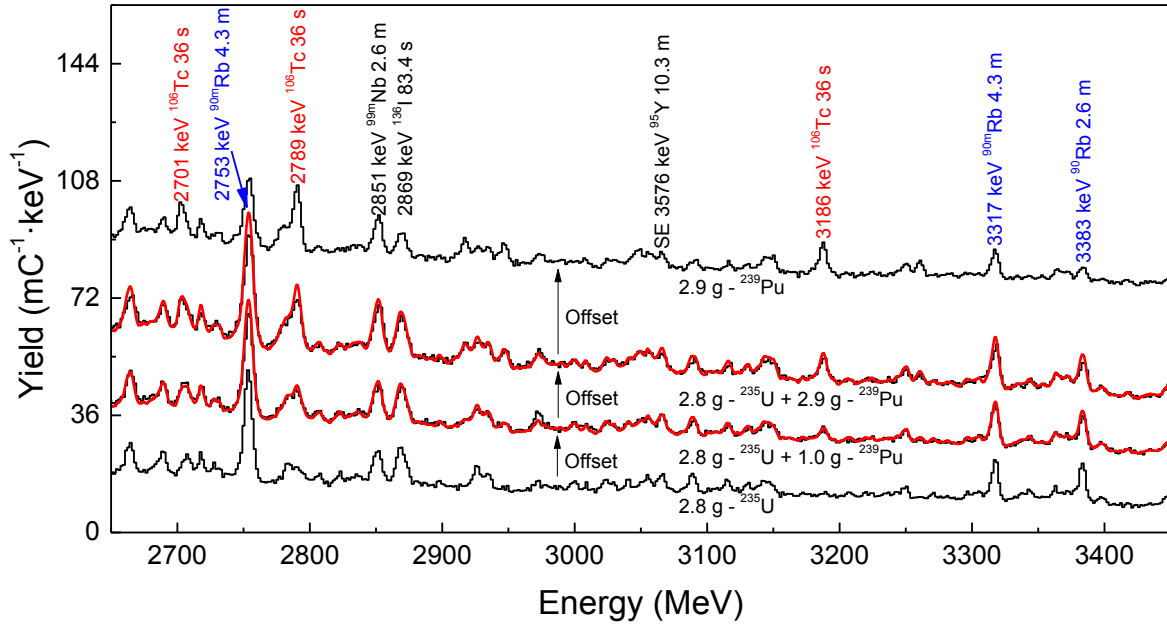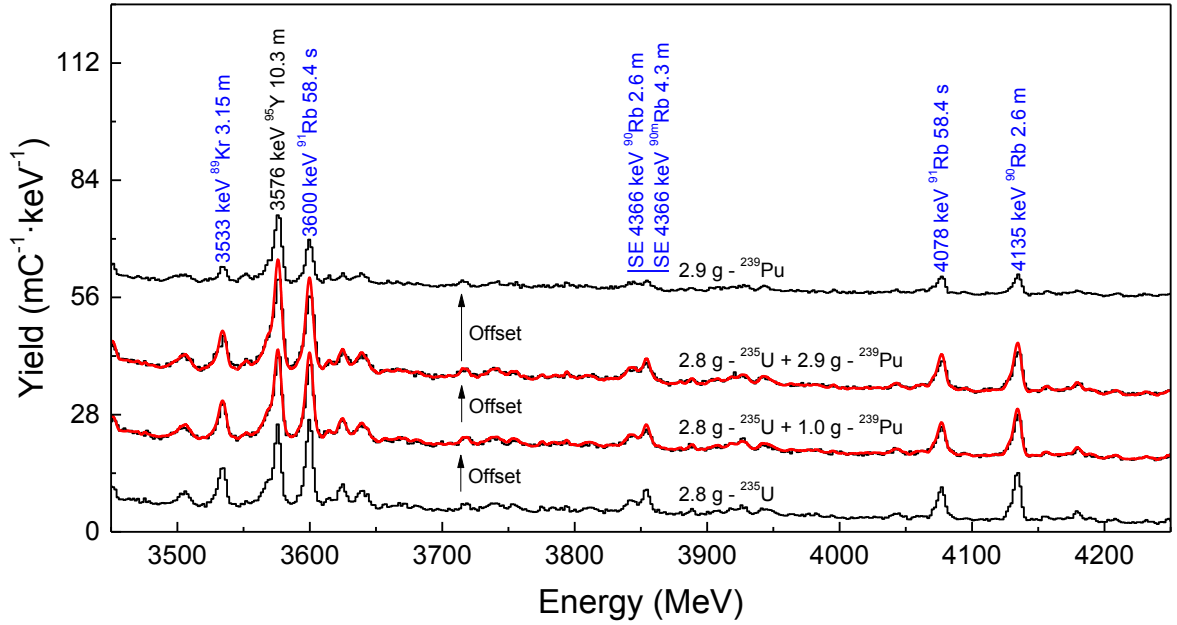
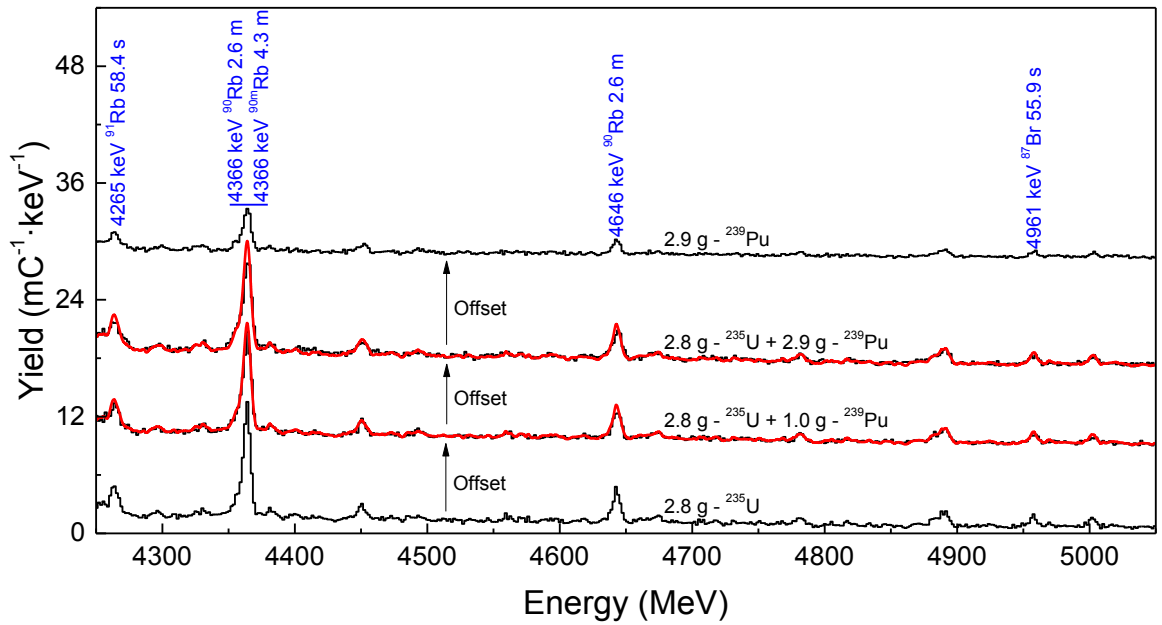Figure 26b. Delayed gamma-ray spectra as in Figure 26a but from 3450 to 4250 keV.

Figure 26c. Delayed gamma-ray spectra as in Figure 26a but from 4250 to 5050 keV.
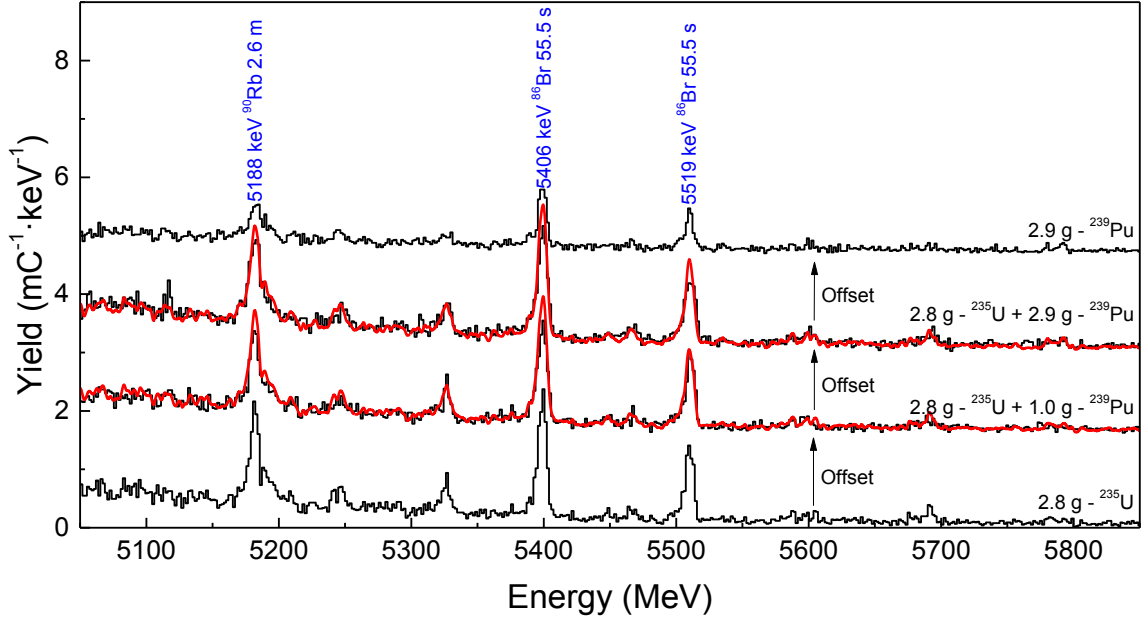
Figure 26d. Delayed gamma-ray spectra as in Figure 26a but from 3450 to 4250 keV.

A more detailed look reveals that adding ^{239}Pu to ^{235}U caused the strong ^{239}Pu indicators gamma-ray lines at 2789 and 3186 keV from ^{106}Tc to increase in intensity. In a similar fashion, adding ^{235}U to ^{239}Pu caused the strong ^{235}U indicator gamma-ray lines at 3383, 3533 and 3600 keV from ^{90}Rb, ^{89}Kr and ^{91}Rb to increase in intensity. In a counterintuitive fashion, however, the strong indicators from ^{235}U or ^{239}Pu decrease intensity when the mass of one of the fissile isotopes (e.g. ^{235}U) was held constant and the other fissile isotope (e.g. ^{239}Pu) was added. This can be most easily seen by comparing the intensity of the strong ^{235}U indicators at 3383, 3533 and 3600 keV for the pure 2.8 g ^{235}U sample and the 2.8 g ^{235}U + 1.0 g ^{239}Pu combined sample with all of these gamma-ray lines decreasing in intensity with the addition of 1.0 g of ^{239}Pu. Figure 27 shows the decrease of the integrated yield of the strong ^{235}U fission indicator at 3533 keV by 32% as ^{239}Pu mass is increased to 2.9 g. This can be understood by examining two limiting cases.

In the small-mass limit, the fission yield of each constituent is linear proportional to the isotopic yield so that the gamma-ray yield is given by

$$Y_\gamma = \frac{dY_\gamma}{dm_{235}} \cdot m_{235} + \frac{dY_\gamma}{dm_{239}} \cdot m_{239} \tag{12}$$

where dY_γ/dm_{235} and dY_γ/dm_{239} are the differential gamma-ray yields per unit fissile mass. Hence, the addition of ^{239}Pu to a constant mass of ^{235}U should cause the gamma-ray yield to increase linearly with the ^{239}Pu mass. Based on the 3533 keV integrated yield data, this relationship is presented in Figure 27 and does a poor job describing the observed yields. In the high-mass limit, there is enough fissile mass that every neutron causes fission and the addition of more fissile mas does not increase the amount of fission. The gamma-ray yield is then proportional to the relative fraction of the fissile constituents

$$Y_\gamma = \frac{dY_\gamma}{df_{235}} \cdot \frac{m_{235}}{m_{235} + m_{239}} + \frac{dY_\gamma}{df_{239}} \cdot \frac{m_{239}}{m_{235} + m_{239}} \tag{13}$$

40

where dY_γ/dm_{235} and dY_γ/dm_{239} are the differential gamma-ray yields per unit fissile mass. Based on the 3533 keV integrated yield data, this relationship is presented in Figure 27 and describes the observed yields well. This second limiting case neglects neutrons generated in the sample itself, which can cause additional fission reactions.
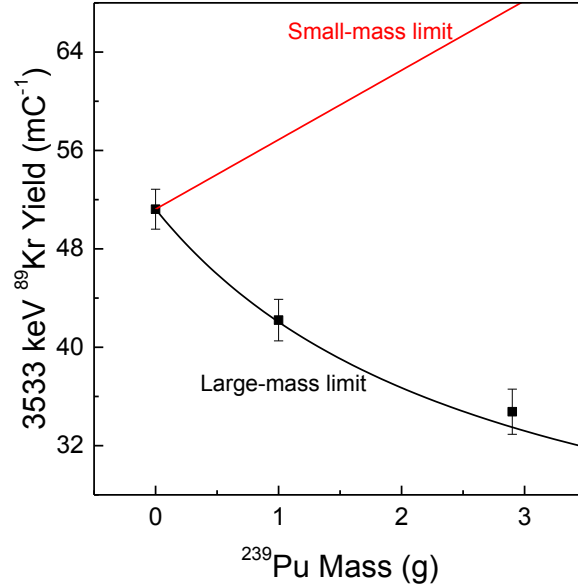

Figure 27. Integrated gamma-ray line yield for the strong [235]U fission indicator at 3533 keV from [89]Kr as a function of [239]Pu using the 90/90 s irradiation/detection periods. The [235]U mass was a constant of 2.8 g.

The research team investigated a variety of different techniques to deconvolve the spectra in order to extract the fissile constituents. The most robust method was Peak Area Component Analysis (PACA). This technique basically applies a super position principal to a vector of integrated gamma-ray line yields in the form of

$$\Phi_{mix} = \alpha_{235} \cdot \phi_{235} + \alpha_{239} \cdot \phi_{239},$$

where ϕ_{235} and ϕ_{239} are the basis vectors from pure samples of [235]U or [239]Pu with the α's being the required mixing to obtain the spectrum from the sample containing [235]U and [239]Pu. The α's can then be found by general linear regression techniques. This simple technique was applied to the four spectra presented in Figures 26a-d. The integrated γ-line yields from the pure 2.8 g [235]U and 2.9 g [239]Pu samples were used to form the basis vectors. The integrated gamma-ray yield vectors included 11 of the 12 gamma-rays presented in Figure 25a with the 2783 keV line from [91]Rb being excluded because of the interference from the 2777 and 2789 keV lines of [106]Tc. Figure 28 shows the relative [239]Pu spectral contribution, $\alpha_{239}(\alpha_{235} + \alpha_{239})^{-1}$, as a function of the relative concentration of [239]Pu in the samples. Of course, at the extremes of the pure [235]U and [239]Pu samples the spectral contributions are perfect because the basis vectors are the same as Φ_{mix} leaving only the two mixed samples with interesting results. The statistical errors were ~5% with a maximum deviation of ~9% for the sample containing 2.8 g of [235]U and 2.9 g [239]Pu. For this sample, the relative [239]Pu spectral contribution was only 1.9 standard deviations above the actual [239]Pu in the sample. The spectral contribution α's can also be used to form a linear combination of the spectra from the pure 2.8 g [235]U and pure [239]Pu samples to generate a predicted mixed spectrum. These predicted spectra are overlaid in Figures 26 with good agreement between the measured spectra and the linear combination.
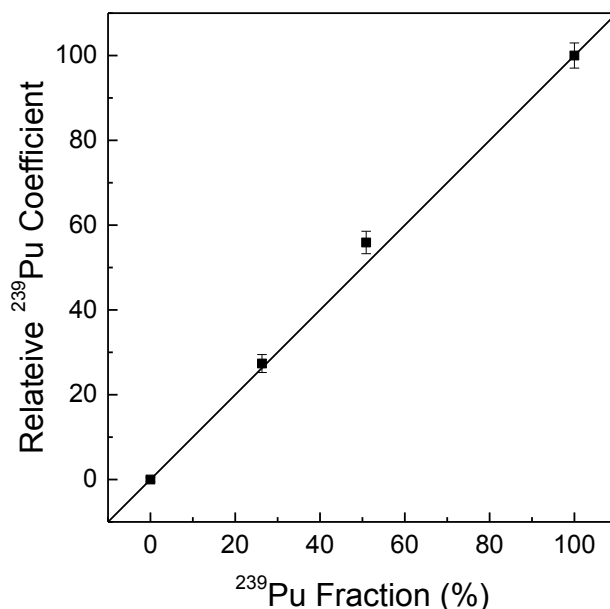
Figure 28. Relative [239]Pu spectral contribution versus the [239]Pu fraction of the fissile mass in the sample. The spectra used in this analysis are presented in Figure 26. These spectra were collected with the 90/90 s irradiation/detection period. Overlaid on this data is unity line to represent expectations.

II.4. Delayed Gamma Experiments on Mockup Assembly

For further experimental testing of the delayed gamma-ray method, measurements were extended from U and Pu targets of several grams to a mock-up assembly. Measurements were performed on several configurations of low-enriched and depleted uranium pins as a first step towards developing assembly scale methods and to provide data for validating modeling codes at the assembly level.

The experiments were performed in a hot cell at LANL over a period of several days. A $2 \cdot 10^8$ n/s DT neutron generator was used to irradiate the assembly and induce fission. The delayed gamma spectra were recorded with an HPGe detector, read out with a Lynx's Canberra MCA, and a LaBr$_3$ scintillation detector, read out with a nanoMCA. Also recorded were prompt gamma-ray spectra during the irradiation periods. Available for the measurements were 120 LEU rods (3.2% enriched) and 84 DU rods that could be inserted into a 15 x 15 assembly rack. In addition, a [239]Pu source was used that consisted of 60 g Pu-oxide (~90% [239]Pu) inside a sealed cylinder of about 12 cm in diameter and 16 cm in length. Several configurations were measured using irradiation/spectroscopy times of 1/1 min, 5/5 min and 15/15 min. Measurements were performed with the assembly in water (LEU and DU rods only) as seen in Figures 29 and 30 and also with the assembly in air. For the in-air setup assembly and neutron generator were surrounded by several inches of poly, as seen in Figure 31, to moderate the fast neutrons from the generator and to maximize the flux of thermal neutrons in the assembly. The in-air setup allowed the use of the [239]Pu source. For a measurement of the combined delayed gamma emission from [235]U, [238]U, and [239]Pu the Pu source was placed on the detector side of 5 rows of LEU rods. Also measured in air were a combination of LEU and DU rods and the LEU, DU, and Pu separately.

42
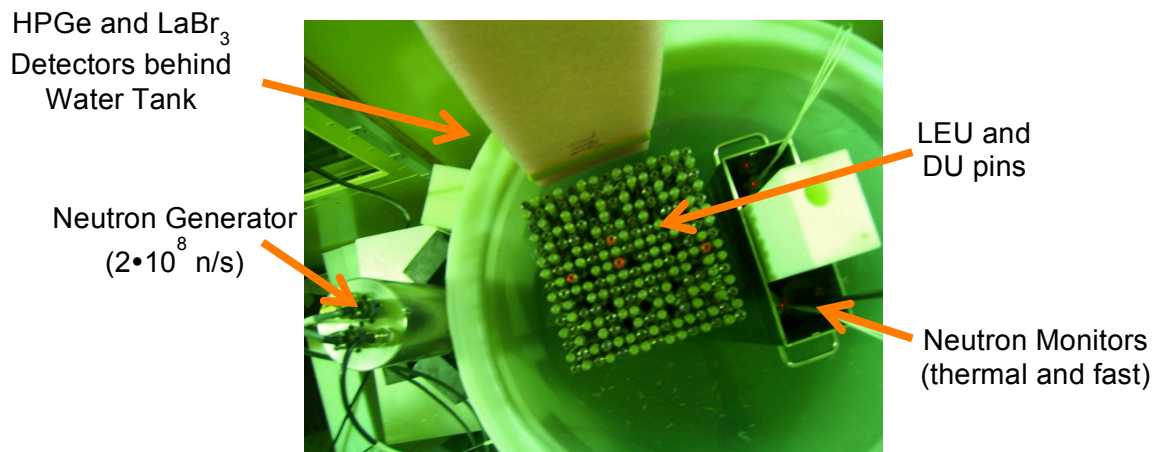
Figure 29. Setup for mock-up fuel assembly experiments at LANL with assembly in water. A set of neutron flux monitors was placed next to the assembly. One tube was placed "bare" into the steel container, the other one was placed inside a polyethylene block for monitoring the fast neutron component.
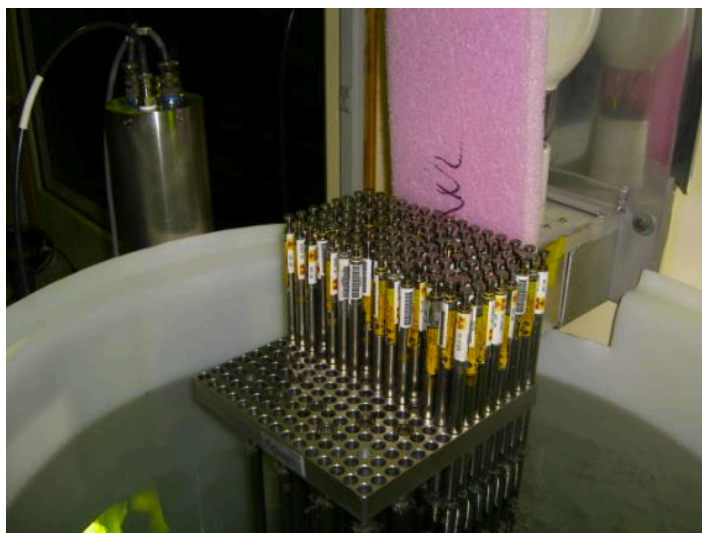
Figure 30: Half-filled assembly rack for "in-water" measurement.

Figure 31. Set up used during the irradiation in air. Polyethylene was used as moderator and some blocks of lead served as neutron reflectors around the generator.

A main objective of the mockup assembly experiments was the generation of assembly level data for benchmarking of the developed modeling code package. Measured spectra are being compared to model predictions. The data for different LEU/DU combination (i.e., different amounts of ^{235}U) and different neutron generator & moderator configurations will give information about measurement sensitivity and neutron coupling efficiency between neutron generator and assembly.

While generally good quality spectra were recorded for sets of LEU, DU pins, the Pu signal was too weak to provide statistically acceptable data. Because the Pu source originally selected for this experiment could not be made available due to a lacking authorization for using the source at the experiment location, a 10 times weaker replacement Pu source had to be used. Figures 32 a,b,c show sample spectra measured for assemblies of LEU and DU pins.
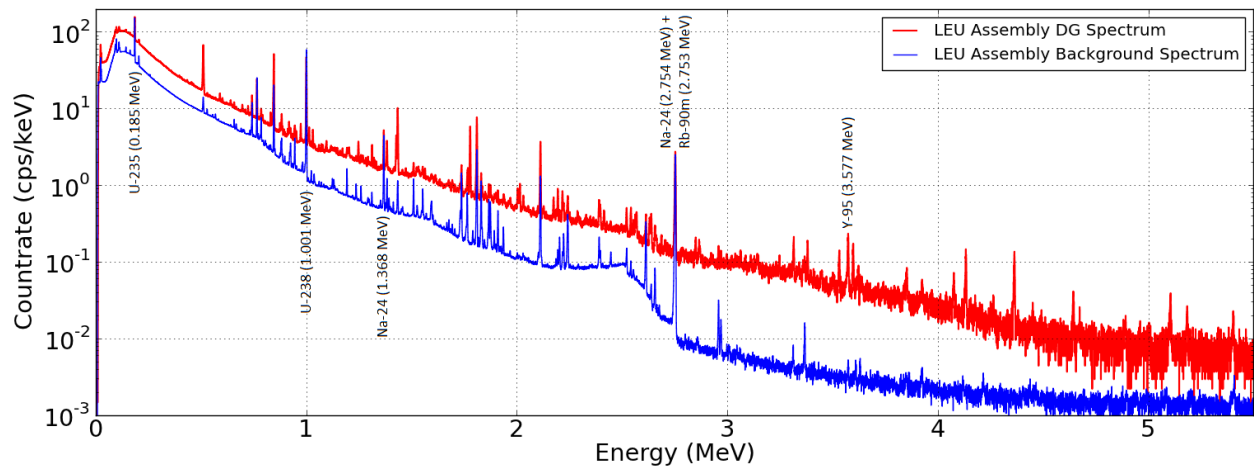
Figure 32a. Measured DG spectrum for assembly of LEU pins (red) in water. The blue spectrum was taken after several hours of delayed gamma measurements and shows the background from fission products with longer half-lives.
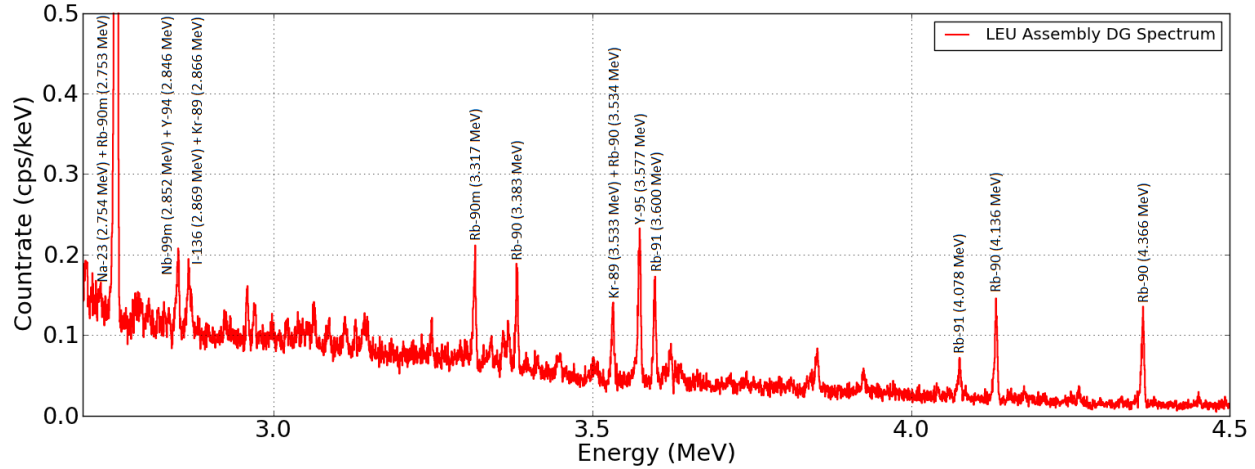
Figure 32b. Measured LEU spectrum (same as in 22 a) for the energy range from 2.7 to 4.5 MeV.
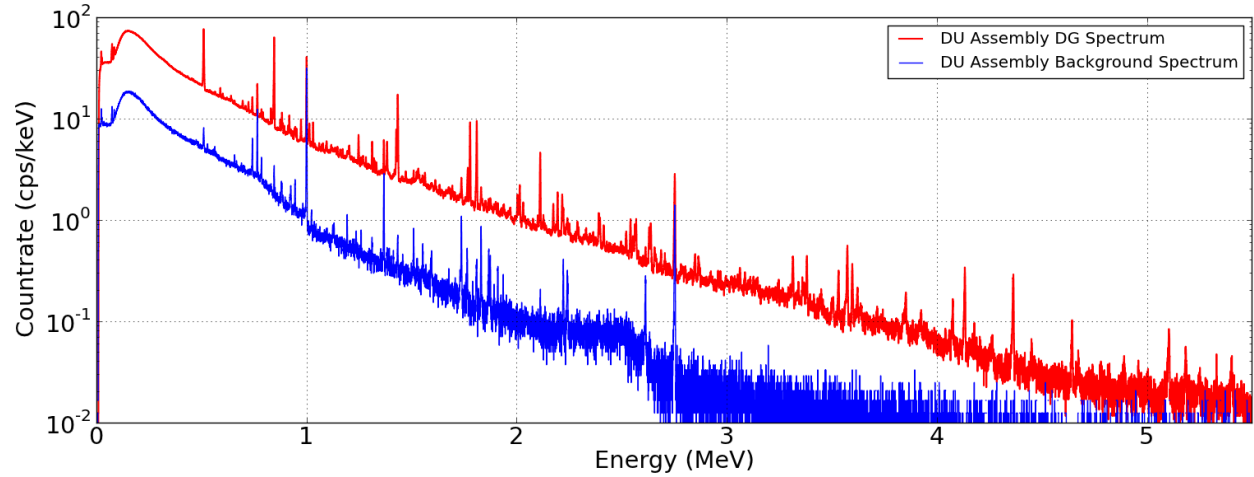
Figure 32c. Measured DG spectrum for assembly of DU pins (red) and background (blue).

III. Modeling

Modeling was performed in support of the experimental measurement campaigns of task 1, i.e., for designing the experiments and analyzing measured data. Modeling technique and code package were benchmarked against the experimental results. In addition the modeling of potential applications was started and spent fuel measurement scenarios analyzed building on earlier work performed as part of the Next Generation Safeguards Initiative effort [10] aimed at determining Pu content in spent nuclear fuel assemblies.

III.1 Modeling Code Development and Benchmarking

The modeling approach is based on a hybrid calculation method in which Monte Carlo and analytical components are executed in sequence as indicated in Figure 33. The primary advantage of this scheme is effective processing of extensive amounts of data under full user control. The

Monte Carlo transport module enables modeling of complex geometries and provides effective variance reduction solutions that enhance the computational performance in massive parallelized calculations. The analytical CINDER-DGSDEF (Discrete Gamma Source DEFinition code) calculation module provides fast and exact calculations of material inventory evolutions and delayed gamma-ray source terms. In the first step, the interrogating neutron flux distribution is calculated. This is followed by the calculation of delayed gamma-ray and passive emission spectra. In the last step, the radiation is transported to the detector and the detector response determined. The modeling calculations include neutron induced and spontaneous fission, neutron capture transmutations, and passive gamma-ray emissions. The modeling capability was benchmarked for "one pass" and "pulsed" measurements.

TRANSPORT CODE (*MCNPX 2.7*) → TRANSMUTATION AND DISCRETE SOURCE RECONSTRUCTION CODE (*Analytical, CINDER method merged with DGSDEF*) → TRANSPORT CODE (*MCNPX 2.7*)

Figure 33. Delayed gamma-ray measurement modeling approach.

The modeling method was used in conjunction with the experimental campaign to investigate and optimize the measurement parameters and to interpret the resulting delayed gamma-ray spectra. In the same process, experimental data was used for benchmarking of the modeling technique and associated physics library data (neutron cross sections, fission yields, fission products decay data, gamma-ray emission intensities and branching ratios). Comprehensive fission products creation and decay patterns are developed in the code using an extensive dataset of 3400 nuclides with Z ranging from 1 to 103 in ground and isomeric states; 98 nuclides with spontaneous and neutron-induced fission yields (at thermal, fast, and high energy regions) for 1325 fission products. Neutron reaction cross sections are defined in 64-group energy structure [11]. The full extent of this physical data is used in the course of modeling calculations without any omissions or restrictions.

A significant part of the code development and benchmarking effort specifically focused on the newly developed capability that allows modeling of the "pulsed" interrogation regime. In the pulsed measurement mode, acquisition of the delayed gamma-ray spectra is performed between active cycles of the interrogation source. Each neutron source pulse perturbs isotopic inventory of activated targets, which is reflected in time-dependent evolution of the delayed gamma-ray responses. For example, short pulse measurement regime (with a period up to few dozens of seconds) highlights response from short-lived fission products and builds up statistical quality of measured spectra. However, when such short pulsing is extended in time, peaks from long-lived fission products eventually dominate the response. In order to capture this time behavior of "pulsed" interrogation systems, the modeling code was set up to explicitly calculate a discrete delayed gamma-ray emission source term for each subsequent detection period. The cumulative source term that is passed to the transport code for a detector response calculation is obtained as a superposition of the entire set of individual between-the-pulse emissions. The isotopic inventory of an activated target is maintained continuously through the entire length of "pulsed" interrogation and the entire material composition is passed from the end of the detection period to the start of the next activation cycle. This explicit implementation of the delayed gamma-ray response calculation is complex and highly demanding to memory and processor power.

46

Benchmarking of the delayed gamma-ray modeling capability was accomplished primarily using experimental data from the ISU setup described in section II of this report. Initial calculations were performed to replicate the delayed gamma-ray responses acquired in the "one-pass" regime, which typically consisted of 15 minutes of activation and 30 minutes of acquisition time periods with a one minute cool-down/sample transfer gap between them. This assay scenario considered two separate setups, the first one was used for sample irradiation with the linac-driven neutron source, and the second one, located in a separate room, was used to acquire the delayed gamma-ray spectra. "Pulsed" benchmarking calculations were completed for the measurement setup configuration in which the linac-driven neutron source and a high-resolution HPGe detector were co-located. This setup was interpreted and parametrized in the modeling code is depicted in Figure 34.
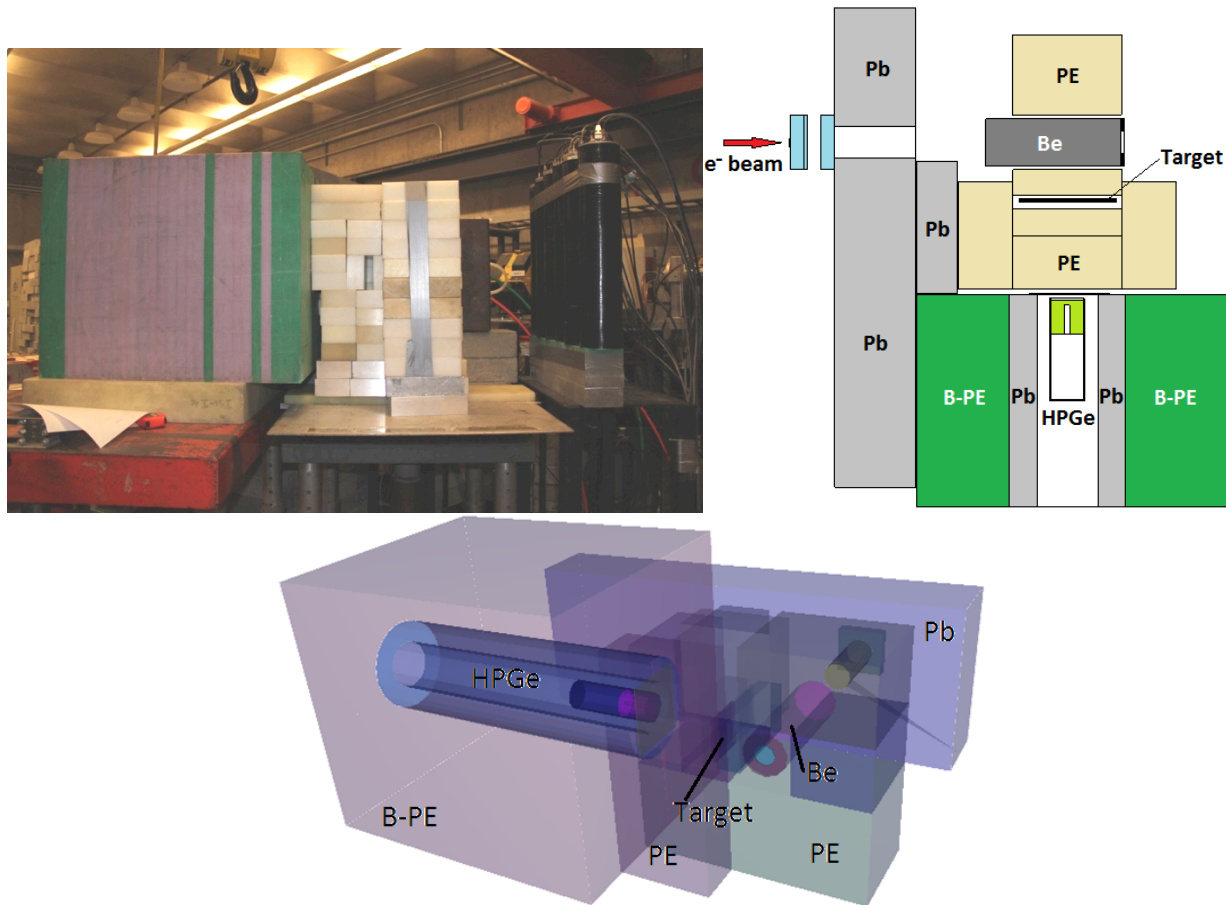
Figure 34. "Pulsed" measurement setup at IAC with the co-located neutron source and HPGe detector used for benchmarking measurements of short-lived DG responses at IAC: photography of the setup from the side opposite to the linac beam (top left); top view of the setup (top right); 3D rendering of the setup (bottom).

In the IAC experimental setup, the linac-driven neutron source is produced by intercepting the electron beam with a thick (4.2 g/cm^2) tungsten radiator resulting in the emission of photons with bremsstrahlung energy and angular distribution. After passing through the aluminum electron filter, the bremsstrahlung photons are collimated on a beryllium photo-neutron converter in which neutrons are produced by means of (gamma,n) reactions on Be-9 isotopes with a threshold energy of approximately 1.7 MeV. The resulting neutron flux is thermalized in the layers of polyethylene

surrounding the Be converter before reaching the assay sample. By varying elements of this setup (electron beam energy, accelerator current and frequency, photo-neutron converter material, amount of polyethylene moderator), a wide range of energy, intensity and time distribution characteristics of the neutron source can be produced. According to the modeling calculations, the intensity of the ISU linac-driven neutron source can vary from 10^8 to over 10^{12} neutrons per second. However, for the pulsed measurements with the co-located HPGe detector, the neutron output intensity was limited to the lower range of 10^8 to 10^9 n/s in order to limit the neutron damage and charge deposited by the bremsstrahlung source to the detector crystal during the active linac cycles.

Development of the IAC experimental setup and benchmarking of the delayed gamma-ray response modeling approach required a detailed simulation of the linac-drive neutron source parameters. From preliminary calculations and experimental sessions, the optimal accelerator electron beam energy for measurements in the pulsed regime was determined at 15 MeV. The angular and energy distribution of the bremsstrahlung photon source was obtained by using MCNPX transport calculations and is shown in Figure 35. Previously, similar bremsstrahlung source calculation methodology was verified for consistency with the theoretical expectations (Schiff formula, NCRP recommendations [12]), and was confirmed in the IAC activation experiments with a high-energy photon source. Transport calculations demonstrate that under the conditions of the baseline configurations of the IAC experimental setup, the overall conversion rate of electrons in the linac beam to bremsstrahlung photons was approximately 0.780±0.002. Conversion values calculated this way were used for absolute normalization of modeled results relative to the linac beam parameters during the experiment.
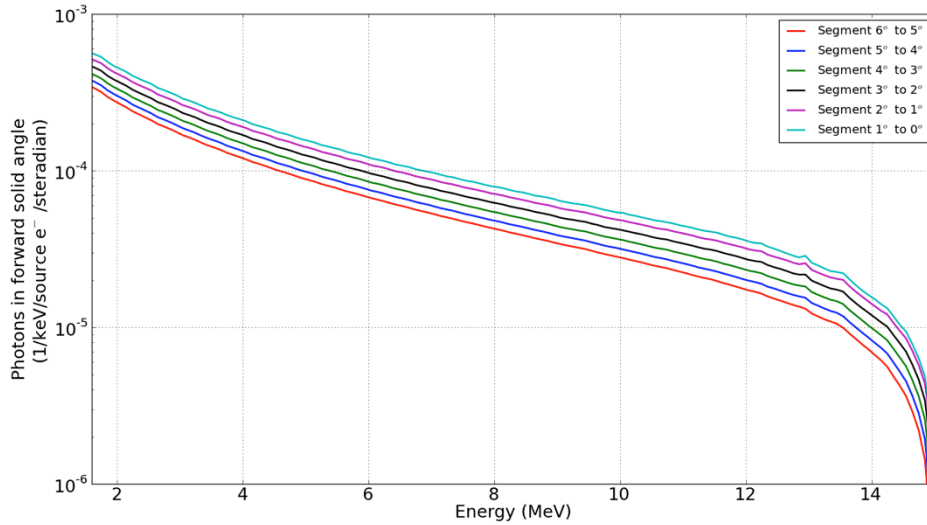
Figure 35. Calculated bremsstrahlung photon source energy and angular (forward segments) distribution for the IAC experimental setup, assuming 15 MeV linac electron beam energy.

Resulting neutron flux on the target and its energy distribution in the IAC setup was performed for each activation experiment using the MCNP transport code and a parameterized definition for the bremsstrahlung source. Several configurations of the setup were investigated in order to achieve either primarily thermal, or primarily fast neutron activation flux in the targets. The main variables in the process of the experimental setup optimization were the linac electron beam energy, photo-neutron converter material, target standoff, amount of moderator (polyethylene), and the presence of thermal neutron filters (Cd). Typical neutron flux-on-target distributions calculated for the "thermal" and "fast" setup configurations are shown in Figure 36. Such distributions obtained for the 64-group energy structure were calculated for each experiment and are direct outputs of the

delayed gamma-ray modeling code. Neutron flux distributions were experimentally verified by activating gold witness foils in the ISU interrogation setup. This was performed by introducing gold samples with known mass together with the activated target in each experimental measurement. After the irradiation period, the amount of thermal neutron flux incident on the foil was estimated from the area of the 411 keV peak from the Au-198 isotope decay. Predictive calculations of the gold foil activation were performed using delayed gamma-ray modeling algorithm, with a satisfactory agreement between measured and calculated results.
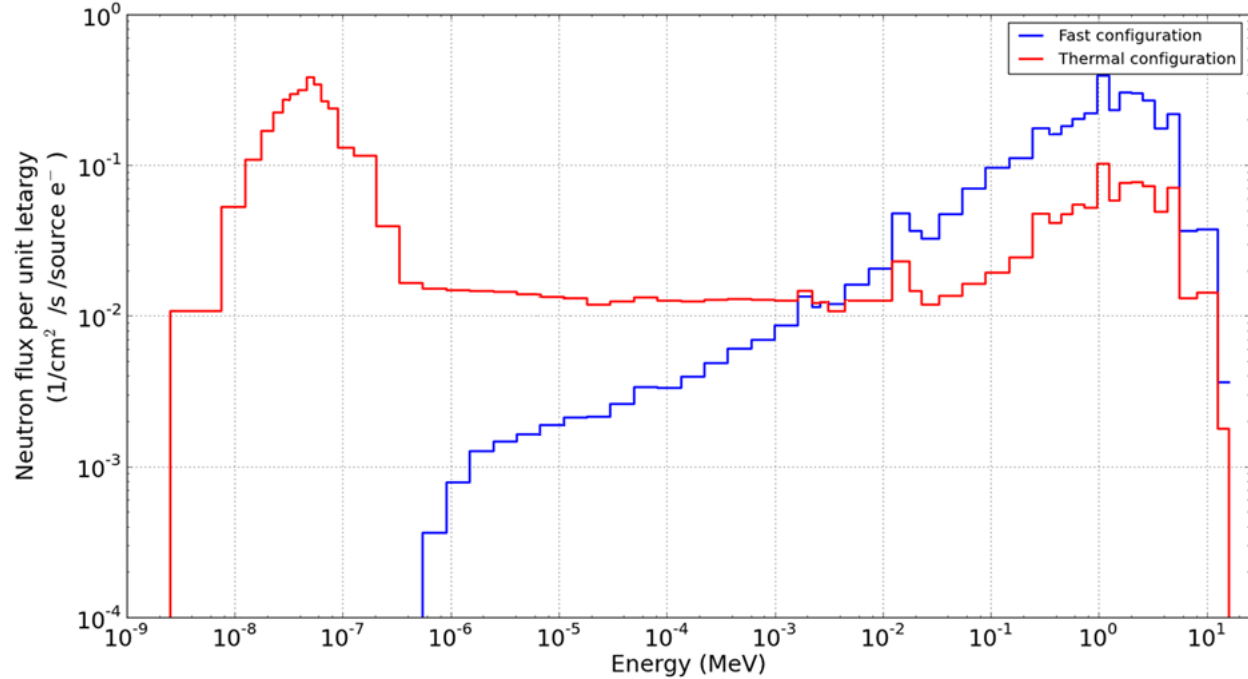
Figure 36. Calculated neutron flux-on-target energy distributions in "thermal" and "fast" configurations of the IAC experimental setup.

Experimental data from ISU measurements was used to benchmark the modeling technique and associated data libraries with the emphasis on verification of the complex pulsed modeling capability. Each measured delayed gamma-ray spectrum was matched with a simulated spectrum; any discrepancies were documented and analyzed. The discrete gamma-ray source terms from the second stage of the modeling process were used to identify the emission lines contributing to the most prominent peaks in the experimental spectra. An example of the combined measured and calculated results analysis is shown in Figure 37, with more details provided in Figures 38 (a-e). This set of results was obtained for a depleted uranium target irradiated in a pulsed regime with 10 seconds activation, 0.16 seconds detector relaxation, and 10 seconds spectrum acquisition time periods. This 20 second measurement period was repeated in 677 cycles for a total measurement time of 3.7 hours. Measured and calculated spectra in Figures 37 and 38 are shown as obtained, without any artificial normalization and offset. Overall, a good agreement is observed between all comparisons of experimental and modeled results. The modeling technique provides a satisfactory match of the continuum in the high-energy region, and accurately predicts the location and relative intensities of the most prominent peaks. In certain cases, isolated peaks are present in the calculated spectra while absent in the measured spectra and vice versa. Such discrepancies indicate potential deficiencies in the fission yields data libraries and require separate investigation.

Qualitative comparison of measured and calculated delayed gamma-ray spectra indicate a good agreement in high-energy range above approximately 2.7 MeV. Below this threshold, measured

spectra are dominated by several strong peaks that are not replicated in the calculated results. This also affects the comparison of measured vs. calculated continuum. This discrepancy can be explained by the neutron activation of the experimental setup elements that was not considered in the modeling calculations. In particular, some of the lines were identified as Na-24 emissions with a half-life of 14.95 hours that is produced either by the ^{27}Al(n,alpha)^{24}Na reaction in aluminum housing of the HPGe detector, or by the ^{23}Na(n,gamma)^{24}Na reaction on the naturally occurring sodium. The other lines were attributed to the ^{116m}In emissions with 54.3 minutes half-life produced from the ^{115}In present in the HPGe detector construction.
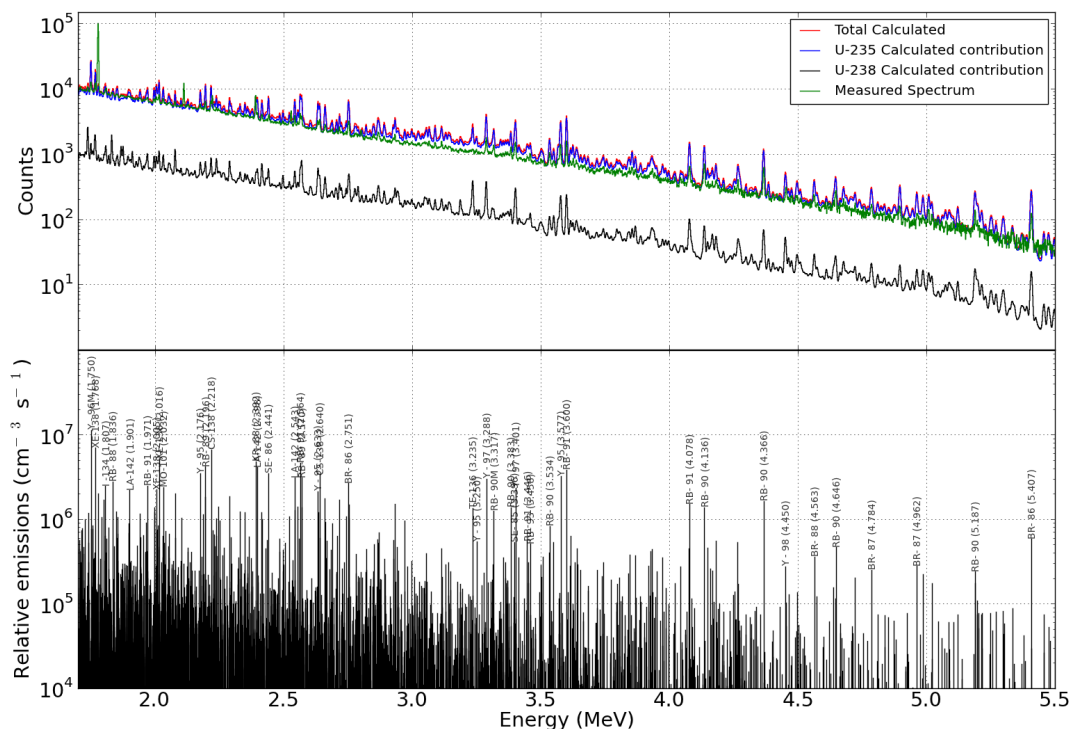
Figure 37. Example of the calculated and measured spectra comparison for the depleted uranium target in "thermal" configuration and the pulsed 10 seconds activation, 9.84 seconds acquisition time regime.

Figure 38 (a). Close-up of the 1.7 to 2.7 MeV region of Figure 13.

Figure 38 (b). Close-up of the 2.7 to 3.5 MeV region of Figure 13.
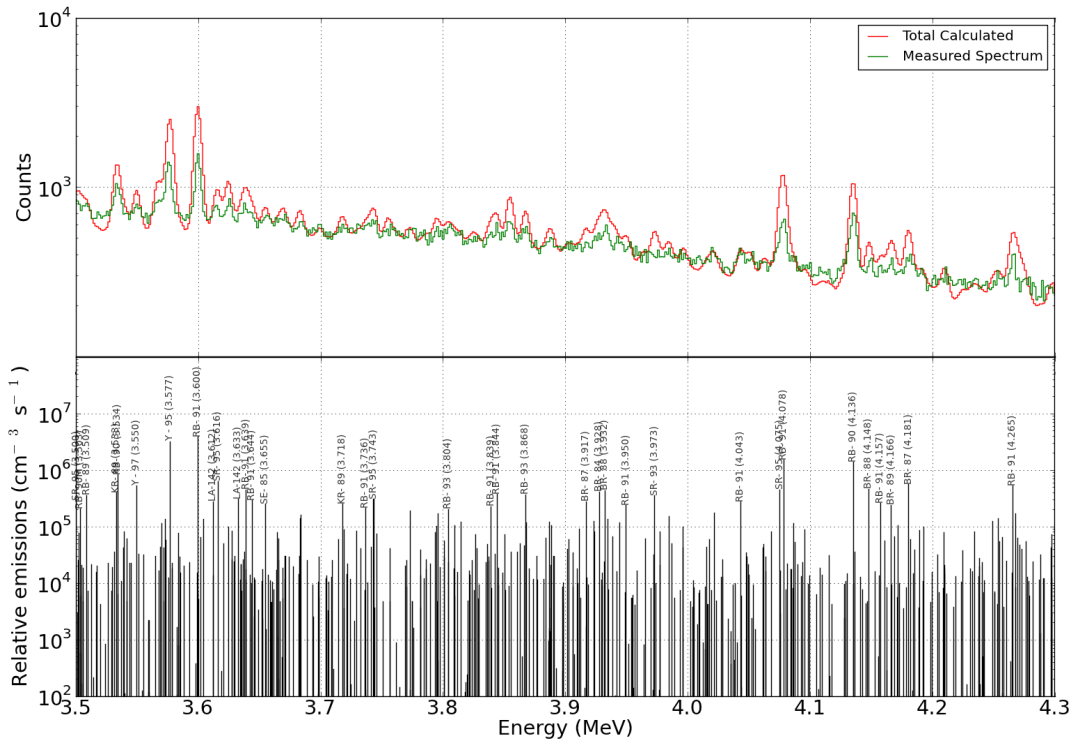
Figure 38 (c). Close-up of the 3.5 to 4.3 MeV region of Figure 13.
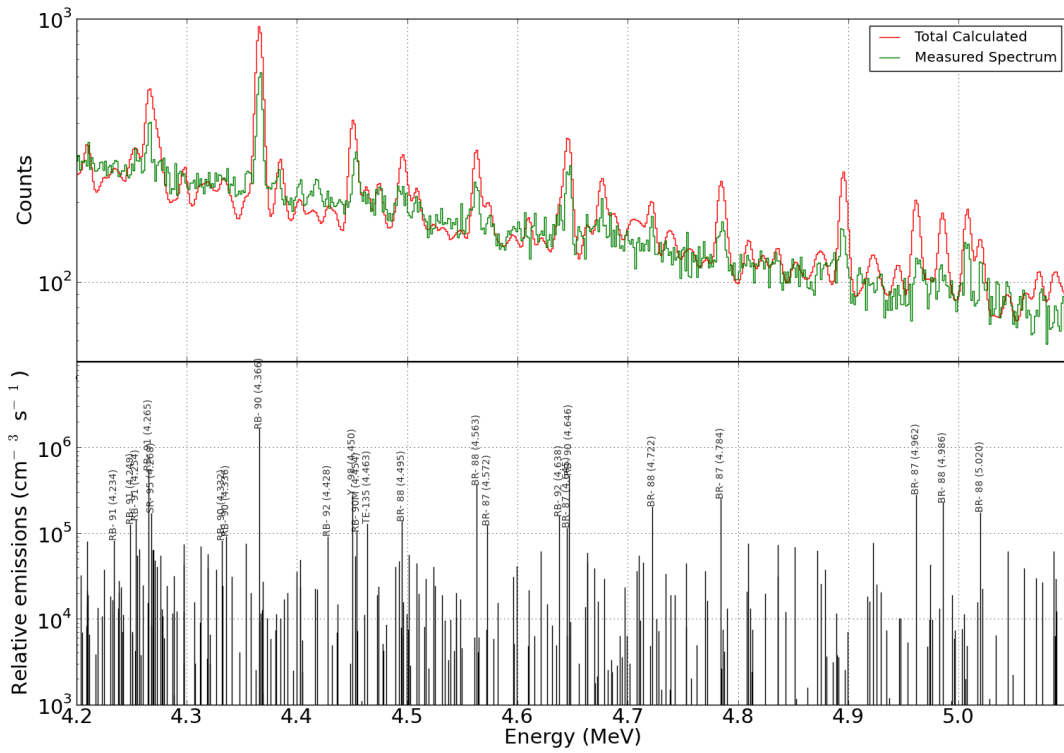
Figure 38 (d). Close-up of the 4.3 to 5.1 MeV region of Figure 13.
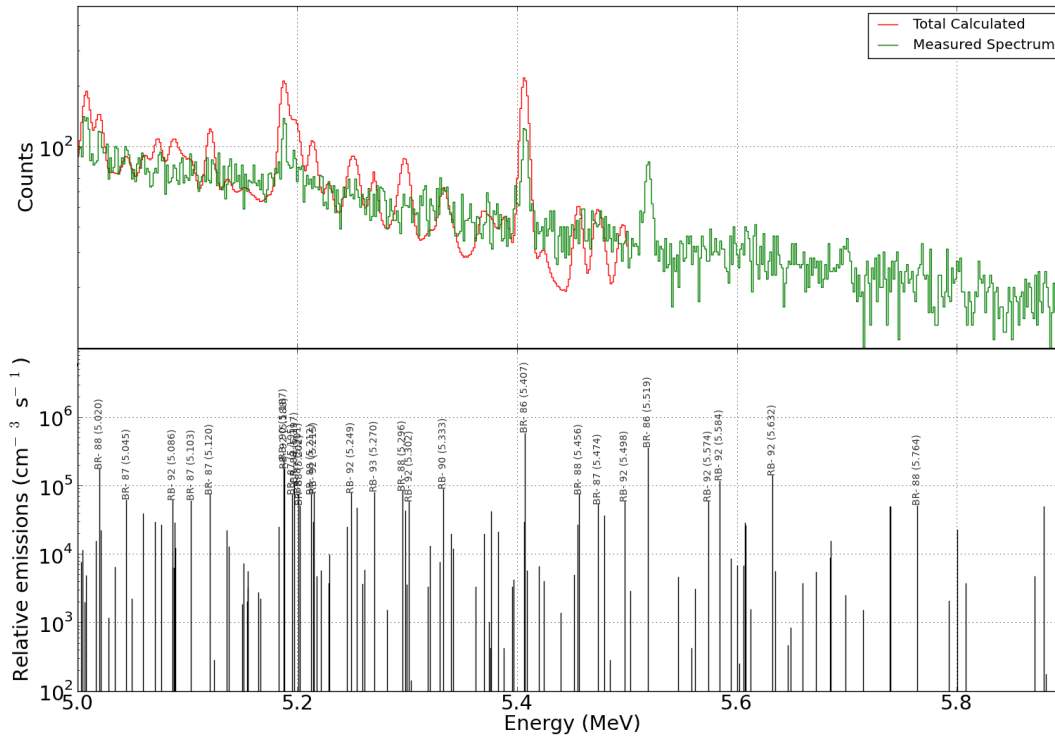
Figure 38 (e). Close-up of the 5.0 to 5.9 MeV region of Figure 13.

Measured and calculated delayed gamma-ray spectra were produced for the individual samples of fissile materials as well as for various combinations. This data was used to verify the performance of the modeling technique for the case of complex heterogeneous targets. In addition, these results were used to develop the response analysis approaches, in particular the methodology for determining the relative contribution of fissile isotopes present in the activated sample to the detected response spectrum. Preliminary findings indicate that the response de-convolution techniques will be limited by the statistical quality of the delayed gamma-ray spectra, and the final uncertainty in the peak areas obtained by fitting. A set of results with high statistical quality was achieved by repeating the one-pass measurements of the same target several times. An example of these "high-quality" results is shown in Figures 39 – 41 for the individual Pu and depleted uranium targets, as well as their combinations. A good qualitative agreement between the calculated and measured results is observed in all cases, with overall discrepancies attributed mainly to the detector response model adopted for the calculations.
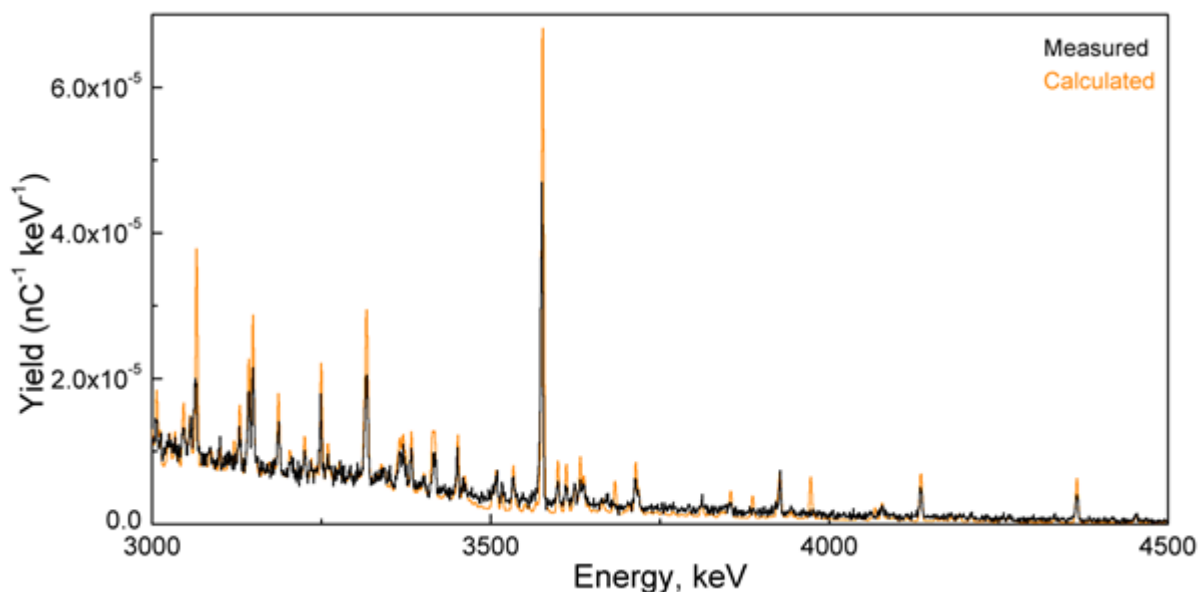
Figure 39. Comparison of a detailed measured delayed gamma-ray response from the Pu-239 target and corresponding calculated spectrum. Parameters: 15 minutes activation, 30 seconds transfer, 30 minutes spectrum acquisition, repeated 5 times.
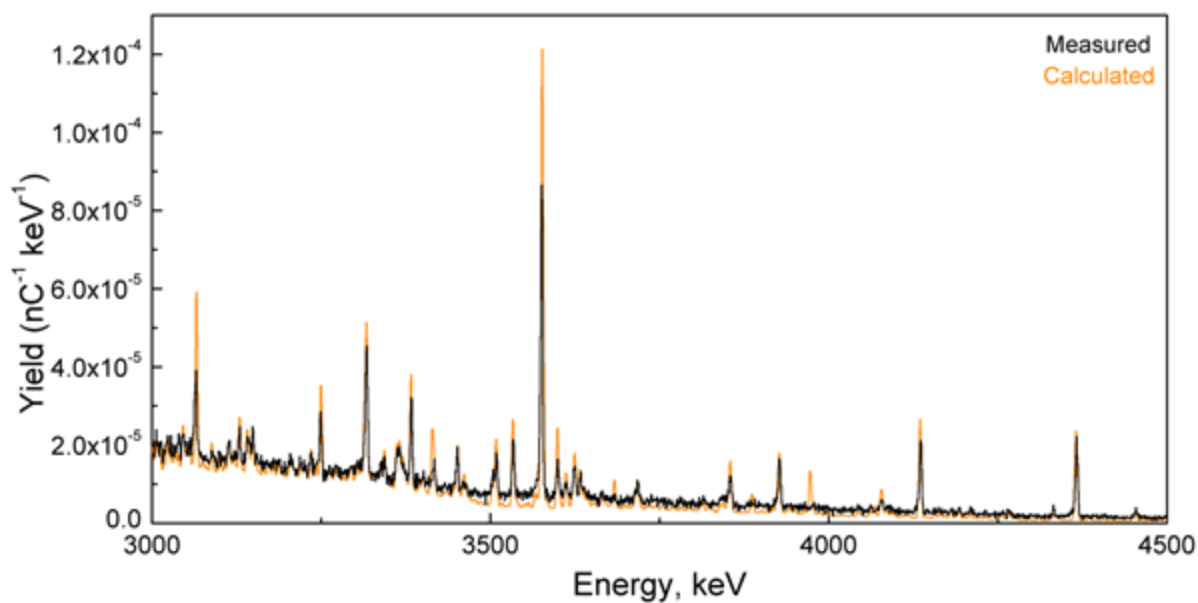
Figure 40. Comparison of a detailed measured delayed gamma-ray response from the DU target and corresponding calculated spectrum. Parameters: 15 minutes activation, 30 seconds transfer, 30 minutes spectrum acquisition, repeated 5 times.
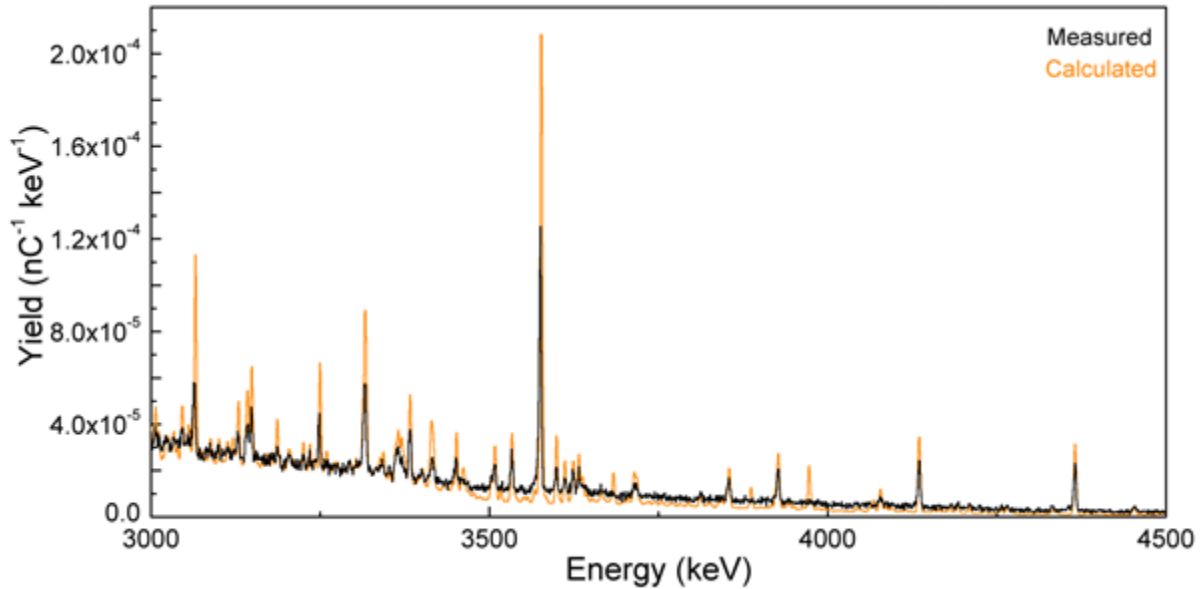
Figure 41. Comparison of a detailed measured delayed gamma-ray response from the combined DU+Pu-239 target and corresponding calculated spectrum. Parameters: 15 minutes activation, 30 seconds transfer, 30 minutes spectrum acquisition, repeated 5 times.

Figure 42 illustrates a subset of calculations completed for various targets irradiated in the "pulsed" regime. Measured and calculated spectra are compared for HEU, Pu-239, and HEU+Pu-239 combined targets. The experimental spectra are overall well reproduced with delayed gamma-ray peak positions and relative intensities matched by the modeling result. However, modeled peaks are significantly more pronounced and a number well-defined peaks in the calculated spectra barely visible in the measured spectra. This effect was investigated earlier in the project and is attributed to the fact that the detector response calculation does not include major pulse processing electronics effects, such as incomplete charge collection, noise, pulse-shape discrimination, and pile-up rejection. Such effects become especially important and hard to replicate at high and dynamically changing count rates, which are an unavoidable attribute of the delayed gamma-ray activation measurements.
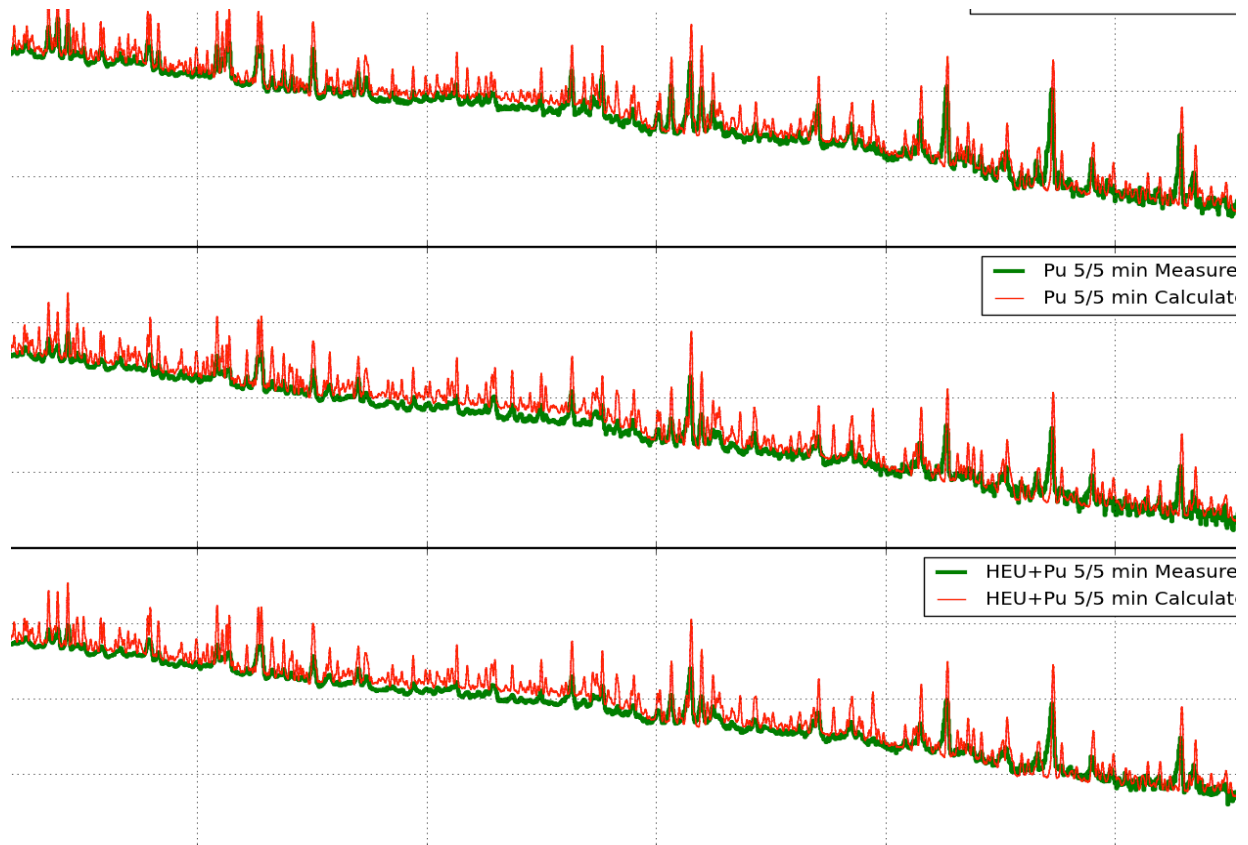
Figure 42. Comparison of measured and calculated delayed gamma-ray spectra for benchmarking the code in the "pulsed" regime.

Benchmarking comparisons suggest that the modeling technique is capable of accurate (within the limits of the physical data libraries) simulation of the transport processes, activation and temporal evolution of material inventories and associated gamma-ray emission source terms. The accuracy of calculations is sufficient for application modeling, general prediction of real systems behavior, and parametric studies. However, it is not designed to fully replicate the detector effects and performance limits of the signal processing electronics. Therefore, an exact match between the measured and calculated spectra should not be expected, making the benchmarking conclusion less obvious. In addition, uncertainties in the composition of the sample materials and package, exact target position in the irradiation setup, limited statistical quality of the pulsed experimental spectra and other factors limit the effectiveness of the direct spectra comparison.

In the effort to inform a more formal benchmarking of the modeling technique through a numerical comparison of measured and calculated results, three evaluation criterial were adopted:

1. Visual comparison by overlaying predicted and measured spectra to determine the correct overall count rate, peak positions, energy and resolution calibrations, peak shapes and statistical quality of the experimental data. At this step peaks omitted in one spectrum and present in another are identified and recorded.

2. Direct ratio of corresponding peak area fits in calculated and measured spectra are verified to be constant (within uncertainty) over the high energy range 3.0 to 5 MeV. A constant offset from unity is routinely observed and attributed to the statistical limits of the experimental data, and assumptions of the model.

3. Shape analysis of the spectral sub-regions using a correlation function method. In this approach, a qualitative comparison of the measured and calculated spectra is performed and a formal metric indicating the relative match between the shapes is obtained.

The shape analysis benchmarking approach is demonstrated here for a set of experimental and modeling results obtained in one-pass and pulsed interrogation time regimes. Figure 43 compares the high-energy regions of response spectra acquired from the same HEU target in three distinct measurement patterns: 15 minutes activation, 30 minutes detection (one pass); 10 seconds activation, 10 second detection (pulsed); 60 seconds activation, 60 seconds detection (pulsed).
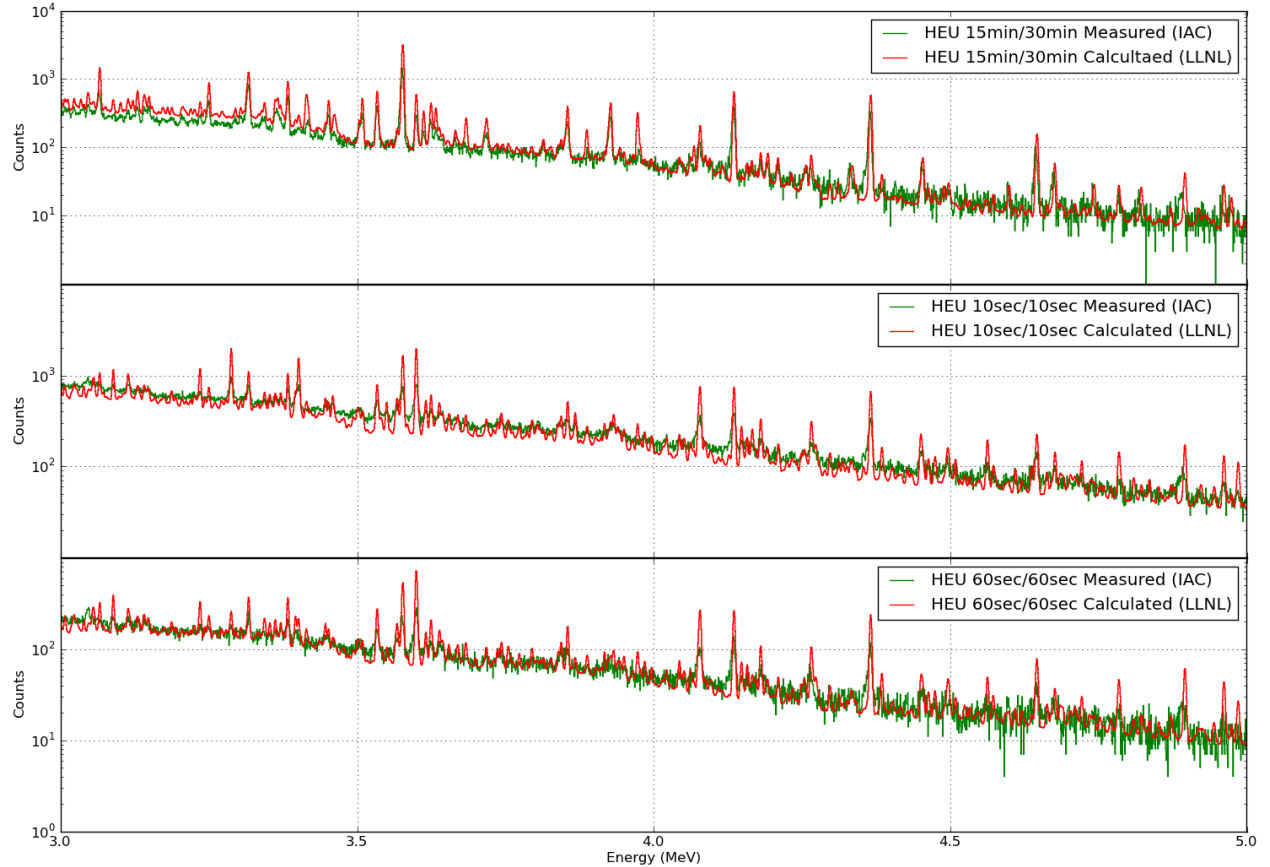
Figure 43. Comparison of calculated and measured HEU spectra for various assay time regimes: one-pass 15 min irradiation – 30 min detection (top), pulsed 10 sec irradiation – 10 sec detection (middle), pulsed 60 sec irradiation – 60 sec detection (bottom).

Experimental and simulated gamma-ray spectra were compared using a correlation function method. A correlation value Ck is calculated to quantify the degree of overlap between the experimental and simulated spectra in spectral sub-ranges [13]:

$$C_k = \frac{\sum_i^k E_i S_i}{\sqrt{\sum_i^k E_i^2 \sum_i^k S_i^2}},$$

57

where k denotes an arbitrary energy sub-range in the spectra, E_i and S_i are the number of counts in the ith channel of the experimental and simulated spectra in that sub-range, respectively. The correlation value would be 1 in the case of perfect overlap of the two spectra and 0 in the case of no overlap. This value is sensitive only to the shape and not absolute normalization; therefore this technique is not sensitive to any offset between the two spectra.

To implement this comparison method, the delayed gamma-ray region shown in Figure 43 was split in ten 200 keV-wide sub-ranges between 3.0 and 5.0 MeV. The correlation value is calculated for each sub-range assuming all possible combinations of measured and calculated spectra, meaning that the one-pass results are not only compared to each-other but also to the two sets of pulsed data and vice versa. The resulting correlations between each of the three experimental and all calculated spectra in each sub-range are shown in Figures 44 – 46. In each of these figures a certain experimental spectrum from the HEU target is compared with all three calculated spectra for the same sample. Figure 44 compares experimental spectrum obtained in the one pass 15 minutes activation, 30 minutes detection time regime with the corresponding calculated spectrum and two somewhat different spectra calculated for pulsed mode with 10 seconds activation, 10 seconds detection, and 60 seconds activation, 60 seconds detection. In the center of Figure 44, the 3D plot displays the correlation value for 10 sub-ranges of the matching and non-matching spectra pairs. In the case of matching measured and calculated spectra the correlation function ranges between 0.90 and 0.98 across all sub-range regions. This represents a good overall agreement between simulation and experiments, which was found to be typical for all matching cases. Conversely, there is substantial disagreement in some of the sub-ranges of the non-matching comparison cases, although some sub-ranges exhibit a good correlation for all three cases. The latter is explained by the fact that all three spectra exhibit the similar features arising from the longer-lived delayed gamma-ray components of the response.

The mean of the correlation values for all sub-regions in the three comparison sets from Figures 44 – 46 is shown in Table V. In general, the matching measured and calculated cases are characterized by the higher mean correlation value and a lower standard deviation as a measure of its spread in the distribution. The non-matching cases have a lower mean correlation and a greater spread, both indicating a poorer match. The one-pass measured spectrum is in a good agreement with the one-pass calculations and deviate considerably from the pulsed spectra calculations. The two measured pulsed spectra are in a good agreement with both calculated pulsed results, which was observed in the visual comparison, and disagree with the one-pass calculation results. The formal shape comparison results support the initial conclusion on the satisfactory overall performance of the modeling technique in all investigated interrogation time patterns.

Table V. Summary of the mean correlation values from the cross-comparison of measured and calculated spectra obtained from the HEU target.

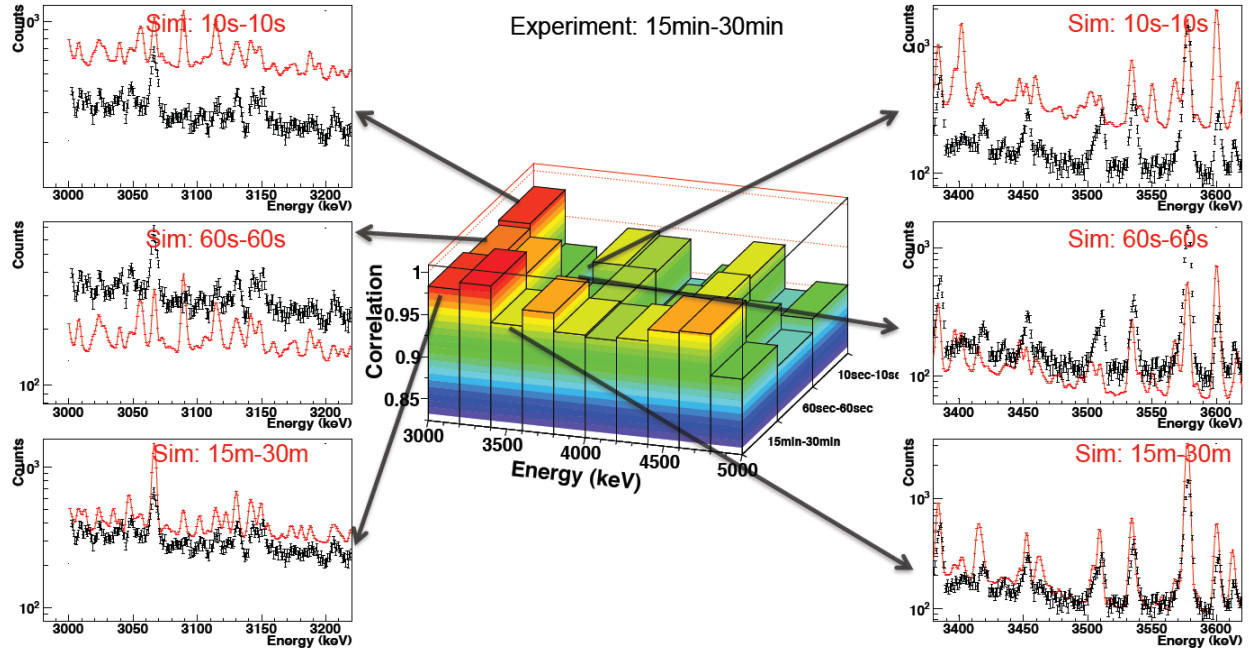| Measured spectra	Calculated spectra		
	One-pass 15 min – 30 min	Pulsed 10 sec – 10 sec	Pulsed 60 sec – 60 sec
One-pass 15 min – 30 min	0.956 ± 0.021	0.916 ± 0.038	0.923 ± 0.036
Pulsed 10 sec – 10 sec	0.839 ± 0.107	0.956 ± 0.019	0.939 ± 0.033
Pulsed 60 sec – 60 sec	0.847 ± 0.094	0.948 ± 0.021	0.950 ± 0.030

Figure 44. Correlation function analysis for the HEU target experimental spectrum obtained in one-pass 15 minutes activation, 30 minutes detection time regime with three calculated spectra.
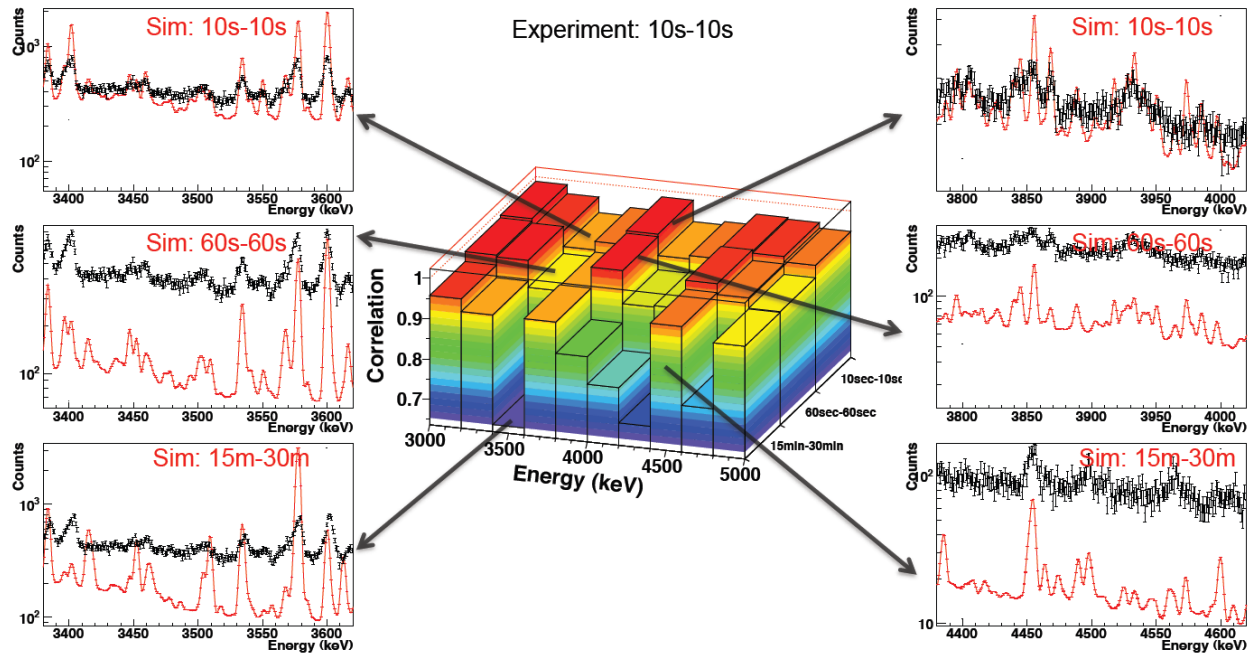
Figure 45. Correlation function analysis for the HEU target experimental spectrum obtained in pulsed 10 seconds activation, 10 seconds detection time regime with three calculated spectra.
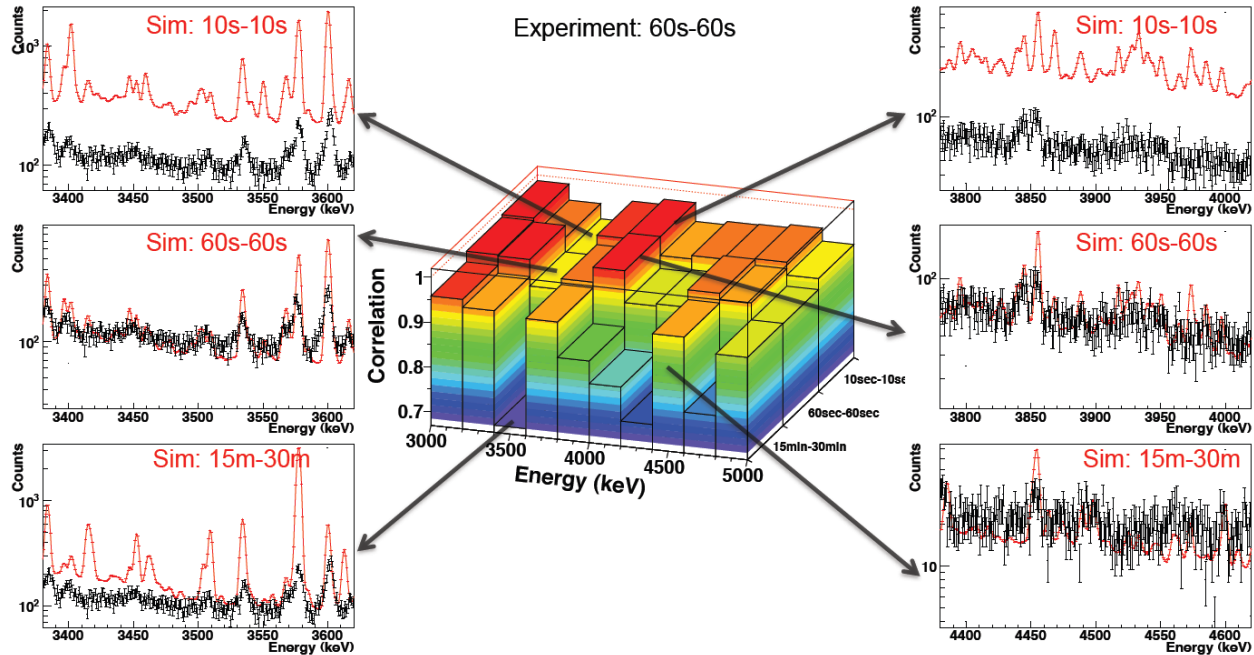
Figure 46. Correlation function analysis for the HEU target experimental spectrum obtained in pulsed 60 seconds activation, 60 seconds detection time regime with three calculated spectra.

Overall, the modeled response spectra proved to be useful for interpretation of measured spectra for identification of signature peaks and fissionable isotopes sensitivity. The modeling capability was successfully used to develop the response analysis approaches, in particular the methodology for determining the relative contribution of fissile isotopes present in activated samples. Candidate analysis methods were investigated for both the experimental and calculated results, and were used for application modeling. Preliminary findings indicate that the response de-convolution techniques will be limited primarily by the statistical quality of the delayed gamma-ray spectra, and the final uncertainty of the peak area fitting.

III.2 Applications Modeling

The modeling capability was applied to the investigation of spent nuclear fuel assay building on results of the Next Generation Safeguards Initiative (NGSI) study. Investigation of the delayed gamma-ray assay responses was performed for a number of Westinghouse 17x17 PWR spent nuclear fuel assembly models defined in the NGSI spent fuel libraries (SFL) produced and maintained by the Los Alamos National Laboratory. [14] Each SFL investigated specific spent nuclear fuel properties, and assumed a different set of parameters for the burnup/depletion calculations. The resulting spent fuel models vary in the level of geometric detail, reactor operation parameters, symmetry, and reflection assumptions. Within each library, assemblies varied with a range of initial U-235 enrichment (IE), integral burnup (BU), and cooling times after discharge from a reactor (CT). For the DG response calculations, the following sets of assemblies from three SFLs were considered:

- SFL#2: 33 assemblies with BUs of 15, 30, 45, and 60 GWd/MTU, IEs of 2, 3, 4, and 5 wt%, and CTs of 5, 20, and 40 years.

- SFL#3: 46 assemblies with BUs of 15, 30, and 45 GWd/MTU, IE of 4% and CTs of 5, 20, and 80 years, obtained for various reactor operation conditions such as moderator density and presence of burnable neutron absorbers. (Produced in collaboration between the Oak Ridge National Laboratory (ORNL) and LANL.)

- SFL#4: 36 assemblies with non-disclosed parameters produced for sensitivity studies and blind tests.

Investigation of the delayed gamma-ray assay feasibility of spent fuel assemblies defined in these libraries were performed using exactly the same modeling methodology that was benchmarked in the course of the experimental campaign at ISU.

III.2.1 Modeled Setup Configuration and Parameters

For high-fidelity reconstruction of the delayed gamma-ray spectroscopic responses from SFL assemblies, detailed material definitions were supplied for each assembly in the form of intermediate binary CINDER90 composition files. Each file contains on the order of two thousand isotopes generated in the burnup/depletion calculation for every individual fuel pin. Material compositions were provided at discharge from the reactor (at CT=0). This data was processed using the DGSDEF code and pin material inventories were "aged" to specific CTs with explicit analytical tracking of all time-dependent evolutions of the isotopic content. From the detailed material definitions at each CT, a discrete gamma-ray emission source term was produced for each individual pin in the assembly. These source terms were used for calculating passive gamma-ray spectra in the simulated assay setup. In order to obtain the response spectra, the MCNP model of the assembly with simplified material inventories defined for specific CTs was used to complete neutron transport calculations in the active interrogation setup with a DT neutron generator. The computed multi-group neutron flux distribution across the assembly pins was used for analytical calculation of delayed gamma-ray source terms and spectroscopic responses. This modeling approach accounted for realistic assay parameters including the full 3D geometry, attenuation and collimator effects, scatter in the fuel and detector material, detector resolution and stopping power as a function of energy. Resulting simulated spectra are expected to replicate features of spectra obtainable in real measurements (with a caveat of the unaccounted for detector electronics effects) and are compatible for direct processing with spectroscopy analysis software. Predicted spectra were treated as if they were real datasets obtained from the experiment, and standard spectra processing methods were utilized. No a priori information about the assembly parameters or additional data from the model was used in the response de-convolution. Realistic statistical uncertainties were reproduced in the calculated responses and propagated through each step of the analysis to the final result for each assembly.

The complexity of the delayed gamma-ray assay is determined by the requirement to acquire high-resolution delayed gamma-ray responses in the presence of the high-intensity passive gamma-ray background of the spent fuel assembly. High-resolution spectroscopic measurements are required to resolve the interference between the passive and actively induced gamma-ray signals. The passive gamma-ray response in spent fuel primarily originates from the long-lived fission products accumulated during the reactor life, and is primarily confined to the lower energy range: under ~3 MeV at shorter cooling times (5 years), and under ~2 MeV at long cooling times (10 years and longer). The delayed gamma-ray signature extends into the higher energy range and is dominated by the short-lived fission products produced as a result of interrogation with a neutron source. The upper energy range of the response spectrum is limited primarily by the intrinsic efficiency of the detector, and for HPGe-type spectrometers the practical range extends up to ~5

MeV. For the modeling effort with SFLs, the delayed gamma-ray response spectra were considered for the same region between 3 and 5 MeV, acceptable for assemblies with any cooling time.

The effective spent fuel assay setup must have minimal efficiency to the gamma-rays in the lower range of the spectrum below ~3 MeV, and provide sufficient efficiency in the higher energy range where the delayed gamma-ray responses can be collected without any interference. Two primary design parameters must be in balance to achieve this condition: 1) intensity of the interrogating neutron source, and 2) count rate limit of the detector(s). Increasing the neutron generator output proportionally increases the intensity of the delayed gamma-ray response relative to the passive background signal; therefore the highest practically achievable neutron source intensity is desirable. Detector count rate imposes the limit on the minimal amount of attenuation and collimation required to mitigate the high-intensity passive gamma rays. Attenuating filters between the detector and the assembly effectively reduce the low-energy gamma-ray rate, but also affect the high-energy part of the gamma-ray spectrum, therefore suggesting the existence of an optimal thickness. Collimation controls the overall gamma-ray intensity reaching the detector, and can partially balance the delayed gamma-ray losses due to the attenuation filters.

For the purposes of modeling the delayed gamma-ray spectra from the SFL assemblies, the assumed neutron generator intensity was set to 10^{11} n/s, as the maximum achievable in modern commercial prototypes. The target limit on the detector count rate was set at approximately 100 kHz, which was practically demonstrated with the current high-resolution HPGe spectroscopy electronics capable of resolving the pile-up effects and dead time signal losses at high throughput. These limiting parameters are not the final requirements DG assay and can be further investigated when more realistic implementations of the neutron source or spectrometers are considered.

The simulated setup for SFL delayed gamma-ray assay modeling is shown in Figure 47. Assembly and a D-T neutron generator are submerged in water with the 130%-efficient HPGe detectors positioned at a distance of ~90 cm from the assembly center inside an air-filled container. The three HPGe detectors are positioned at each side of the assembly in a way that provides approximately uniform geometric efficiency to the assembly pins, considering the gradient in the neutron source interrogation efficiency on each assembly side. Each detector is enclosed in a lead cave with 1 cm-thick attenuating filter in front, and subtends the full assembly width and approximately 10 cm-high axial length. This detector configuration was fixed for the full range of assemblies included in the three SFLs, without any adjustments for the nominal cooling time and burnup. As a result, this configuration did not keep the predicted count rate in the detectors below the realistic limit for all assemblies. While for the majority of assemblies the count rate was below 100 kHz per detector, a few extreme cases varied considerably from this value. As expected, the highest count rate of approximately 180 kHz per detector was predicted for the high-BU, low-CT assembly with BU of 60 GWd/MTU, IE of 5 wt% and CT of 5 years. The lowest count rate of approximately 15 kHz was determined in the case of the low-BU, high-CT assembly with BU of 15 GWd/MTU, IE of 2 wt% and CT of 50 years. Although both of the extreme cases provided responses with quality sufficient for the subsequent analysis and de-convolution, the modeling technique does not allow investigation of the detector effects in the variable count rate conditions. In future implementations of the delayed gamma-ray assay, it may be crucial to have a capability to adapt the setup configuration to each assembly by means of the variable attenuating filter thickness, detector standoff, or adjustable collimator. Adaptable assay setup can help improve the quality of the response spectra and reduce the intensity requirement for the interrogating neutron source.

The delayed gamma-ray modeling method provided additional insight into the processes occurring over the course of the assay, illustrating its limitations and possible optimization strategies. Figure 48 demonstrates the calculated relative high-energy delayed gamma-ray emission intensity across the assembly pins following the active neutron interrogation in the integrated

instrument assay configuration. This rate is directly proportional to the induced fission rate in each pin and therefore demonstrates the geometric efficiency of the interrogating neutron source to the assembly. The same typical distribution was observed for all modeled assemblies. The highest intensity of the induced fission rate and delayed gamma-ray source signal can be observed in half of the assembly closest to the neutron generator. As the interrogating neutron flux propagates across the assembly, it decreases by the factor of ~2 to 3 and a noticeable intensity gradient is developed. Analysis of the neutron flux in pins from the opposite sides of the gradient demonstrates that the integral flux decreases by the same approximate factor of 2 to 3 at the assembly side opposite to the neutron generator. Energy distribution of the neutron flux is not considerably perturbed and most of the fissions still occur in the thermal energy range. Overall analysis of the integral fission rates and delayed gamma-ray responses across the SFL#2 assemblies consistently indicates that over 80% of the delayed gamma rays above 3 MeV are emitted by fission products from fissile U-235 and Pu-239 isotopes. The rest of the response almost entirely originates from Pu-241 and U-238 fissions, with each of them rarely exceeding 10% of the total intensity.
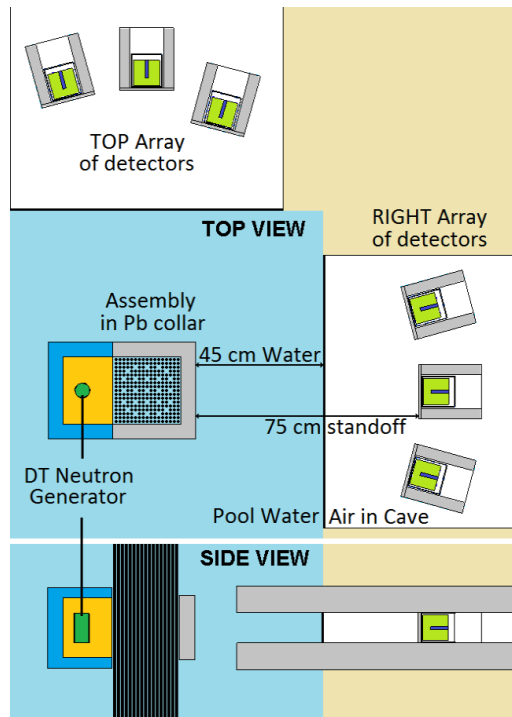
Figure 47. Simulated setup with fuel assembly in water. The neutron generator surrounded by tungsten and stainless steel is placed next to the assembly. The HPGe detectors are positioned ~90 cm from the assembly center inside an air filled container.
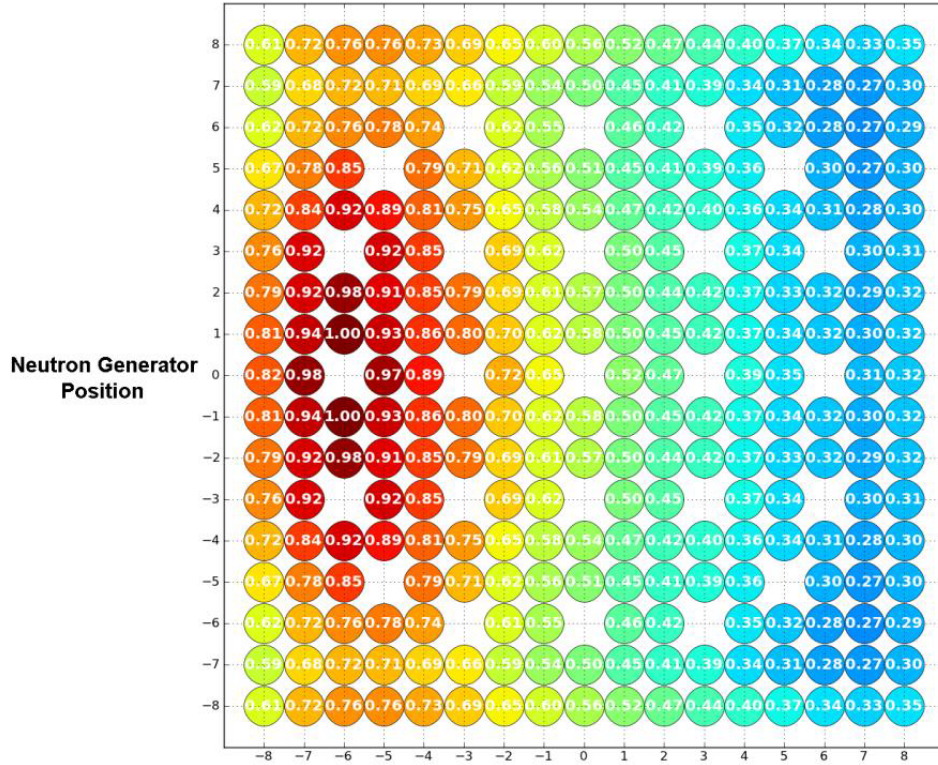
Figure 48. Illustration of the calculated high-energy delayed gamma-ray emission intensity distribution for a typical SFL#2 assembly. Averaged over 15 min measurement time following 15 min irradiation with a DT source in the assumed assay setup.

Figure 49 provides an example of the relative contribution of each assembly pin to the total delayed gamma-ray response spectrum above 3 MeV collected in all three detectors from the assembly side. Asymmetric positioning pf HPGe detectors results in a different geometric efficiency of individual detectors to the pins in the assembly and can be used to compensate for the delayed gamma-ray source intensity gradient. The figure also illustrates the self-shielding effect on the response in the configuration of the 17x17 PWR assembly. The combined effect of the high-density fuel material and periodic structure limit the efficiency of the response collection to a few outer rows of pins at each side of the assembly. This limitation is common to existing passive gamma-ray assay techniques used for spent nuclear fuel characterization.

64
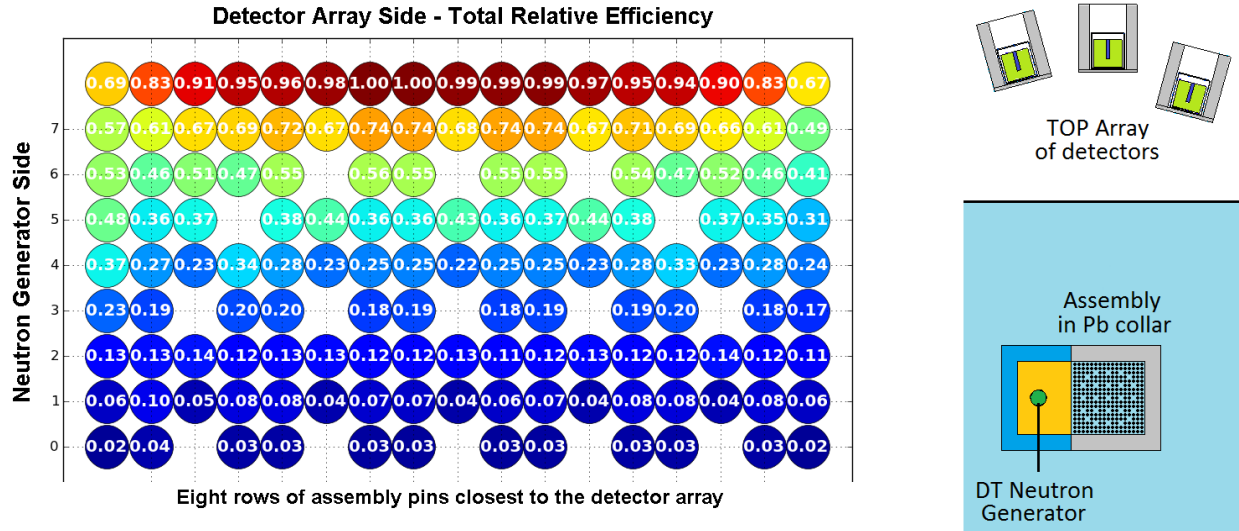
Figure 49. Example of the detector array efficiency to the high-energy delayed gamma-ray response for each assembly pin in one of the modeled configurations.

Despite the constraints of the assumed setup, a delayed gamma-ray response with quality sufficient for analysis was predicted for the full range of the assembly models from SFLs #2, #3 and #4. Modeling observations support the assumption of the theoretical feasibility of this type of assay of spent fuel assemblies using conventional instrumentation. Because of the limiting nature of the passive gamma-ray activity, it is expected that the delayed gamma-ray measurements are more readily applicable to the assemblies with long CTs. More uniform assay efficiency can be potentially achieved for the BWR type assemblies that have smaller dimensions and less compact pin packing. Practicality of the technique can be further improved by considering a different type of interrogating neutron source and its coupling with the assembly, or by deploying gamma-ray spectrometers with higher throughput limits.

III.2.2 Spent Nuclear Fuel Response Modeling and Analysis

Delayed gamma-ray assay of SFL#2 assemblies was modeled assuming the "one-pass" mode with 15 minutes irradiation, 1 minute delay, and 15 minutes detection periods. The DT neutron generator strength was assumed to be $1 \cdot 10^{11}$ n/s. Assay responses for the assumed configuration were calculated in the form of 1) predicted delayed gamma-ray HPGe spectra over a 15 min. acquisition period, and 2) passive gamma-ray spectra obtained assuming the same assay configuration. In order to investigate the effect of the burnup asymmetry in the assembly models, delayed and passive gamma-ray responses were calculated for several positions of the neutron source and detector arrays. Burnup symmetry of the SFL#2 assemblies provided three unique assembly sides for the neutron generator coupling, with a total of seven sets of responses characterizing each individual assembly.

An example of the typical response spectra predicted for the SFL assemblies is shown in Figure 50 for the SFL#2 assembly with BU of 30 GWd/MTU, and IE of 4%. Passive spectra are shown for CTs of 5, 20, and 40 years and depicted together with the activation delayed gamma-ray spectrum which does not change considerably with the cooling time and was calculated at CT of 5 years for this illustration. As commonly observed for all of the assemblies investigated in the current and earlier efforts, the actively induced delayed gamma-ray response is not perturbed by passive

65

emissions interferences at the energy region above ~3.5 MeV. Only few passive lines are present in the spectrum around 3 MeV for the shorter CT fuel and can be easily separated by means of the high-resolution spectroscopy. For the assemblies with long CTs, the delayed gamma-ray signal can potentially be obtained in the energy region that starts as low as ~2 MeV without significant obstructions from the passive continuum. However, the usability of the 2 to 3 MeV energy region is still not clear because in the conditions of the neutron interrogation it can be populated by the activation gamma-ray lines from the common constructional materials and assembly components. Additional observations can be made about the expected detector count rate evolution with cooling time that is governed by the passive response component. The predicted average detector count rate over the 15 min DG response acquisition period decreases by a factor of ~10 between 5 and 20 years CT consistently for all investigated assemblies. A further decrease by a factor of ~3 to ~4 can be observed between 20 and 40 years CT. Lower expected count rates indicate that the DG assay may require an interrogating neutron source of a lower intensity and allow for more efficient detector setups for the assemblies with higher CTs, commonly present in the interim storage facilities.
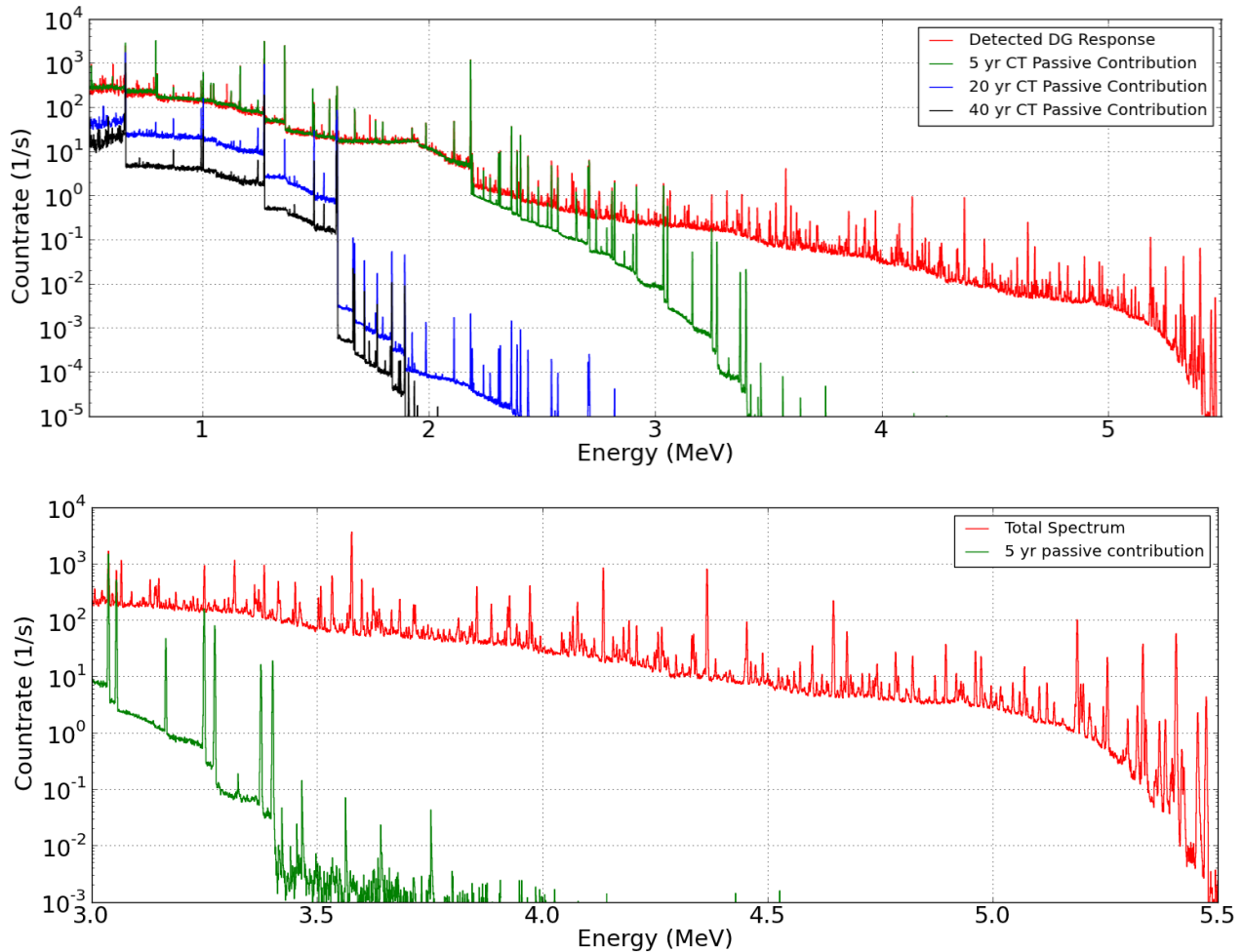
Figure 50. Example of the calculated gamma-ray spectroscopic response of the 30 GWd/MTU BU, 4% IE, 5 yr CT assembly from SFL#2. Bottom section provides a close view of the high-energy DG response region.

The DG response modeling scenario assumed that no a priori information about the assembly is known before the assay, therefore responses from all assemblies were treated and analyzed in an identical manner without being adjusted for a specific BU, CT and IE. For this reason, only the high-

energy region of the activation spectrum above 3 MeV was reported as the DG response and supplied for the analysis directly assuming no need for the background subtraction. A close-up view of this spectrum is shown in the bottom part of Figure 50 for the same assembly with BU of 30 GWd/MTU, IE of 4%, and CT of 5 years. HPGe detectors are expected to provide sufficient resolution and efficiency so that the resulting spectra can be processed with conventional spectroscopic analysis methods. The DG spectrum in the high energy region above 3 MeV contains multiple gamma-ray peaks from the decay of beta-delayed fission products produced over the course of active interrogation. This response can effectively serve as a direct characteristic of the fissionable isotopic content in the assayed material. In the conditions of the spent fuel assembly, it is constrained by the limited geometric efficiency of the detector setup to the assembly pins and by the neutron transport effects during active interrogation. Individual peak and the overall DG continuum magnitudes are always proportional to the intensity of the interrogating source. However, this dependency cannot be straightforwardly used for absolute normalization of the DG response because it is permutated by the presence of neutron absorbers and multiplication effects in the assayed fuel. Although these factors can be potentially corrected in the response analysis if BU, IE and CT are assumed known or measured, the required correlations can be quite complicated and potentially unsustainable for application in the field, therefore were not currently implemented for the DG responses.

Analysis of the high-energy delayed gamma-ray response spectra indicates that the energy region above 3 MeV is almost entirely populated by response from four isotopes that undergo fission in the course of active interrogation: U-235, Pu-239, Pu-241 and U-238. In the conditions of the "one-pass" assay regime characterized by equal 15 min interrogation and acquisition time periods, the response spectrum is dominated by gamma-rays emitted from fission products and their daughter nuclides with half-lives of a several minutes. An experimental and modeling investigation of detectable gamma-ray peaks in these interrogation conditions, concluded that none of them can serve as a reliable unique identifier for any of the U or Pu fissionable isotopes. All of the delayed gamma rays that can be detected with intensity sufficient for the spectroscopic analysis are simultaneously present in the fission-decay chains of all four fissionable isotopes dominating the response. Also, none of the delayed gamma-ray response spectra provided an unambiguous signature that is independent from the assembly multiplication and can be directly related to the total fission rate in the course of the interrogation. These factors precluded development of the delayed gamma-ray response analysis technique capable of the de-convolving the assembly response in absolute terms (such as mass of individual isotopes) without additional inputs from other instruments, calibration standards, or declarations.

While individual delayed gamma-ray peaks detectable in the assumed interrogation conditions are not specific to particular fissionable isotopes, combined analysis of peak areas can provide a relative composition of fissile isotopes in the assayed material. The intensity of each peak is governed by the fission product yields and decay chains that are characteristic of every fissionable isotope. Therefore, peak areas are proportional to the linear combination of fission rates of all actinides in the mixture. Each of the multiple peaks available in the delayed gamma-ray response spectra serve as an independent metric of the cumulative fission rate and can be de-convolved to determine the relative isotope-specific fission rates, and ultimately, the abundance of fissionable isotopes. The underlying method is to approach the set of several individual delayed gamma-ray peaks as a convolution of responses from all four fissionable isotopes significant in the active neutron assay of SNF: U-235, U-238, Pu-239, and Pu-241. In this case, individual intensities of peaks in the total spectrum detected from an assembly can be interpreted as a linear combination of the peak intensities specific for each fissionable isotope, as shown in the equation:

$$Total\ Response = A(U235) \cdot I(U235) + A(Pu239) \cdot I(Pu239) +$$
$$+A(Pu241) \cdot I(Pu241) + A(U238) \cdot I(U238),$$

where parameters A represent isotopic abundances, and parameters I represent isotope-specific delayed gamma-ray response peak areas.

Parameters *A(U235), A(Pu239), A(Pu241), A(U238)*, in this equation determine the relative contribution of responses from each fissionable isotope to the total spectrum. It is assumed that in the case of spent nuclear fuel, the four isotopes are present in a macroscopically homogeneous mixture, experience an identical flux of interrogating neutrons, and are subject to the same detector efficiency. Therefore, these relative contribution parameters are directly proportional to the relative abundances of each fissionable isotope in the activated fuel. De-convolution of the relative abundances for the primary contributing isotopes, can be performed from a set of four equations and therefore requires determining at least four peaks in the total detected response spectrum. With the higher amount of peaks and associated equations, the system becomes over-determined, which increases the confidence of the analysis. The primary condition in this approach is to ensure that peaks selected for the linear combination have substantial contributions from all four fissionable isotopes.

As a crucial requirement for this response de-convolution method, the fissionable isotope-specific delayed gamma-ray peak intensities *I(U235), I(Pu239), I(Pu241), I(U238)*, must be precisely determined. These values are determined for each peak primarily by two factors: (1) probability of the delayed gamma-ray emission following activation, and (2) total detection efficiency for the gamma-ray of this energy in the detector setup. Theoretically, both of these factors can be calculated if the energy dependent fission cross sections, as well as primary fission product yields, branching ratios and half-lives are known or can be determined in laboratory measurements. Similarly, the counting geometry and detector effects may be reproduced in the efficiency calculations for the well-known system. However, the most effective way to determine both factors simultaneously is to perform experimental calibration by activating assemblies with known fuel composition in an actual measurement setup. Such calibration can be effectively performed by measuring a series of fresh (not irradiated) fuel assemblies both with known LEU and MOX composition. This approach for determining the isotope specific peak intensities was assumed for the set of results presented further. A single set of calibration parameters was determined from the delayed gamma-ray spectra obtained from four different LEU and two MOX assemblies and was consistently used to analyze responses from all assemblies in SFL#2, #3, and #4. The principal drawback of the described approach is that it cannot cope with unresolved interferences to the DG peaks and it is sensitive to the accuracy of multiplets fitting and decomposition in the detected spectra. Consequently, this de-convolution method requires analysis of isolated DG peaks, and imposes the ultimate limit on the resolution with which the response gamma-ray spectra can be obtained. This resolution limit has not been investigated at the current stage of the project, and the standard experimentally determined, energy-dependent HPGe detector resolution was assumed for all modeling calculations.

Analysis of the peaks in the high-energy regions of the fissionable isotope-specific spectra revealed that at least 12 predicted peaks are useful for the delayed gamma-ray response de-convolution method. These peaks are indicated in Table VI and were used to analyze results from all modeled assemblies. The table also indicates relative peak intensities specific to the four fissionable isotopes used in the analysis.

Table VI. A list of delayed gamma-ray peaks with isotope-specific relative intensities selected for the response analysis from all modeled assemblies.

Peak Energy, keV	Fission Product	Isotope-specific relative intensity (relative uncertainty)			
		U-235	Pu-239	Pu-241	U-238
3129	Y-95	0.043 (0.015)	0.063 (0.019)	0.059 (0.049)	0.049 (0.050)
3149	Tc-104	0.031 (0.027)	0.134 (0.011)	0.185 (0.022)	0.085 (0.035)
3317	Rb-90*	0.168 (0.005)	0.215 (0.008)	0.166 (0.027)	0.118 (0.027)
3383	Rb-90	0.140 (0.006)	0.087 (0.013)	0.088 (0.032)	0.127 (0.022)
3451	Y-95	0.053 (0.011)	0.082 (0.013)	0.084 (0.033)	0.066 (0.035)
3508	Rb-89	0.056 (0.012)	0.042 (0.024)	0.036 (0.070)	0.049 (0.048)
3599	Rb-91	0.082 (0.008)	0.062 (0.015)	0.063 (0.038)	0.090 (0.027)
3887	Y-95	0.022 (0.020)	0.032 (0.021)	0.032 (0.054)	0.026 (0.061)
3972	Sr-93	0.058 (0.010)	0.071 (0.013)	0.066 (0.034)	0.065 (0.032)
4078	Rb-91	0.030 (0.014)	0.022 (0.026)	0.023 (0.066)	0.033 (0.047)
4135	Rb-90	0.157 (0.005)	0.094 (0.009)	0.098 (0.023)	0.144 (0.017)
4365	Rb-90	0.162 (0.004)	0.096 (0.009)	0.100 (0.022)	0.148 (0.016)

In order to ensure a consistent analysis approach for the predicted spectra for all assemblies, and facilitate data flow, the response analysis technique was fully automated. The processing code is equally capable of analyzing measured or calculated data and accepts two inputs: 1) a raw HPGe gamma-ray spectrum in the form of the energy and number of counts per channel, and 2) the data from Table XX. In the gamma-ray spectrum, the code preforms a search for peaks with centroid energies indicated in the table. For the statistically significant peaks, the Gaussian fit is performed, and peak areas are extracted. For every peak energy, a linear equation combining the measured peak intensity with the isotope-specific data in accordance with equation for the Total Response is prepared as defined above. The resulting set of equations is used to determine the relative peak intensities for the four fissionable isotopes. The system of linear equations is solved as an Orthogonal Distance Regression problem by implementing the Levenberg-Marquardt Algorithm (LMA) [15] with inequality constraints applied to the fitting coefficients. This approach is widely used in physical and engineering studies and involves minimizing the sum of squared distances (that are assumed orthogonal) between each measured data point and the expected valued described by the model equation. Each of the equations describing the measured and isotope-specific peak areas in accordance with the Total Response equation, satisfy a mathematical function of the following form:

$$y = f(x_i; \beta_i), \quad i = 1, \dots, 4,$$

where y is the peak area in the measured spectrum, xi is the pre-determined peak area specific to each of the four fissionable isotopes, and β_i is the isotope-specific contribution to the measured peak area to be estimated. This expression expands to a system of equations where each symbol is associated with a vector of values instead of a single variable. In all cases considered, the number of equations is determined by the number of delayed gamma-ray peaks extracted from the spectrum (12) and is greater than the number of the target parameters (4).

In the basic case, only the measured delayed gamma-ray peak areas are assumed to be measured with errors ϵ_i, and the isotope-specific peak areas are available as precise numbers from a calibration experiment, then the function takes the following form:

$$y = f(x_i; \beta_i) \pm \epsilon_i, \quad i = 1, \dots, 4.$$

Since the errors are assumed normally distributed with mean 0 and variance σ^2, then maximum likelihood estimate of β_i becomes the solution to the least square problem:

$$min_\beta \sum_{j=1}^n [y_j - (x_i; \beta_i)_j]^2, \quad i = 1, ..., 4,$$

where n equals the number of equations.

If necessary, the uncertainty in the isotope-specific peak areas δ_i can also be propagated in the solution, then the minimization problem becomes:

$$min_{\beta,\epsilon,\delta} \sum_{j=1}^n [\epsilon_i^2 + \delta_i^2]_j, \text{where } \epsilon_i = f(x_i; \beta_i) - y_i, \quad i = 1, ..., 4.$$

As indicated earlier in this report, the absolute normalization of the DG responses is problematic in the current setup; therefore de-convolution was performed to determine the relative contribution of the four fissionable isotopes to the observed peak areas. The isotope-specific calibration peak areas were normalized to the sum of number of counts in all 12 peaks for each isotope. In a similar manner, delayed gamma-ray peaks obtained for the modeled spent nuclear fuel spectra were normalized by the sum of counts. As a result, the coefficients β_i that characterize the relative isotopic contribution to the measured response, are expected to be a fraction of a unity. Therefore, the minimization algorithm was executed with the following constraints:

$$\beta_i > 0; 0 \le \beta_i \le 1; \sum \beta_i = 1.$$

A Python program was written to apply this minimization problem to the DG peak data using the LMA method. The same settings and parameters were consistently used to analyze DG responses for all assemblies from SFL#2, SFL#3, and SFL#4.

The described basic analysis method represents only one of several possible DG response analysis techniques and is used here to trace and illustrate the low-level parameter behavior. More complex, high-level methods were also considered. Appendix A demonstrates results obtained with a technique based on the elements of the Principle Component Analysis and Singular Value Decomposition.

DG response spectra were calculated and analyzed for 33 assemblies from SFL#2, 45 assemblies from SFL#3, and 36 assemblies for SFL#4. All data was produced with the same set of assumptions, and in the consistent assay geometry shown in Figure 47. For calculations of DG responses from the SFL assemblies, the neutron generator intensity was assumed at 10^{11} n/s, as the maximum achievable in modern commercial prototypes. The DG assay time regime implemented in the current modeling effort considered 15 min. activation, 1 min. cool-down/movement, and 15 min. spectrum acquisition time periods. DG assay responses were obtained in the form of gamma-ray spectra for each HPGe detector during the 15 min. acquisition period following irradiation with the neutron source. In addition to the actively-induced delayed gamma rays, calculated spectra for SFL#2 and SFL#4 included a passive gamma-ray component arising from the long-lived fission products intrinsically present in the spent nuclear fuel. Response spectra in the high-energy region above 3 MeV were analyzed using the de-convolution algorithm. Calculations were performed for 5, 20, and 40 year cooling times. Considering the symmetry of the material definitions in the assembly pins, seven unique source-detector combinations were analyzed for SFL#2, two for SFL#3, and three for SFL#4.

Figures 51 – 53 illustrate the de-convolution results for the relative fissile isotope abundances produced for all modeled assemblies The solid lines indicate the known, assembly-averaged compositions. The data points show the fractional values for the fissile isotopes ^{235}U, ^{239}Pu, and ^{241}Pu that were determined from the simulated delayed gamma-ray spectra. Several data points for

each assembly correspond to seven unique detector positions in respect to assembly and neutron generator. The reported total uncertainty in each result is cumulative and incorporates uncertainties in the modeled response spectra, peak fitting, and de-convolution technique that are propagated in the results in the form of the standard errors. There are several sources of these uncertainties, including those that appear in realistic experimental conditions:

- All MCNP transport calculations were completed with a target uncertainty of 0.1%, however these are conservatively considered to be "under 1%".

- In processing the delayed gamma-ray responses, the largest uncertainty originates from peak area fits in the modeled response spectra of an assembly. Each assembly-specific response is produced with its intrinsic errors in the peak area fits, explicitly propagated through the analysis.

- The de-convolution technique accounts for the uncertainty of the delayed gamma-ray instrument calibration in the four isotope-specific "basis" peak area sets used in the analysis algorithm.

- The algorithm de-convolves the relative contribution of U-235, Pu-239, U-238, and Pu-241. In the assumed interrogation conditions, the last two contribute to the spectrum on a level comparable with the fitting uncertainty ~5%. This decreases the method's sensitivity to these isotopes, but does not considerably affect separation of U-235- and Pu-239-specific signals in the total response, and determination of Pu-239 relative content. This is the primary limitation of the method, and should be somewhat similar to other NG techniques.

The largest uncertainty in the current set of modeled results originates from the delayed gamma-ray peak fitting error. Although the only peaks with areas exceeding 1000 counts were used for de-convolution, this is not always sufficient to obtain the Gaussian fit with sufficient statistical confidence. There are several ways to reduce this uncertainty by increasing the number of counts in the peak areas:

- Increase the interrogation neutron flux on the assembly. This can be achieved by implementing a more intense DT generator, deploying a linear accelerator-driven neutron source. Also, the delayed gamma-ray response can be measured from the assembly side that was irradiated by the source, if the assembly or instrument movement is allowed during the 1 min separating the irradiation and spectrum acquisition time periods.

- Change the coupling of the neutron source with the assembly. The neutron source can be brought closer to the assembly, and some of the neutron energy spectrum tampering materials can be reduced or eliminated. In contrast to the other proposed neutron generator-based interrogation systems such as delayed neutron or differential die-away, the delayed gamma-ray assay does not require interrogation with mostly thermal neutrons. On the contrary, an increased fraction of fast neutrons can increase the relative contributions from U-238 and Pu-241 to the response, and improve the de-convolution technique performance.

- Include only significant peaks in the analysis and improve calibration approach. With more peaks included in the de-convolution, less uncertainty can be achieved in the result. This is a non-linear process, so it may not be effective for reducing the uncertainty interval, but it can be used to provide more confidence in the result. The peak selection approach and advanced calibration/de-convolution methodology are discussed in Appendix A.

- Adjust the efficiency of HPGe detectors. The assumed configuration of the delayed gamma-ray instrument is fixed to accommodate the detector count rate from the entire range of the SFL assemblies. It is very ineffective for the assemblies with low BU or with long CTs. In the event that it is not required to measure assemblies with very low CTs, the setup of detectors can be

made more efficient by reducing the collimation and standoff. In addition, passive assembly emissions are significantly decreased with time, and additional DG peaks can be harvested in the energy region starting from 2 MeV and above.

De-convolution results for the SFL#2, #3, and #4 when compared with the known assembly-averaged material compositions, demonstrate a consistent offset in the estimation of the U-235, Pu-239, and Pu-241 relative abundances (generally U-235 content is estimated higher and Pu-239 lower). This is the effect of the detectors being mostly sensitive to the outer few rows of pins as discussed earlier. SFL assembly models have asymmetric burnup distribution with the lower BU in the periphery pins when compared with the assembly-averaged value. As a result, estimations illustrated in Figures 51, 52, and 53 are biased and reflect the relative fissile compositions for a slightly lower than expected assembly- burnup.

Overall, the de-convolution results demonstrate a consistent estimation of the relative fissile isotopes abundances for each assembly assay. The uncertainty in U-235 and Pu-239 relative composition for every assembly side and neutron generator position ranges between 1 and 15% and in most cases does not exceed 10%. Averaging among all results obtained for the assembly decreases the uncertainty to approximately 5%.

Modeling of the delayed gamma-ray technique demonstrates its potential as an assay method for determining the relative fissile content of spent nuclear fuel assemblies. It is sensitive to direct signatures of fissionable isotopes in the fuel, and can be easily calibrated with a small set of working standards. After calibration, the instrument can be used for assay of assemblies with any combination of BU, IE, and CT, and will be sensitive to fuel with anomalies in the irradiation history. In addition, delayed gamma-ray responses can be used alongside with results from other fuel measurement instruments in the effort to develop the integrated analysis approach for independent verification of declared fuel properties and partial defects detection. The delayed gamma-ray signature is conducive to development of more sophisticated response analysis methods with some approaches investigated in Appendix A.
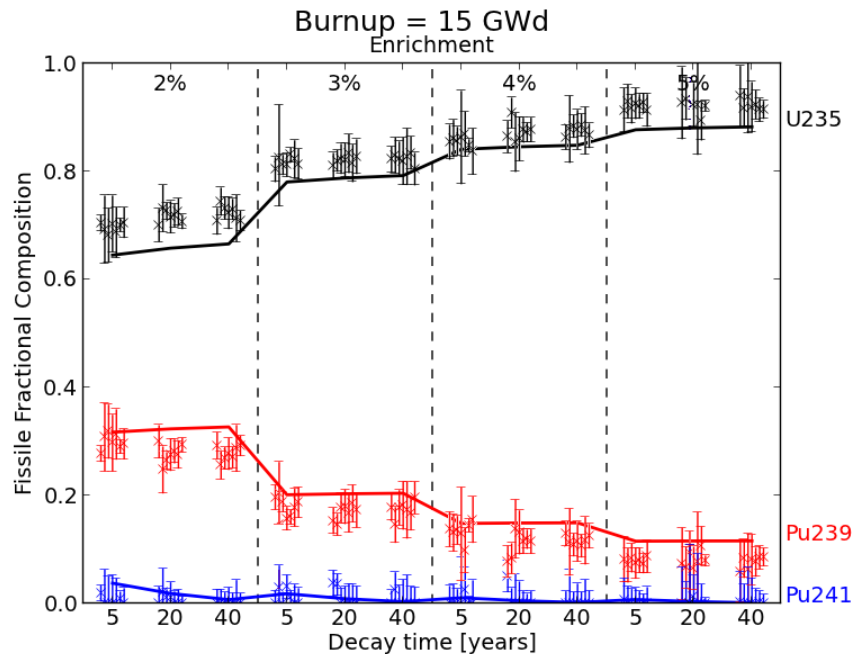

Figure 51 (a). Fissile fractional compositions extracted from simulated delayed gamma-ray spectra for assemblies with 15 GWd burnup, initial enrichment between 2% and 5%, and cooling times of 5, 20, 40 years.

The solid lines show the known, assembly-averaged composition. The data points show the fractional values for the fissile isotopes [235]U, [239]Pu, and [241]Pu that were determined from the simulated delayed gamma-ray spectra for seven different detector positions for each assembly.
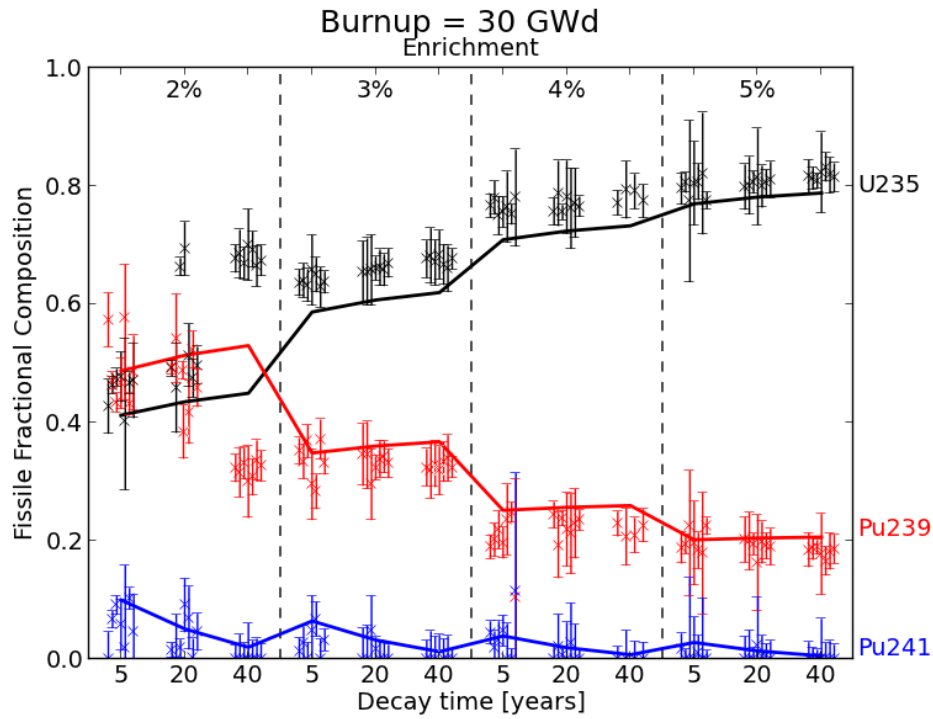

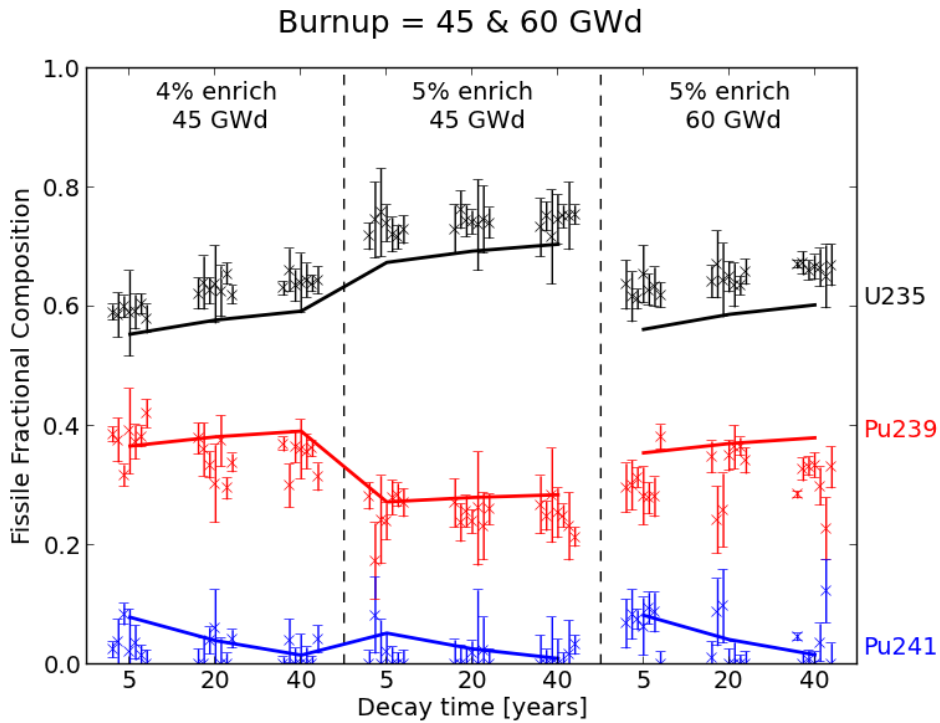Figure 51 (b). Fissile fractional compositions for 30 GWd assemblies.

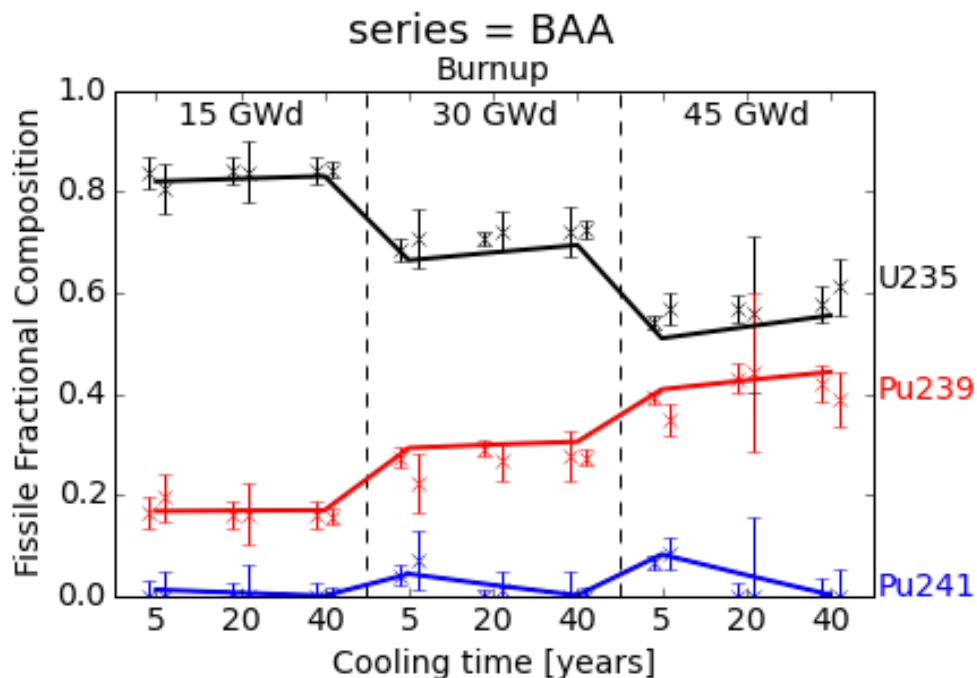Figure 51(c). Fissile fractional compositions for 45 & 60 GWd assemblies.

Figure 52(a). DG response de-convolution results indicating the relative fissile isotopic composition for SFL#3 assemblies. BAA subset of SFL#3 assemblies correspond to the variable boron content in the coolant water assumed during assembly burnup calculations.

Figure 52(b). Delayed gamma-ray response de-convolution results indicating the relative fissile isotopic composition for SFL#3 assemblies. Mod62 subset of SFL#3 assemblies correspond to the variable moderator density assumed during assembly burnup calculations.
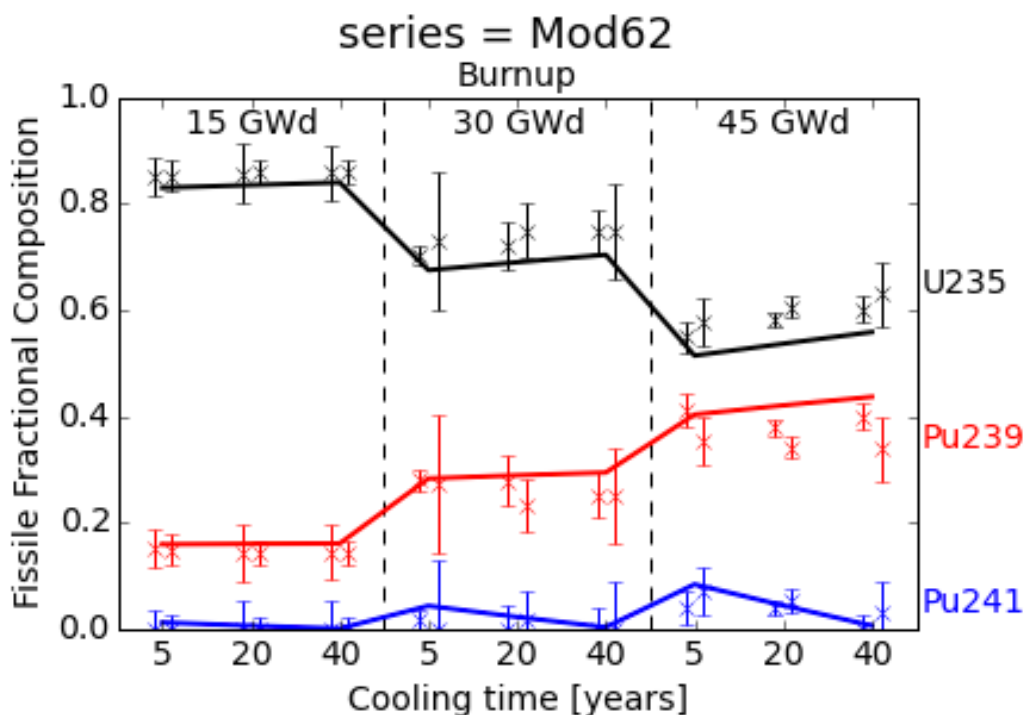
74

Figure 52(c). Delayed gamma-ray response de-convolution results indicating the relative fissile isotopic composition for SFL#3 assemblies. Mod67 subset of SFL#3 assemblies correspond to the variable moderator density assumed during assembly burnup calculations.

Figure 52(d). Delayed gamma-ray response de-convolution results indicating the relative fissile isotopic composition for SFL#3 assemblies. Mod67 subset of SFL#3 assemblies correspond to the variable moderator density assumed during assembly burnup calculations.
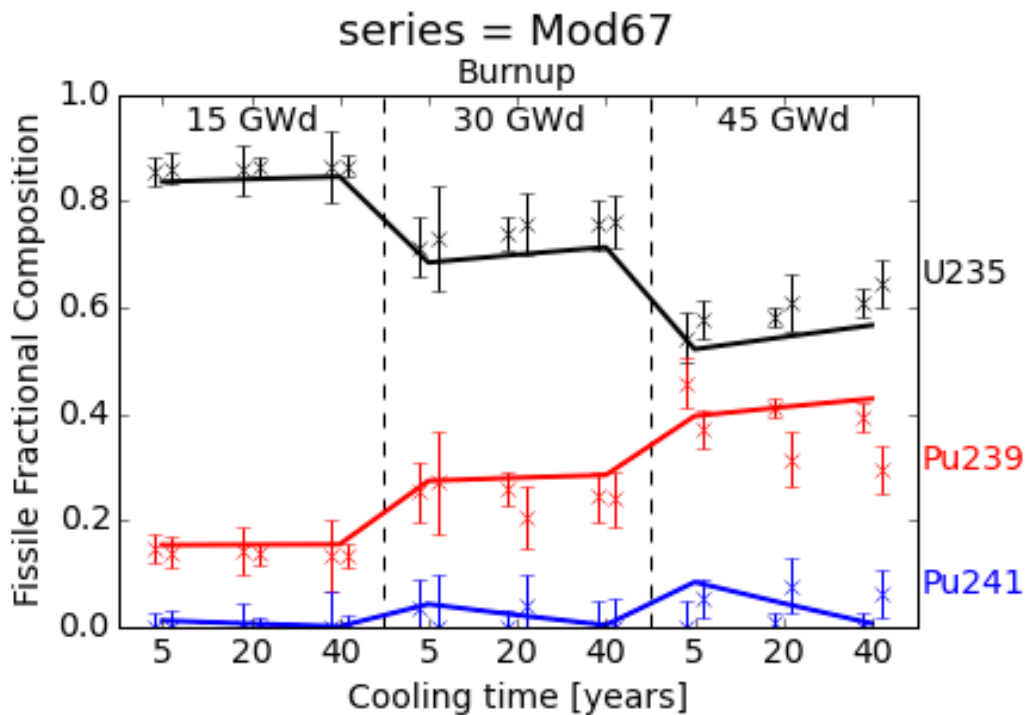
Figure 52(e). Delayed gamma-ray response de-convolution results indicating the relative fissile isotopic composition for SFL#3 assemblies. Mod67 subset of SFL#3 assemblies correspond to the variable moderator density assumed during assembly burnup calculations.
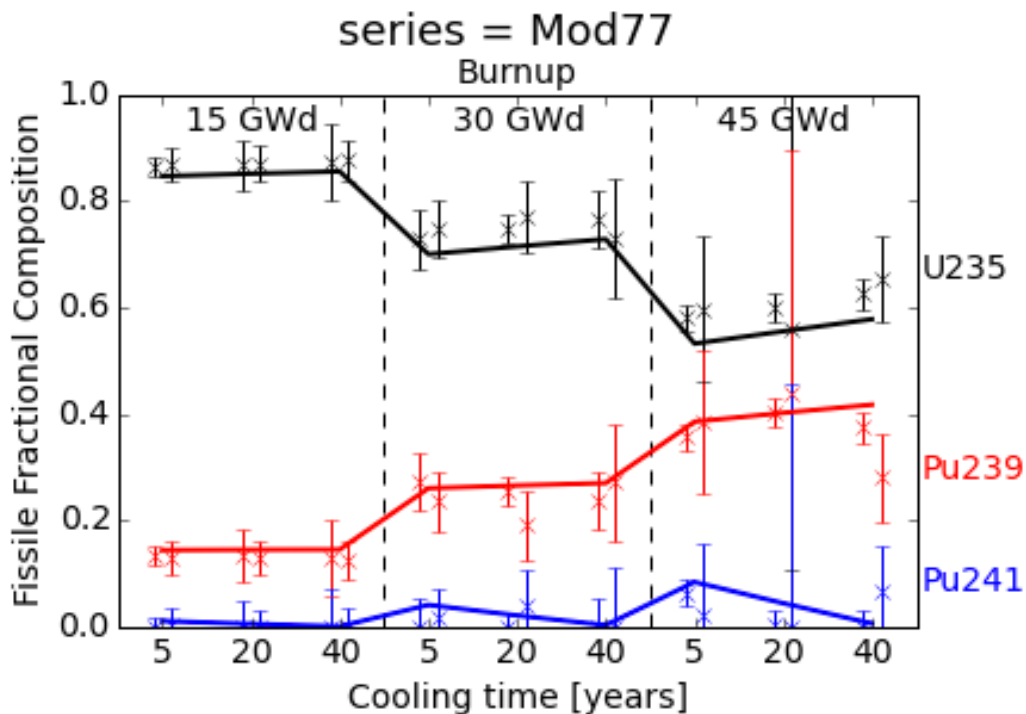

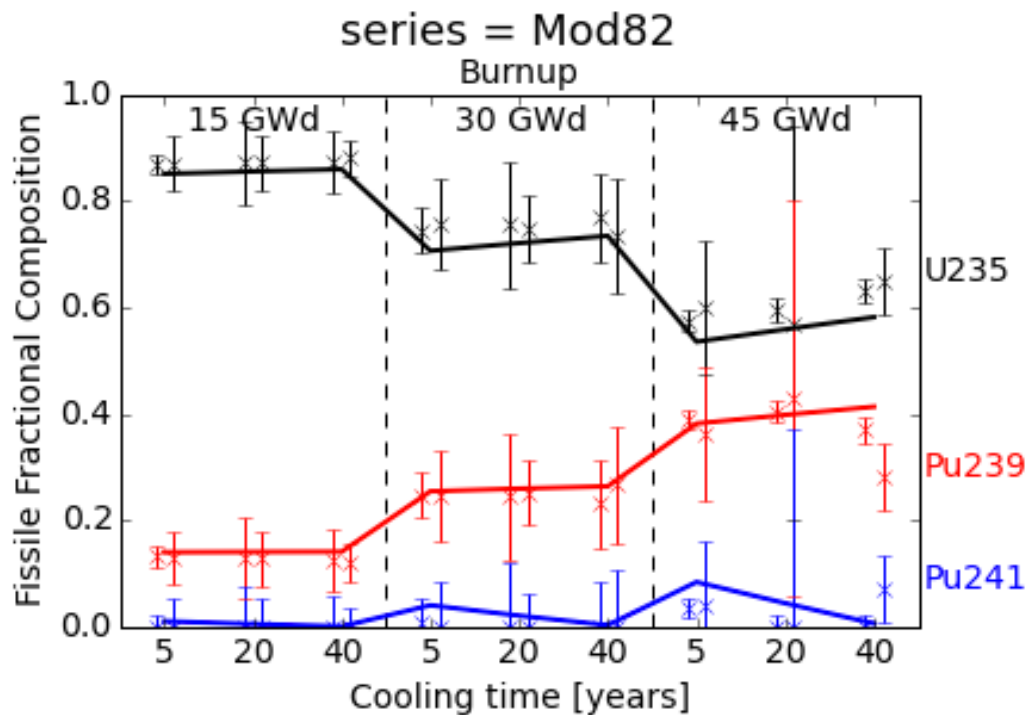Figure 53(a). Delayed gamma-ray response de-convolution results indicating the relative fissile isotopic composition for SFL#4 assemblies. Assembly numbers correspond to a different combination of BU, CT, and IE assumed during assembly burnup calculations.

Figure 53(b). Delayed gamma-ray response de-convolution results indicating the relative fissile isotopic composition for SFL#4 assemblies. Assembly numbers correspond to a different combination of BU, CT, and IE assumed during assembly burnup calculations.

Figure 53(c). Delayed gamma-ray response de-convolution results indicating the relative fissile isotopic composition for SFL#4 assemblies. Assembly numbers correspond to a different combination of BU, CT, and IE assumed during assembly burnup calculations.
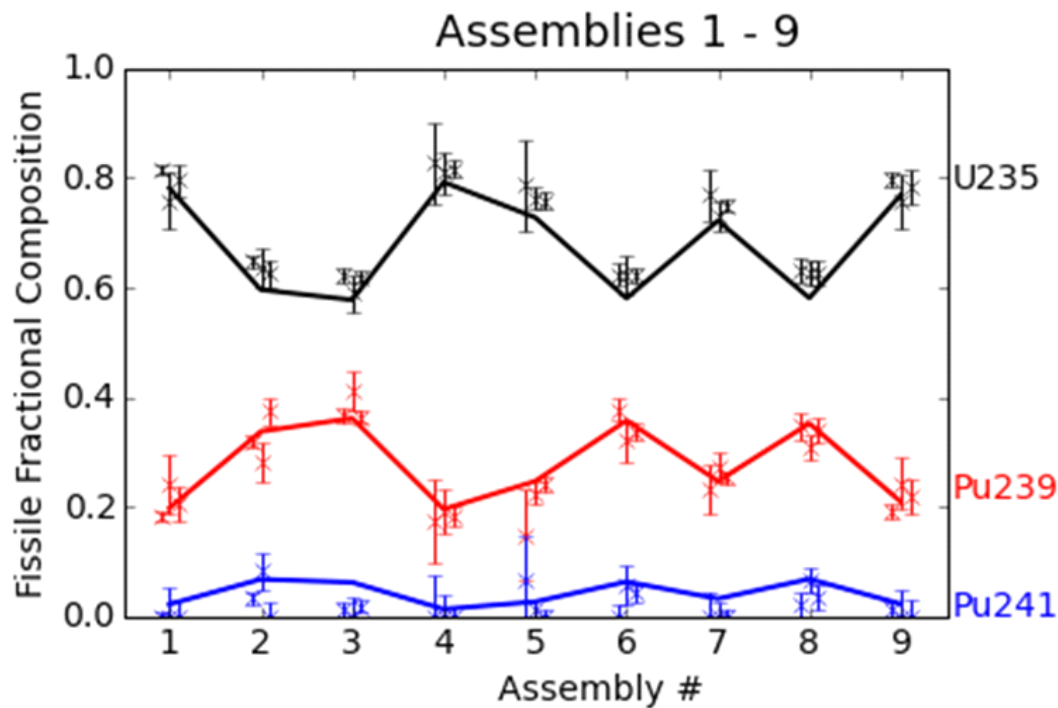
Figure 53(d). Delayed gamma-ray response de-convolution results indicating the relative fissile isotopic composition for SFL#4 assemblies. Assembly numbers correspond to a different combination of BU,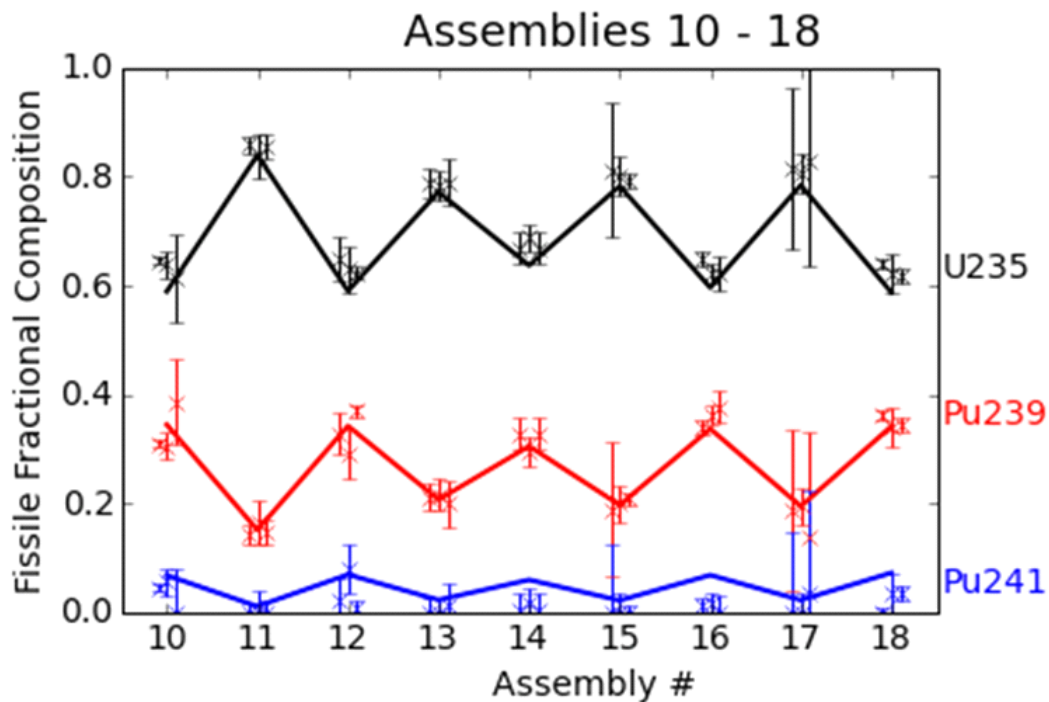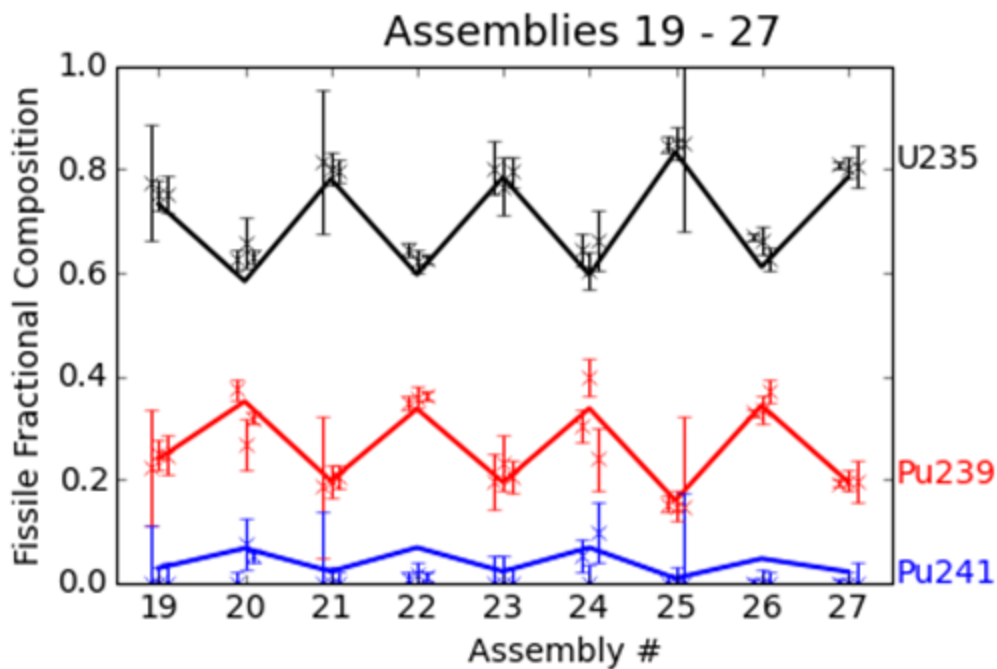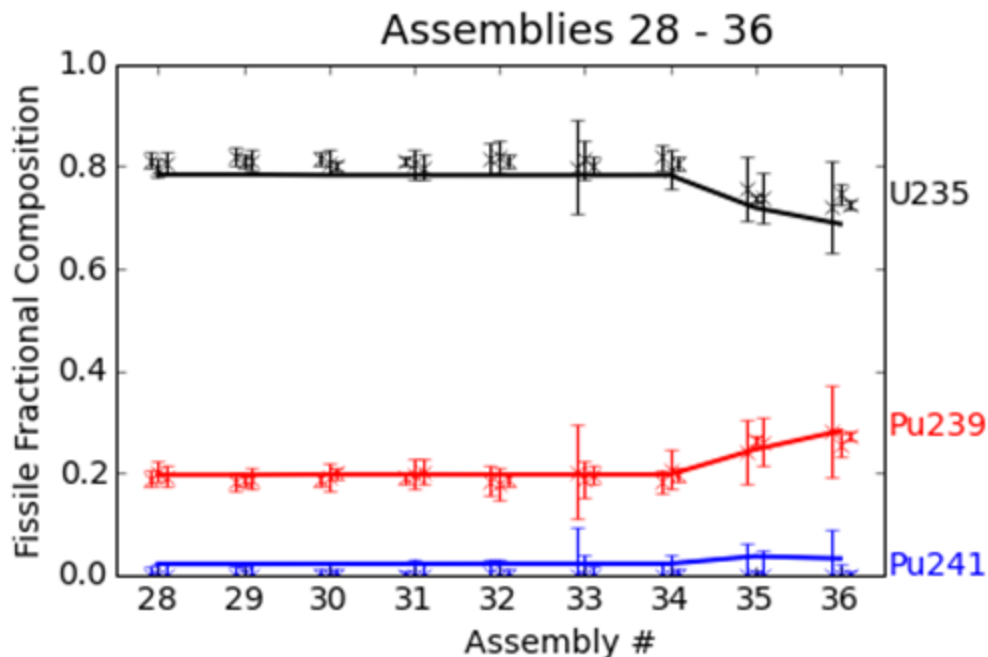 CT, and IE assumed during assembly burnup calculations. Assemblies 28-34 have the same BU, CT, and IE, but have a various amount of fuel pins removed from the central region of the bundle.

III.2.3 Assay Modeling for a Real Spent Fuel Assembly

In order to further investigate feasibility and parameters of spent fuel characterization with the delayed gamma-ray assay technique, a detailed modeling demonstration for a realistic assembly and acquisition setup was conducted. Experimental data from passive high-resolution gamma-ray measurements of real spent fuel assemblies was used to simulate the delayed gamma-ray spectrum that potentially can be acquired under the same conditions, provided that a neutron generator of sufficient intensity can be deployed within the assay setup.

In the course of 2013-14 as a part of the NGSI-SF project, a series of passive gamma-ray spectroscopic measurements of real spent fuel assemblies were completed at the Clab centralized fuel storage facility in Oskarshamn, Sweden. A number of PWR and BWR assemblies with a wide range of burnup, initial enrichment and cooling times were analyzed. The majority of the gamma-ray spectroscopic data was acquired using a HPGe detector system very similar to the spectrometers used in the delayed gamma-ray experiments at the IAC. These measurements utilized an existing penetration through the reloading pool wall with a built-in adjustable collimator. Fuel assemblies were placed in a rotation/translation elevator installed inside the pool. Each assembly was measured at several axial and lateral orientations. The assembly center of rotation was positioned 550 mm from the collimator opening on the inside pool wall, the total extent of the collimator was 1600 mm, vertical collimator opening was 5 mm. The collimator was diverging from the detector front face to subtend the full width of the assembly. Additional gamma-ray attenuating materials were positioned in front of the detector for count rate control and included Pb, stainless steel and copper layers. Schematic of the setup is shown in Figure 54.

The measurement setup at Clab is tailored specifically for passive gamma-ray measurements with energies below 2-2.5 MeV, has low geometric detector efficiency, and would have to be modified to support the delayed gamma-ray assay. The collimator subtends a very small range of the assembly axial extent, and as a result, a considerable fraction of neutron-source induced high-energy delayed gamma-ray signal would not be captured by the detector. A collimator that diverges in the vertical direction and opens up to a lager axial region of the assembly would be more appropriate for the delayed gamma-ray collection in this scenario. Additional improvement can be gained with optimization of the neutron generator position and attenuating filter thickness.

Following the passive gamma-ray measurements of the Clab assemblies, each of them was modeled in with high fidelity using the detailed operator supplied data. Burnup modeling for several axial regions in each assembly pin were completed at ORNL. Extended material compositions at discharge were extracted from the burnup calculations and used as an input for the delayed gamma-ray modeling technique described earlier in this report. Pin-specific material inventories were advanced from the time of discharge to the cooling time of the real measurement. Passive and activated delayed gamma-ray spectra were calculated and plotted together with the actual measured response.

For modeling of the delayed gamma-ray spectrum in this configuration, it was assumed that a DT neutron generator is submerged in the vicinity of the assembly inside the storage pool. To compensate for the detector setup inefficiencies, the neutron generator output was assumed to be $1 \cdot 10^{12}$ n/s. The delayed gamma-ray assay assumed the "one-pass" measurement with 15 min interrogation, 1 min delay, and 15 min spectrum acquisition periods. The modeled results are shown in Figure 55, and indicate a reasonable intensity of delayed gamma-ray lines above 2.5 MeV. Delayed gamma-ray response in this energy region dominates the passive spectrum and individual peaks can be collected with the accuracy that is potentially sufficient for the analysis. This simplified example is not comprehensive, but it points at the delayed gamma-ray response measurement feasibility in the conditions of the spent fuel storage pool. However, the neutron generator intensity remains an important constraint, and any future investigations should consider a careful choice of the neutron source type, intensity, and coupling with the assembly. Potentially, an accelerator-driven interrogation setup, similar to the one used at the IAC can be a reasonable choice for this application.
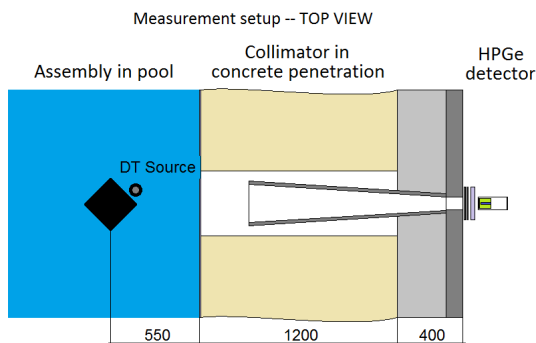

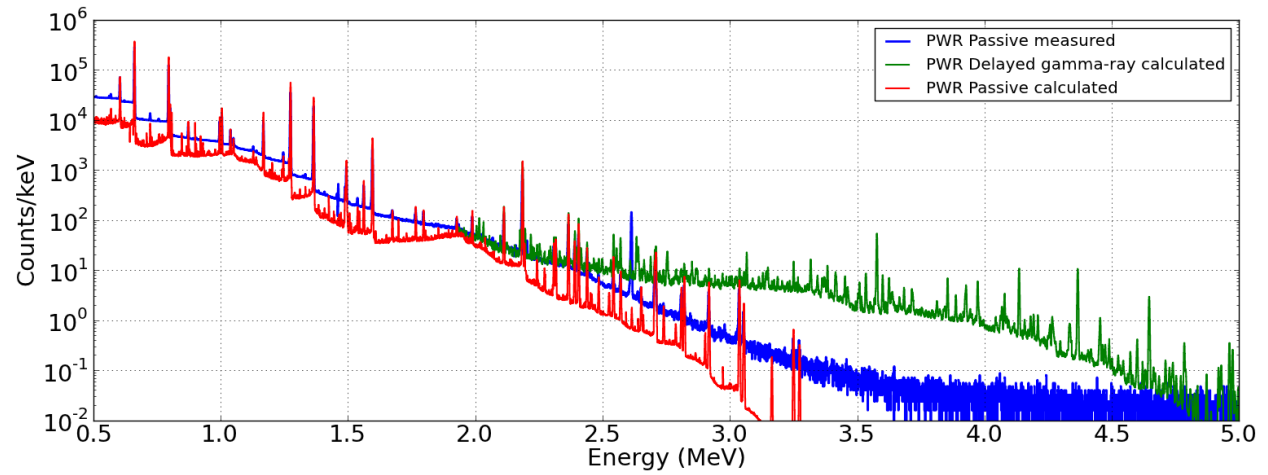Figure 54. Schematic of the real spent fuel assembly measurement setup.

Figure 55. Real spent fuel assay modeling: an overlay of the passive measured, passive calculated and activated delayed gamma-ray spectra from a real spent fuel assembly. Passive background is subtracted from the measured spectrum up to 2.2 MeV, the Tl-208 background line at 2.614 MeV is visible.

IV. High-Rate Spectroscopy Detector Study

In high-energy, beta-delayed gamma-ray spectroscopy of nuclear spent fuel delayed gamma-rays of up to ~7 MeV must be detected on an intense background of lower energy gamma-rays from long-lived fission products and a very high count-rate capability is essential for efficient measurements. The requirements for the gamma-ray detection system include high efficiency at high gamma-ray energies, high energy resolution, good linearity between gamma-ray energy and output signal amplitude, ability to operate in a very high count-rate gamma field, and ease of use in industrial environments such as nuclear facilities. High Purity Germanium Detectors (HPGe) are the state of the art but the maximum count rate is limited to less than 150 kcps. Lanthanum Bromide (LaBr$_3$) scintillation detectors with a fast light-decay time of 16 ns can operate at more than an order of magnitude higher rates but at a reduced energy resolution. In addition, these detectors offer a higher efficiency at higher gamma-ray energies due to the higher-Z material and do not need a cooling system. [16,17] Thus LaBr$_3$ detectors may be an effective alternative for nuclear spent-fuel applications in spite of their lower energy resolution. The spectroscopy performance of a LaBr$_3$ system at high gamma input count rate was investigated and delayed gamma-ray spectra of [235]U and [239]Pu targets were measured with this detector.

IV.1 Characterization of Spectroscopic LaBr$_3$ Detector

In the first research phase, the performance of a 2" (length) x 2" (diameter) LaBr$_3$ scintillation detector was evaluated at high gamma-ray count rates that may be encountered in spent nuclear fuel applications. The detector configuration was optimized for high count rate studies and included a negatively biased photomultiplier (PMT) (PM R6231-100 Hamamatsu with 8.5 ns rise time), to avoid a long decay time constant caused by a coupling capacitor, coupled with a tapered active high voltage divider [18] in order to preserve good photoelectron collection (for good resolution) and gain linearity at high gamma-ray energies. The PMT signal was amplified by a charge sensitive RC preamplifier. The design decay-time constant was chosen to be low, 40 µs, in order to avoid preamplifier saturation at high count rates. This time constant is about the minimum that most Multichannel Analyzers (MCAs) can accommodate using Pole-Zero (P/Z) compensation. Additionally, in order to preserve the fast rise time of the LaBr$_3$ detector, a fast operational amplifier, an ADA4817 with a 1 GHz bandwidth and 870 V/µs slew rate, was selected for the preamplifier. The spectroscopic measurements were performed with a nanoMCA produced by LabZY LLC [19]. An important feature specific to this MCA is the availability of two compensation filters that allow the removal of some detector pulse tails caused by slow rise time. The parameters for these filters were adjusted to minimize the duration of both fast and slow channel pulses since they directly affect pileup rejection and dead time performance. Other important parameters include detection thresholds (for slow and fast channel), which were set manually at about 50% above the automatically detected noise level at low rates. Automatic threshold setting was disabled to avoid unknown behavior in high count-rate conditions. Spectra were acquired at 16k channels.

Combinations of ^{137}Cs and [232]Th gamma sources were used the detector testing. The sealed [232]Th source provided the highest available gamma-ray energies of up to 2614 keV. The dual source method was used to determine the dead time losses in the peak: a set of ^{137}Cs sources generated different count rates up to ~2.7 Mcps in the detector system, while the highest energy gamma line (2614 keV [232]Th) was observed. The [232]Th source was kept at a fixed position relative to the detector for providing a constant count rate.

81

The spectroscopy parameters (FWHM, net peak area, peak position) were studied as function of the estimated MCA input count rate. Because the MCA may introduce count-rate bias due to imperfect dead time correction at high count rates, we assessed the MCA's performance in these conditions. Using a Kiethley 6497 pico-ampere meter, we directly measured the current from the PMT's anode, which is proportional to the charge produced by the detector in a given time, independent of the pileups. Therefore, as long as the PMT remains linear and the average energy distribution of the incoming gamma rays is constant, the current value is proportional to the gamma count rate.

Figure 56 shows that the incoming count rate estimation of the MCA increases linearly with the current produced by the detector. In this set of measurements the count rate due to ^{232}Th was fixed at about 40 kcps, while the count rate was varied with the ^{137}Cs source. At high count rates, where the count-rate contribution of ^{232}Th was negligible, we were assessing the effect of the MCA dead time correction. The linear behavior exhibited is indication of good dead time correction in the nanoMCA used.
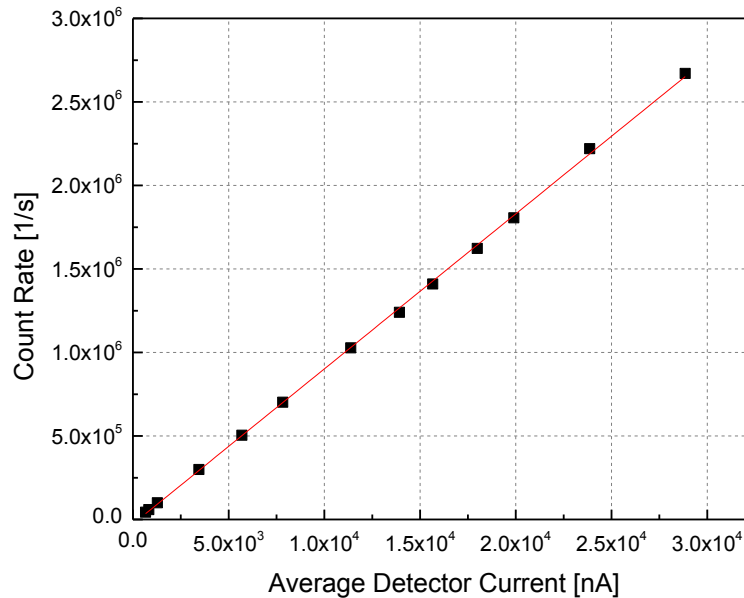
Figure 56. Measured anode current vs. estimated incoming count rate values as reported by the nanoMCA. The R-square value of the linear fit to the data is 0.9996.

At each count rate (data points in the Figure 56) spectra were collected or MCA live times of 200 s and spectroscopy characteristics extracted. Sample spectra are shown in Figure 57 for count rates of 100 kcps, 500 kcps, 1.4 Mcps, and 2.7 Mcps. The effects of the pile up at higher input count rate are visible, as well as a shift of peak position.
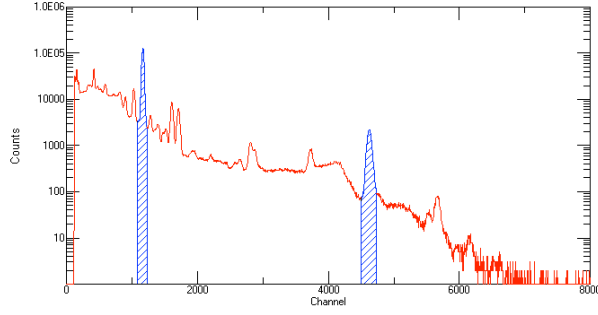
(a) Count rate 100 kcps, dead time 7.5%
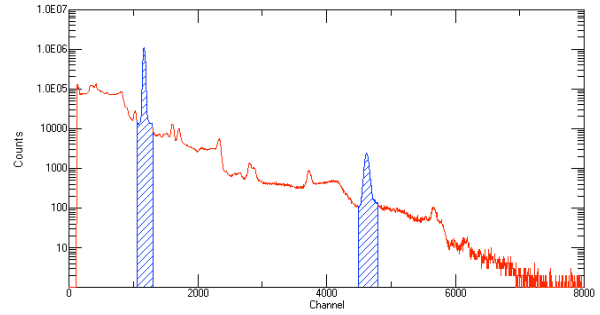
(b) Count rate 500 kcps, dead time 32%

(c) Count rate 1.4 Mcps, dead time 67%

(d) Count rate 2.7 Mcps, dead time 88%

Figure 57. Gamma-ray spectra collected using ^{137}Cs and [232]Th sources at different count rates. From (a) to (d) count rate range from 100 kcps to 2.7 Mcps. ROIs for the 661.7 keV (^{137}Cs) and 2614 keV([232]Th) peaks are indicated in each spectrum.

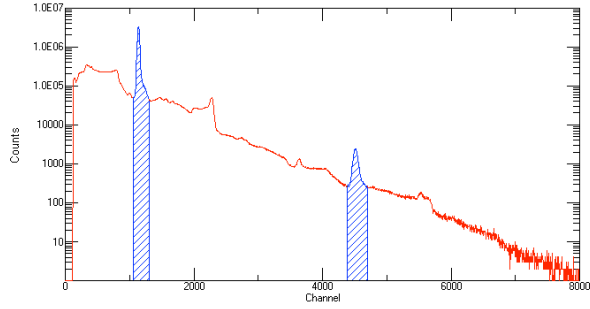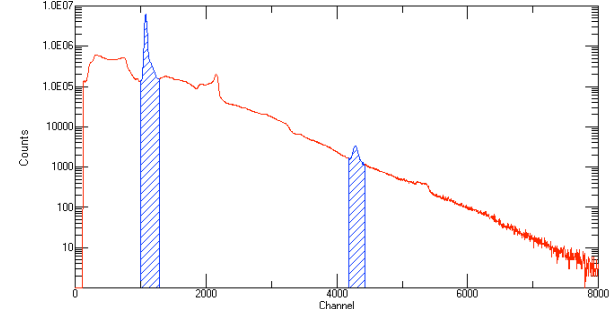For each spectrum we extracted the variation of the 2614 keV gamma line of the [232]Th source net peak area as a function of count rate. In addition, peak positions (in channels) and energy resolutions (measured as FWHM in %) were determined as a function of count rate of both the [137]Cs 661 keV gamma line and the 2614 keV gamma line of [232]Th. The results are summarized in Figures 58-60.

The normalized net area of the [232]Th gamma line as a function of the background count rate is shown in Figure 58. Up to 2.2 Mcps the decrease in integrated peak counts is less than 5 %, and at 2.7 Mcps the loss is less than 20%. Figure 59 shows the shift in peak position for the ^{137}Cs and the [232]Th gamma-ray peaks as a function of count rate. At the highest count rate the shift to lower energy is about 8% for both peaks. Figure 60 shows that the energy resolution (reported FWHM in %) changes only slightly. Even at the highest rate, the FHWM of the Cs line increased only from 2.9% to 3.1%, while the Th line was unchanged with a width of 1.5% FWHM. This is an indication of good pileup-rejection and well-functioning auxiliary MCA services, such as base-line restoration, pulse shaping, and pulse tail compensation.
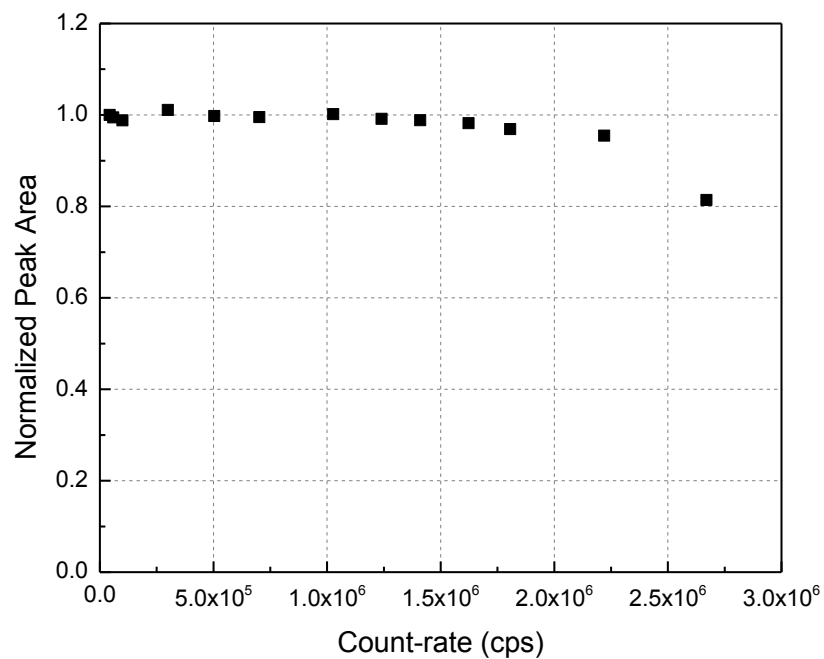
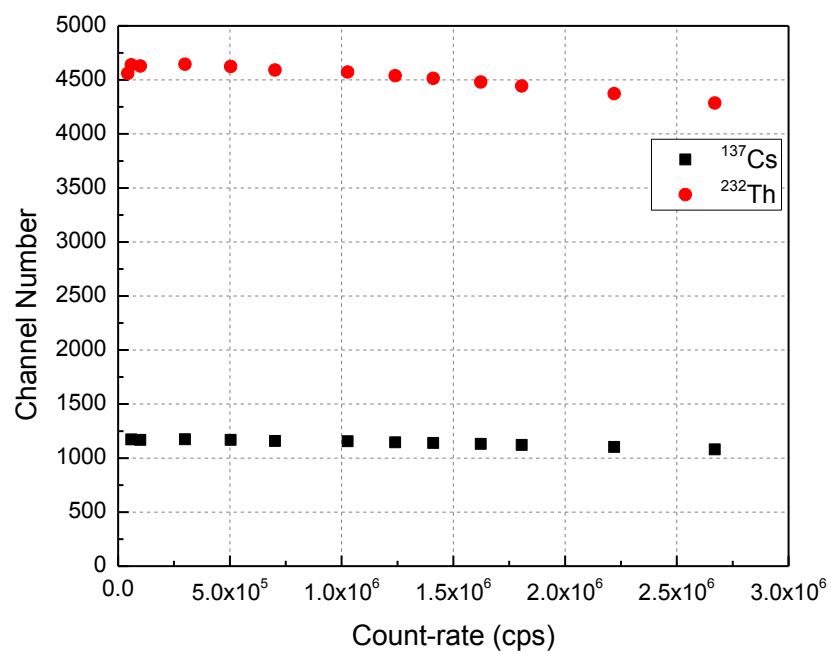Figure 58. ^{232}Th line net area (normalized) as a function of count rate.

Figure 59. Peak positions, in channel number, of ^{137}Cs and ^{232}Th gamma lines as function of count rate.
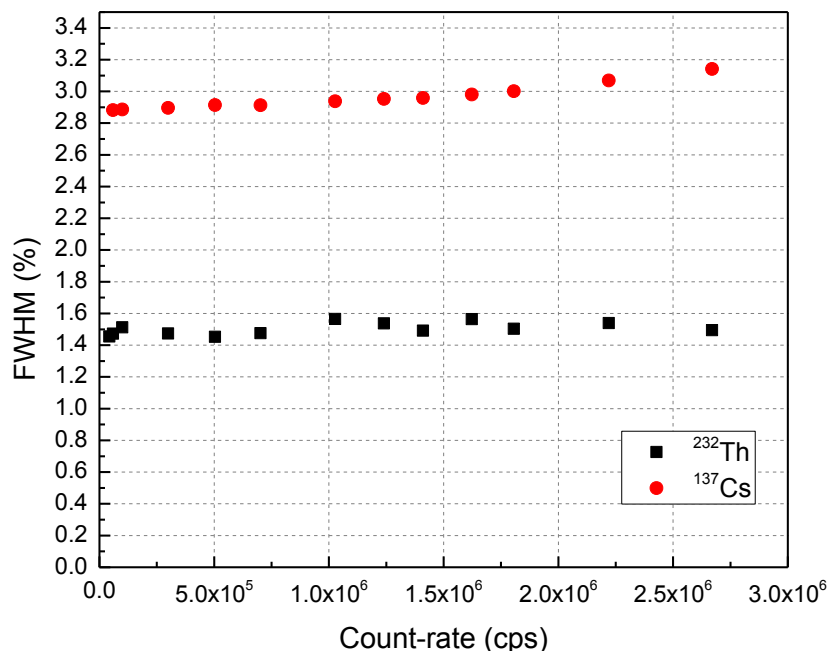
Figure 60. Variation of the energy resolution, measured as FWHM in %, of the ^{137}Cs and [232]Th gamma lines with increasing of count rate.

Note that the setup used with ^{137}Cs and [232]Th for this experiment simulates the situation in spent fuel, where the high passive gamma background is mainly due to ^{137}Cs, and its effect on the DG peaks, at energies of several MeV, must be understood to effectively perform DG spectroscopy of nuclear material.

IV. 2. Delayed Gamma Measurements on [235]U and [239]Pu Targets with a LaBr$_3$ Detector

Experimental measurements were conducted at the Idaho Accelerator Center, where [235]U and [239]Pu samples were irradiated with neutrons from a photoneutron source. Data were taken for several irradiation/spectroscopy cycle times from 10/10 seconds to 15/15 minutes. For the 10/10 seconds measurement the LaBr$_3$ detector was located at the neutron irradiation station, which caused high backgrounds in the gamma-ray spectra due to neutron activation. For the other measurements the targets were transferred to the spectroscopy station behind a shielding wall. Presented below are spectra recorded with the LaBr$_3$ detector for the 15 minutes neutron irradiation followed by 15 minutes of spectroscopy measurements. The LaBr$_3$ scintillation detector was surrounded by 1/8 inch of lead to filter out low energy gamma rays. Delayed gamma-ray spectra up to 7 MeV were acquired by repeating irradiation and spectrum collection 4 times and summing the spectra, which were corrected for any gain drifts. The time for transferring the samples from the irradiation location to the measurement station was about 20 s.

Figure 61 a,b,c compares the [239]Pu delayed gamma-ray spectrum with the [235]U spectrum after live-time normalization. Significant differences between the two spectra are observed for the peaks above ~3.5 MeV. The large [95]Y is approximately the same but the higher energy [90]Rb peaks are significantly stronger for [239]Pu than for [235]U. These differences in peak ratios offer the possibility to determine the relative contributions of these two isotopes to the DG spectrum measured for a mixed target.
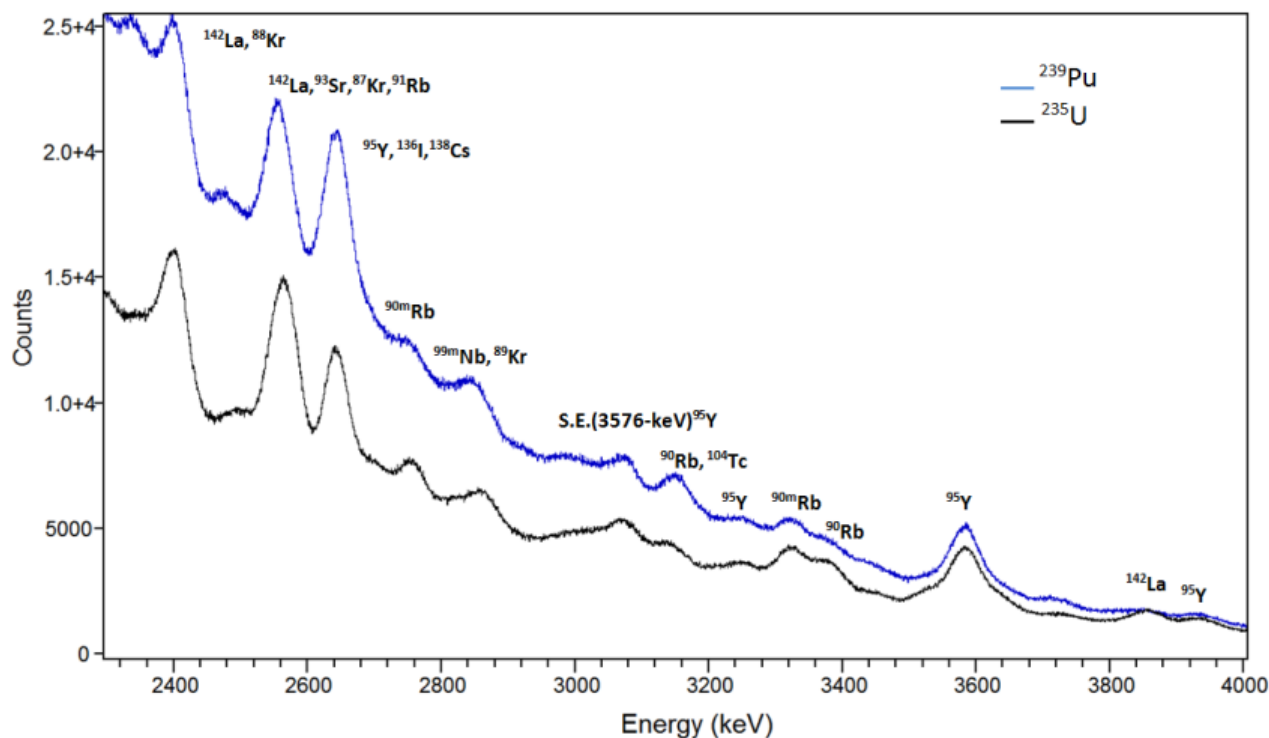
Figure 61 a. Delayed gamma-ray spectra of ^{239}Pu and ^{235}U from 2.3 to 4 MeV. Both spectra were acquired with the LaBr3 detector and 15/15 minute cycle times. Live-time normalizations were applied to the spectra.
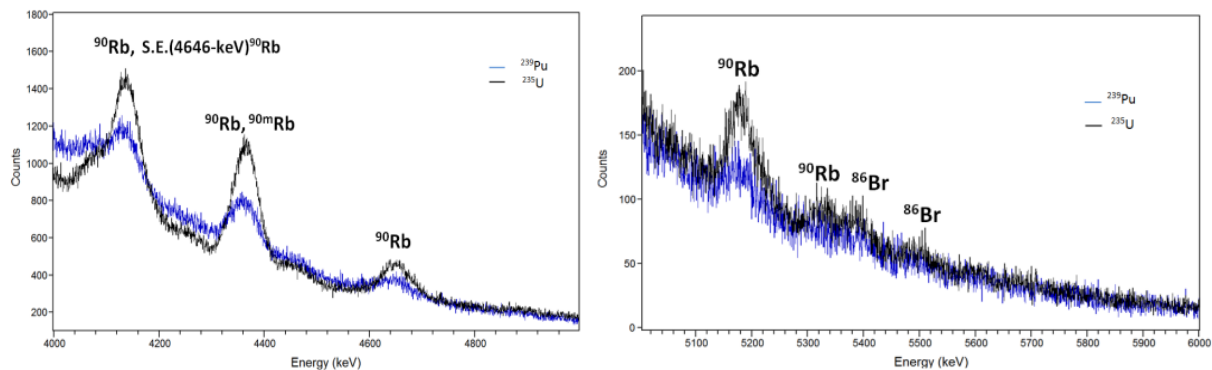
Figure 61 b,c.   Delayed gamma-ray spectra of ^{239}Pu and ^{235}U f rom 4 to 5 MeV (on left) and 5 to 6 MeV (on right). Both spectra were acquired the LaBr3 detector and 15/15 minute cycle times. Live-time normalizations were applied to the spectra.

Characterization of gamma-ray spectroscopy with a LaBr$_3$ 2"x2" scintillation detector coupled to a nanoMCA found excellent spectroscopic performance at high count rates up to 2.7 Mcps. An experimental methodology was developed that uses the average current from the PMT's anode and a dual source method to characterize a detector at very high count rates. Delayed gamma-ray spectra from ^{235}U and ^{239}Pu targets were acquired, analyzed and compared. The preliminary results suggest that a LaBr$_3$ detector system could be a useful alternative to an HPGe detector for delayed gamma-ray spectroscopy in applications, where the high count-rate capability outweighs the lower energy resolution. The observed significant differences between the ^{235}U and the ^{239}Pu delayed

gamma-ray spectra may be exploited to non-destructively determine fissile fractions. The results of the LaBr$_3$ detector study were presented by A. Favalli at the NMM 55th Annual Meeting [20].

V. Conclusions

Experimental measurement campaigns were carried out at the IAC using a photo-neutron source and at OSU using a thermal neutron beam from the TRIGA reactor to characterize the emission of high-energy, beta-delayed gamma-rays from ^{235}U, ^{239}Pu, and ^{241}Pu targets following neutron induced fission. Data were collected for pure and combined targets for several irradiation/spectroscopy cycle times ranging from 10/10 seconds to 15/30 minutes. The IAC data including accumulated spectra, raw list-mode data, laboratory notebooks and other ancillary data, have been uploaded to a data server and team members or other researchers may request access to the data for analysis.

A plethora of delayed gamma-ray lines from short-lived fission products was identified in the 3-6 MeV energy range, a low background region that is most useful for safeguards applications, and examined for potential impact on delayed gamma assays. The ^{235}U/^{239}Pu line ratios vary considerably with several lines much stronger for ^{235}U fission. For shorter irradiation/spectroscopy periods two lines of ^{106}Tc with a half-life of 36 s are prominent in the ^{239}Pu spectra but nearly absent in the ^{235}U spectra and thus a strong indicator of ^{239}Pu fission. For best utilization of delayed gamma-rays from fragments with short half-lives and for maximizing the sensitivity of a ^{235}U/^{239}Pu measurement, 1 to 2 minutes long irradiation/spectroscopy periods appear optimal. A series of repeated measurements may be required to achieve statistical quality of the delayed gamma-ray response peaks in this regime. For a specific application background from neutron activation may need to be considered if the detectors are located near the neutron source.

The delayed gamma-ray signature of ^{241}Pu, a significant fissile constituent in spent fuel, was measured using 90/90 seconds irradiation/spectroscopy cycles and the collected spectra were compared to those of ^{239}Pu. The ^{241}Pu/^{239}Pu ratios varied between 0.5 and 1.2 for ten prominent lines in the 2700-3600 keV energy range. These significant differences in relative peak intensities will likely allow the determination of relative isotopic fractions in a mixed sample. Also measured were combined ^{235}U, ^{239}Pu, and ^{241}Pu targets in order to experimentally test the sensitivity of a delayed gamma assay but the data analysis has yet to be performed.

A method for determining fission product yields by fitting the energy and time dependence of the delayed gamma-ray emission was developed and demonstrated on a limited ^{235}U data set. Significant discrepancies with values in the ENDF/B-VII.1 nuclear data library were found. Future work should include fitting more data sets over larger energy ranges to reduce the uncertainties of the extracted fission yields. By applying the fitting procedure to the full energy and temporal range of the measured data, improved fission product yields could be obtained for all three isotopes, ^{235}U, ^{239}Pu, and ^{241}Pu.

De-convolution methods for determining fissile fractions were developed and tested on the experimental data. Using a set of selected well-identified peaks above 3 MeV yielded good results, whereas spectral component analysis methods using larger sections of the delayed gamma spectra to lower statistical uncertainties suffered from systematic errors.

A high count-rate LaBr$_3$ detector system was investigated as a potential alternative to HPGe detectors for delayed gamma-ray spectroscopy in applications where the high count-rate capability may outweigh the lower energy resolution. Characterization of a LaBr$_3$ scintillation detector

87

showed sufficient spectroscopic performance at count-rates exceeding 2 Mcps. Measured ^{235}U and ^{239}Pu delayed gamma-ray spectra exhibited significant differences in relative peak intensities indicating the possible use of a LaBr$_3$ detector for delayed gamma assay but further assessment of measurement sensitivities and systematic uncertainties is needed.

Modeling capabilities were added to the existing framework and codes were adapted as needed for analyzing experiments and assessing application-specific assay concepts including measurements over many short irradiation/spectroscopy cycles. The code package was benchmarked against the data collected at the IAC for small targets and the assembly-scale data collected at LANL. Study of the delayed gamma-ray spectroscopy applications for nuclear safeguards was performed for a variety of assemblies from the extensive NGSI spent fuel library using the developed simulation technique. The modeling results indicate that the delayed gamma-ray responses can be collected from spent fuel with statistical quality sufficient for analyzing the isotopic composition of an assembly using COTS instrumentation. Delayed gamma-ray measurement setup configuration is flexible and can be adjusted to a specific field conditions, or may be coupled with other spent fuel assay instrumentation. The measurement setup assumed in this study is not optimal and requires an optimized DT neutron generator coupling with the assembly. Despite this, a it is possible to conclude that a 10^{11} n/s source intensity is sufficient to acquire delayed gamma-ray spectra from spent nuclear fuel assemblies with cooling time and burnup values typical for spent fuel storage pools.

Analysis and de-convolution of the delayed gamma-ray response spectra modeled for spent fuel assemblies was performed using the same method that were applied to experimental spectra. At least 12 DG peaks in the energy region between 3 and 4.5 MeV were identified as sensitive to the fissionable isotopic content of the fuel. Modeled assay results were processed to determine the relative fissile isotopic compositions. The baseline de-convolution algorithm was calibrated assuming preliminary measurements of fresh LEU and MOX assemblies with known fissile material compositions. The analysis method demonstrates that assembly-averaged relative fissile isotopic fractions in measured fuel assemblies can be determined with uncertainties on the order of 10% for Pu-239 and U-235. A major contribution to the uncertainty can be attributed to the fact that the detectors are mostly sensitive to the outer few rows of pins while the burnup and thus the isotopic concentrations may vary considerably between the periphery and the central region of a real assembly. For the same reason, the relative fissile compositions determined from the delayed gamma-ray responses are slightly biased relative to the known assembly-average isotopic content. For the simulated measurements on model assemblies of the NGSI Spent Fuel Libraries, uncertainties in the U-235, Pu-239, and Pu-241 relative abundances were approximately 5% when averaged over all detector positions around an assembly.

Overall, the delayed gamma-ray assay technique demonstrates a potential as feasible method for determining the relative fissile content of spent nuclear fuel assemblies, and special nuclear materials in general. It is sensitive to direct signatures of fissionable isotopes, and response analysis can be calibrated with a small set of working standards. Although the methodology for the absolute normalization of the delayed gamma-ray response may not be straightforward, this method can be used alongside other measurement instruments in an effort to develop an integrated analysis approach for detailed fissile material composition characterizations.

VI. References

[1]   B. B. Cipiti, "Advanced Instrumentation for Reprocessing," Sandia Technical Report No. SAND2005 6223 (2005).

[2]   L. E. Smith, S. Tobin, M. Ehinger, A. Dougan, B. Cipiti, A. Bakel and R. Bean, "Safeguards Enhancement Study," Pacific Northwest National Laboratory Technical Report No. PNNL 18099 (2008).

[3]   Uncertainty Analysis of the SWEPP Plutonium Sources (NADS and ZPPRS), Idaho National Engineering and Environmental Laboratory Engineering Design File No. EDF-3153 (2002).

[4]   L.W. Campbell, "Fitting Methods for Delayed Gamma Spectroscopy Data," Technical Report PNNL-SA-99655, Pacific Northwest National Laboratory, Richland, WA, 2013

[5]   M. B. Chadwick et al., "ENDF/B-VII.1 Nuclear Data for Science and Technology: Cross Sections, Covariances, Fission Product Yields and Decay Data," Nucl. Data Sheets **112**, 2887 (2011).

[6]   J. K. Tuli, Evaluated Nuclear Structure Data File: A Manual for Preparation of Data Sets, Brookhaven National Laboratory Technical Report No. BNL-NCS-51655-01/02 (2001).

[7]   Williford, RS. 2013. "Temporal Gamma-Ray Spectrometry to Quantify Relative Fissile Material Content," Oregon State University, Corvallis, OR: Nuclear Engineering. PhD Dissertation.

[8]   L.W. Campbell, "Fitting Methods for Delayed Gamma Spectroscopy Data," Technical Report PNNL-SA-99655, Pacific Northwest National Laboratory, Richland, WA, 2013.

[9]   R. B. Firestone, Table of Istopes 8th edn. (John Wiley & Sons, New York, New York, 1996).

[10]   M. A. Humphrey, S. J. Tobin, and K. D. Veal, "The Next Generation Safeguards Initiative's Spent Fuel Nondestructive Assay Project," Journal of Nuclear Materials Management Vol. **40**, No.3, p. 6 (2012).

[11]   W. B. Wilson et. al., "A Manual for CINDER'90 Version 07.4 Codes and Data," Los Alamos National Laboratory, LA-UR-07-8412 (2008)

[12]   National Commission on Radiation Protection, "Radiation Protection for Particle Accelerator Facilities," Report No. 144, Bethesda (2003).

[13]   Y. Kong, et. al., "Linearization of Gamma Energy Spectra in Scintillator-Based Commercial Instruments," IEEE Trans. Nucl. Sci. 57 1430 (2010).

[14]   J. D. Galloway, H. R. Trellue, M. L. Fensin, and B. L. Broadhead, "Design and Description of the NGSI Spent Fuel Library with an Emphasis on Passive Gamma Signal," Journal of Nuclear Materials Management, Vol. **40**, No. 3, p. 25 (2012).

[15]   D.Marquardt, "An Algorithm for Least-Squares Estimation of Nonlinear Parameters," SIAM Journal on Applied Mathematics 11 (2). 431–441 (1963).

[16]   A. Favalli et al., "Investigation of the PGNAA using LaBr$_3$ scintillation detector," Applied Radiation Isotopes, 68, 901-904, 2010.

[17]   A. Favalli et al., "Wide energy range efficiency calibration for a lanthanum bromide scintillation detector," Radiation Measurements, Vol.43, issue 2-6, 2008.

[18]   R.W. Engstrom, Photomultiplier Handbook, Theory and Design Applications, RCA Corporation, 1980.

[19]   www.labzy.com (May 2014)

[20]   A. Favalli et al., "Delayed Gamma-Ray Spectroscopy with Lanthanum Bromide Detector for Non-Destructive Assay of Nuclear Material," Proceedings of the INMM 55th Annual Meeting, July 2015, Atlanta.

VII.   Appendix A

Advanced Delayed Gamma-ray Response Analysis Techniques

Prepared by Cliff Chen, Vladimir Mozin,

Lawrence Livermore national Laboratory

Active neutron interrogation of a spent fuel assembly produces a characteristic delayed gamma-ray spectrum for each isotope undergoing induced fission. If the spectra from each isotope are known and they are sufficiently distinct, the isotopic content of the assembly can be de-convolved from the measured spectrum. While in principle the isotopic responses can be calculated from nuclear data, effects such as passive gamma-ray background, neutron absorbers in the fuel, and instrument response will modify the theoretical spectrum and cannot be explicitly approximated through simulations. In practice, a set of measurements on known reference assemblies will likely be used as a response basis for calibration of the delayed gamma-ray analysis technique.

Once the response basis is known, the de-convolution of the isotopic fractions can be assumed to first order to be a straightforward weighted, linear multiple regression problem, which has a number of well-established solution techniques. The only additional constraint placed on the solution is the inequality constraint the isotopic fractions should be greater than zero.

This appendix discusses three different types of reference bases, methods for de-convolving the isotopic fractions, and approaches for optimizing the spectral peak selection and choice of reference assemblies. Isotopic fractions are calculated for simulated assemblies from Spent Fuel Library #2 (SFL#2) and are compared to the known simulated compositions. Isotopic fractions from unknown assemblies of SFL#4 are also presented.

Peak fitting of the Raw Spectrum

The delayed gamma-ray response simulations of the spent fuel assemblies convolve the gamma emission with the response function for a simulated High Purity Germanium (HPGe) detector. From this spectrum, only peaks above 3 MeV were used in order to minimize the passive gamma background contribution. Prominent peaks were visually selected and the total peak areas were integrated with a Gaussian fit using a commercial spectroscopy package.

90
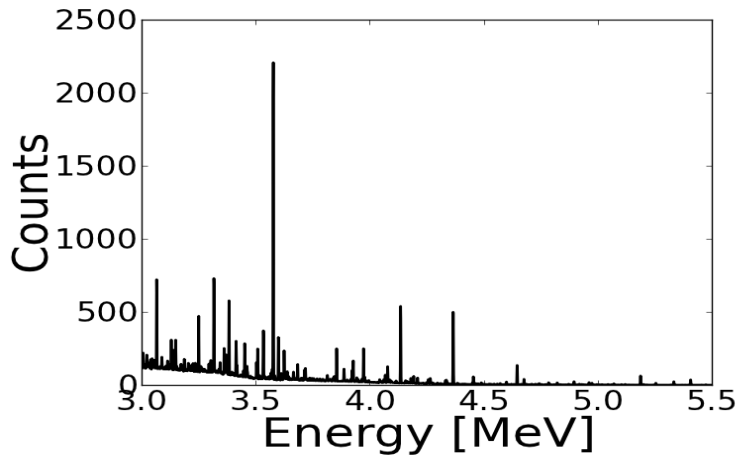
Peak Energies (MeV)		
3.037	3.317	3.855
3.055	3.383	3.887
3.066	3.452	3.973
3.130	3.509	4.078
3.149	3.534	4.136
3.187	3.577	4.366
3.250	3.600	4.646

Figure A1. Sample DG response spectrum above 3.0 MeV showing prominent peaks. A total of 21 peaks can be observed in the energy region between 3.0 and 4.7 MeV.

Peak areas obtained by Gaussian fitting are more useful for the response analysis because they are less sensitive to noise and instrumental effects than peak heights or spectral regions. 21 peaks were identified in the predicted DG response spectra and peak areas calculated for each assembly. A sample spectrum with prominent peaks is shown in Figure A1, along with a table listing the peak energies.

Calculating Isotopic Compositions

There are three ways to calibrate the DG response analysis technique by establishing reference isotope-specific signatures:

1. Measurements from pure isotopic samples.

2. Fresh LEU and MOX fuel assemblies.

3. Fresh and well-characterized spent fuel assemblies.

Under option 1, signatures would be derived from small quantities of isotopically pure material samples. These responses would need to account for the geometric, self-absorption, and noise present in a full assembly assay setup, potentially using detailed transport simulations. However, it is difficult to properly account for realistic conditions through modeling, and this introduces a degree of simulation uncertainty that is somewhat difficult to quantify. Options 2 and 3 require the use of working standards, assemblies with known fissile compositions that are used to calibrate the system. Using only fresh fuel is less complex and would not require spent fuel assemblies of known composition. They also do not complexities associated with the passive radioactive background intrinsic for the real spent fuel. Mathematically, the inversion of the signals leads directly to the isotope fractions in Option 1. Options 2 and 3 require a second mapping from the fuel assembly basis to the isotopic fractions.

Response Matrices

In order to investigate the optimal DG signature analysis and calibration methods, we define the following array response shape parameters:

Parameter	Definition	Value
i	# isotopes of interest	4
n	# spectra peaks	4 - 21
k	# of basis assemblies	≥ 4

The present analysis considers i = 4 isotopes of interest: U-235, Pu-239, Pu-241, U-238. A total of n high-energy DG peaks are used for the de-convolution, which is at least i and up to the full 21 peaks identified earlier in the gamma-ray spectrum. The optimal peak set is discussed in the next section. Value k is the number of reference assemblies used for calibration, which not less than i.

We also define the following response matrices and vectors discussed in this section.

Parameter	Definition	Shape
y	Signal vector of peak areas	$n \times 1$
f	Isotope fractions for isotopes of interest	$i \times 1$
a	Vector of components in assembly basis	$k \times 1$
R	Signal response for each basis assembly (each column represents the peak areas for each basis assembly)	$n \times k$
X	Signal response matrix augmented with signal vector y	$n \times (k+1)$
α	Vector of components in transformed basis	$(k+1) \times 1$
F	Composition matrix of reference assemblies	$i \times k$

The signal response is given by

$$Ra = y,$$

where y is the vector containing the peak areas. R_{nxk} is the response matrix for each assembly, where each of the k columns is a set of n peak areas for a reference assembly. Also, ak is the unknown basis vector representing the linear contributions of each of the reference assemblies to the total signal. There are more peaks than assemblies ($n > k$), resulting in a regression inversion.

The isotope composition is calculated from ak based on the known compositions of the basis assemblies. This is given by

$$f = Fa,$$

where each column of F represents the isotopic fractions of the k basis assemblies. If using the pure isotopic basis, F is just the identity matrix. An inequality constraint ($f_i \geq 0$) can also be incorporated if the optimal solution contains negative isotopic components.

Solution methodology

The optimal solution technique that is required to de-convolve partial isotopic contributions to the detected DG response depends on the choice of one of the three calibration basis types. For the pure isotopic basis, only the first equation needs to be solved. The use of the Levenberg-Marquardt Algorithm (LMA) with inequality constraints has been discussed in the main part of this report. The

LMA works for most linear and non-linear optimizations but is not necessary for a linear system. The Moore-Penrose pseudo-inverse of R_{nxk} provides the least-squares solution for f_i, equivalent to solving the normal equations. This is shown by:

$$Ra = y$$
$$R^T Ra = R^T y$$
$$VS^T U^T USV^T a = VS^2 V^T a = VS^T U^T y$$
$$a = VS^{-2} V^T VS^T U^T y = VS^{-1} U^T y = R^+ y$$

If the inequality constraint is desired, the Karush-Kuhn-Tucker (KKT) conditions [A1] can be numerically solved to provide the constrained solution.

The use of a fresh or a spent fuel assembly basis requires an additional step to calculate the isotopic composition. If an inequality constraint is not necessary, the calculation of f_i directly follows the calculation of ak by multiplication of the known F composition matrix. If an inequality constraint is needed, transformation of the basis using singular value decomposition simplifies the calculation. This change of basis simplifies the mapping of the inequality constraint on f_i to constraints on ak.

First, the response matrix of k known reference assemblies is augmented with the signal vector itself, such that:

$$X a_{k+1}^* = y.$$

The base solution of $a = [0,0……0,1]$ is true by definition. However, a Singula Value Decomposition (SVD) of the new response matrix can be used to change the basis. X is conventionally decomposed into $U_{nxn} S_{nxk} V^T_{kxk}$. Since for $n > k$, the last $n - k$ rows of S are 0, an alternate form of the SVD is $U_{nxk} S_{kxk} V^T_{kxk}$, where U is a rectangular unitary matrix such that $U^T U = I_{k.k}$. Thus, we have

$$U(SV^T a) \equiv U\alpha = y$$
$$\alpha = U^T y.$$

Since the response matrix was augmented with the signal vector, this is now an exact solution instead of a least squares solution. Additionally, as U is rectangular unitary, α can be calculated from the $U^T y$. The second step maps the α basis to the isotopic fractions. Previously the mapping was

$$F^+ f = a.$$

Transformation to the α basis gives

$$U^T RF^+ f \equiv Cf = \alpha.$$

F^+f maps f to the a basis. $R(F_+f)$ maps f to the signal basis. $U_T(RF^+f)$ maps f to the α basis. Note that since we only have k known assemblies in the matrix R, this basis will not fully span α. Thus, the solution to $Cf = \alpha$ is now a least squares solution. The net effect of this transformation simply shifted the regression from the calculation of the basis vector to the calculation of the isotopic fractions. However, the inequality constraint is now straightforward.

Assuming peak errors are uncorrelated, the errors in the peak fits are incorporated by weighting the response matrix. The solution is given by

$$R^T W R a = R^T W y,$$

where W is the diagonal matrix with entries $1/\sigma^2_{ii}$. Thus transformation to $R' = wR$ and $y' = wy$ where $w = 1/\sigma_{ii}$ provides the weighted least squares solution using same techniques previously discussed. Incorporation of errors in the basis assemblies can be incorporated in a total least squares method but has not yet been done.

Errors in the isotopic fractions are calculated from the covariance matrix using standard techniques. Since the least squares minimization occurs in the second step, this is calculated from $(C^T C)^{-1}$. The parameter errors are given by

$$\sigma_{f_i} = \frac{residual}{dof} (C^T C)^{-1}_{ii}.$$

One qualification is that since the different reference assemblies have different isotopic compositions, they also have different multiplications. The absolute signal for each basis vector needs to be appropriately scaled. While relative multiplication can be estimated, to first order the sum of the peak areas is proportional to the total number of fissions. Thus, normalization of the basis spectra with the total spectral sum is a reasonably effective.

Optimization Techniques

Two optimization steps were performed for unfolding the isotopic fractions: peak selection and spent fuel basis selection. A training set selected from SFL#2 was used for optimization. For peak selection, subsets of 5-20 peaks were explored in every combination to determine the set that maximizes the accuracy and precision of the predicted isotopic fractions. The rationale behind not using the entire set of peaks is that some peaks may be contaminated by passive gamma background, and thus increase the error associated with the measurement. Other peaks may also not be sufficiently resolved, and undetected peak overlap may be an additional complicating factor.

For fresh and spent fuel basis selection, different combinations of 5 basis assemblies are selected from LEU and MOX fuel assemblies and the spent fuel assemblies in SFL#2. Different combinations were used by varying enrichment, burnup, and cooling time, while the neutron source and detector positions around the assembly are randomly selected from seven possible orientations.

In order to optimize against a training set, a scoring methodology was developed that balances the accuracy and precision of the calculated isotope fraction. The scores are calculated on an absolute error basis (e.g. 3% ± 1% U-235 is equivalent to 2 – 4% U-235), as opposed to relative fractional error. Using a relative fractional error over-weights the accuracy of components contributing to the response on the lower scale, such as Pu-241. The score for each isotope is given by

$$S_{iso} = \frac{1}{\sqrt{p^2 + (f_{calc} - f_{actual})^2}},$$

where p is the absolute percentage error calculated for that isotope. The score for an assembly sums the isotope scores in parallel, so that high accuracy for one isotope does not dominate the score for that assembly. This is given by

$$\frac{1}{S_{assembly}} = \frac{1}{N_{iso}} \sum_{iso} \frac{1}{S_{iso}}.$$

94

The score for a given set of peaks or a given set of basis assemblies is again summed in parallel and is given by

$$\frac{1}{S_{RA\,set}} = \frac{1}{N_{assembly}}\Sigma_{training\,set}\frac{1}{S_{assembly}}.$$

There are two types of scores calculated, S_{all} and $S_{fissile}$, which represent the scores for all isotopic compositions, which is generally dominated by the U-238 content, and the fissile composition, which presents the fraction of each fissile isotope to the total fissile content (e.g. $f_{U235}/(f_{U235}+f_{Pu239}+f_{Pu241})$)).

Peak Selection

Of the 21 peaks listed in Figure A1 table some were excluded due to poor fits in the peak fitting step. 12 peaks were initially selected for use in the initial analysis. In order to optimize the peak selection, a score for every combination $n = 5 – 20$ peaks was calculated across the training set using the pure isotopic calibration basis. The training set was selected from 60% of the assemblies in SFL#2. A cross-validation set for selection of n and a test set each represented 20% of the assemblies.

The fissile scores for $n = 5$ are shown in Figure A2 (left). The best $S_{fissile}$ is about 20, representing accuracies ~3.5% for each of the fissile isotopes. The best S_{all} is not shown but is approximately 2.5 (~28% error), due primarily to poor predictions in the U-238 isotopic fraction. Figure A2 (right) shows the best $S_{fissile}$ as a function of n. The best combination was selected for each n using the training set, and the $S_{fissile}$ in this figure was calculated from the cross-validation set.
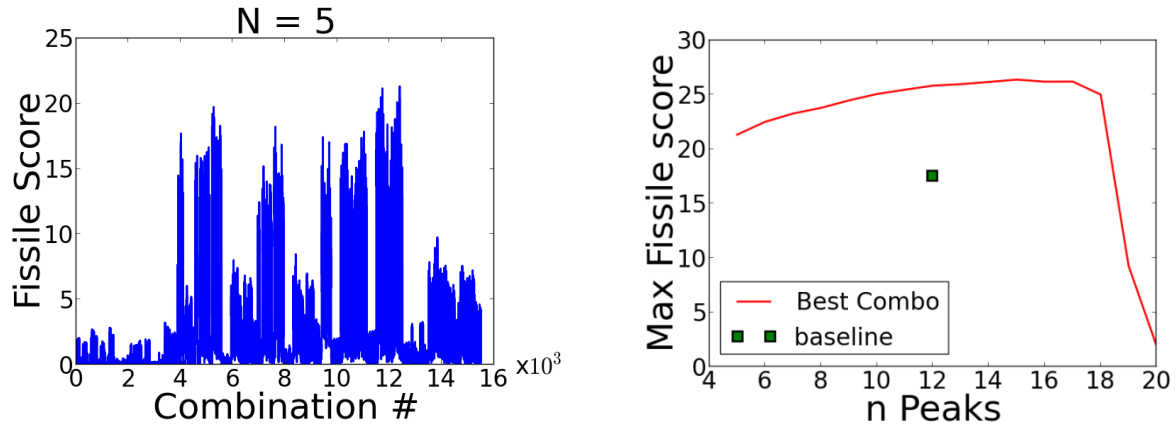

Figure A2. $S_{fissile}$ for each combination of $n = 5$ peaks, calculated form the training set (left). $S_{fissile}$ as a function of n, compared to the baseline set of 12 peaks, calculated from the cross-validation set.

The top score is relatively flat up to $n = 18$, with the peak around $n = 16$. However, incorporating the last two peaks causes the score to fall off dramatically. The green square represents the score for the baseline set of 12 peaks. Thus the optimization provides a significant improvement in $S_{fissile}$ over the manually selected peaks. Figure A3 shows a Hinton plot of the top

combinations of peaks, with the area of each square weighted by the $S_{fissile}$ in Figure A2 (right). Two peaks (3.055 and 3.250 MeV) are always absent. These two peaks do not significantly degrade the accuracy but substantially increase the uncertainty in the predicted fissile composition, suggesting that they are likely contaminated with noise from other sources.
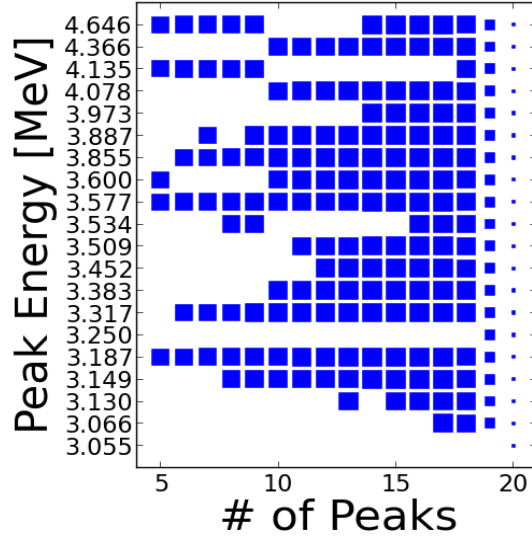

Figure A3. Hinton plot of the best combination of peaks as a function of n peaks. Areas are weighted by the best $S_{fissile}$ for each n.

A combination of 16 peaks providing the best score was used in the rest of the DG response deconvolution procedure. The predicted fissile isotopic fractions are plotted against the known test set of SFL#2 assemblies in Figure A4 for 15 and 30 GWd/MTU burnups. Each enrichment and cooling time has a group of points plotted against the predicted fissile content of the simulation. This group represents the different neutron source and detector positions that were part of the test set. On the left side of each group of points (x) are the predictions from the baseline set of 12 peaks. On the right side of each group (o) are the predictions for the optimized n = 16 peaks.

However, there is no drastic qualitative difference between the two sets. The improvement in the fissile score uncertainty is represented by the average relative error decrease from 4.2% to 3.5%, and on close examination the optimized set provides a relatively better fit.
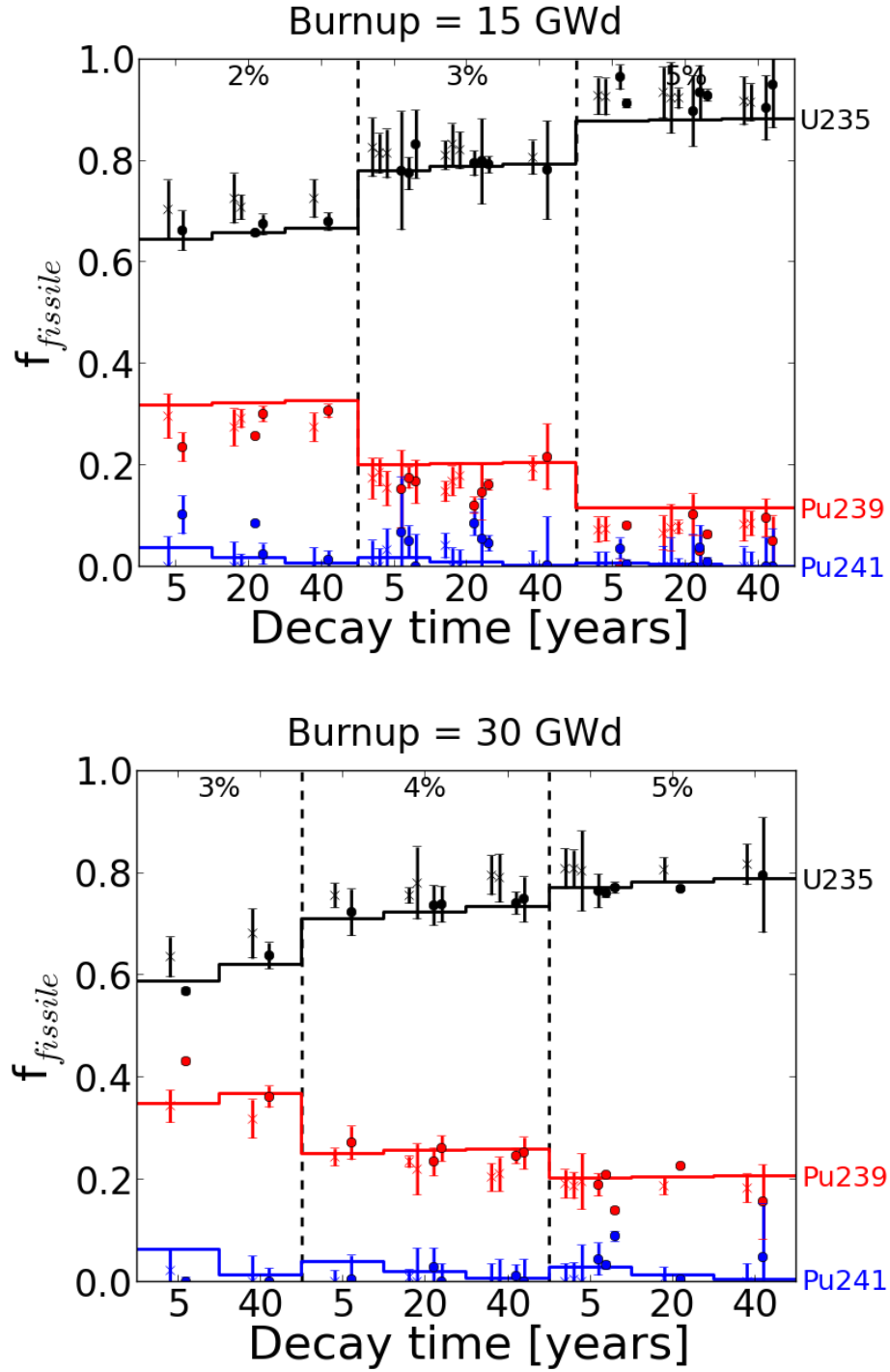
Figure A4. De-convolved fissile isotope fractions comparing the optimized set of 16 peaks and the baseline set of 12 peaks. The "x" markers represent results obtained with the 12 peak baseline set for each burnup, enrichment, and cooling condition. The "o" markers in each group represent results for the optimized set of 16 peaks.

Fresh and Spent Fuel Basis

The fresh fuel basis uses 6 reference assemblies, 4 LEU with enrichments of 2, 3, 4, 5%, and 2 MOX assemblies. The calculated fissile isotopic fractions are compared to the simulations in Figure A5 for burnup of 30 GWd/MTU in the test and cross validation sets.

The error bars for the fresh fuel basis are quite large, on the order of 30-60% absolute for U-235 and Pu-239. The fresh fuel alone in this selected calculation scheme does not provide a sufficient basis for good isotope identification.
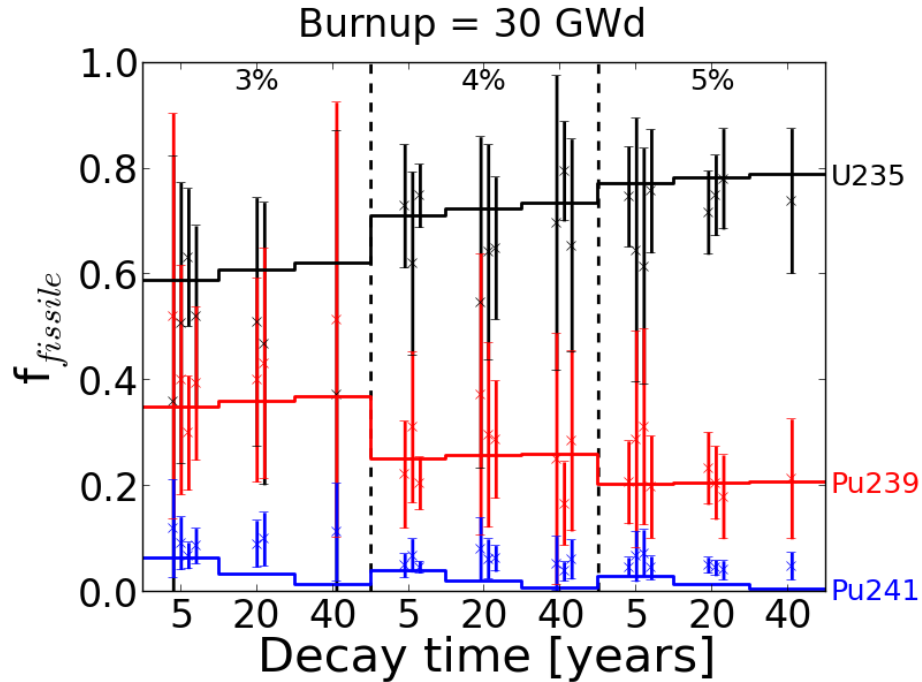

Figure A5. Fissile isotope fractions calculated with the fresh LEU and MOX fuel calibration basis have large uncertainties.

A calibration basis incorporating both fresh and "known" spent fuel assemblies provides the way to improve the de-convolution result. A "working standard" calibration set is selected from the 6 fresh LEU and MOX fuel assemblies and 27 spent fuel combinations of enrichment, burnup, and cooling times from SFL#2. Neutron generator and detector positions for the calibration spent fuel assemblies were chosen randomly. Initially different numbers of assemblies were to be explored, but n = 5 provided sufficiently good results. The cross-validation and test sets were therefore combined for the data comparison.

The comparison to simulation data for 15 and 30 GWd/MTU is shown in Figure A6. The top segment of the plots shows the total U-238 fraction. The bottom segment shows the fissile fraction of U-235, Pu-239, and Pu-241. The best combination of assemblies selected on the basis of $S_{fissile}$ is listed in Table A1. The top $S_{fissile}$ was approximately 40, suggesting average errors of approximately 1.8%.
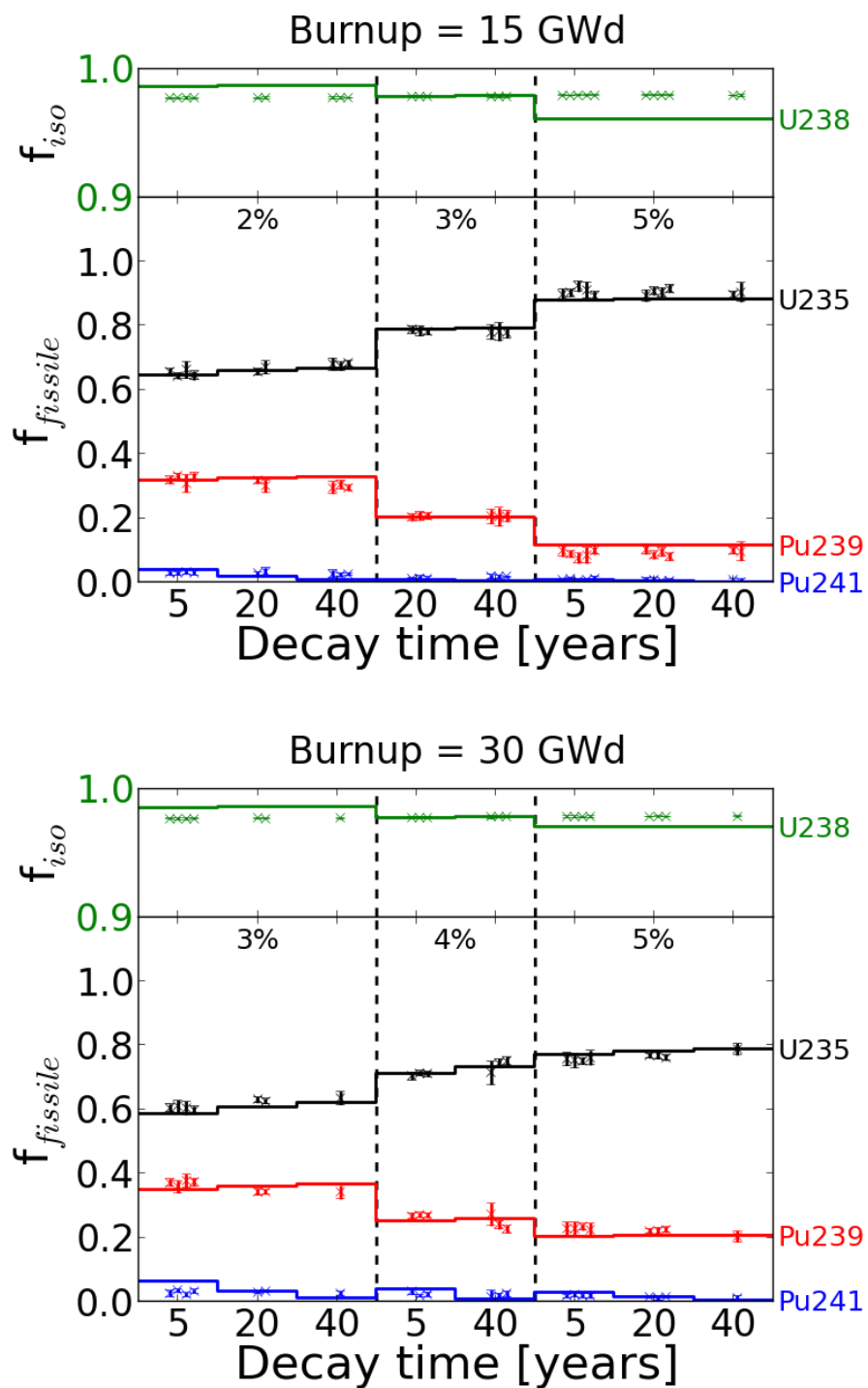
Figure A6. Fissile isotopic fractions are shown in the lower segment and the total U-238 fraction in the upper segment of each plot for the best combination of 5 reference assemblies.

Table A1. Best combination of fresh and spent fuel assemblies.

SFL#2 Assembly
2% fresh
3%, 15 GWd, 5 yr
4%, 30 GWd, 20 yr
5%, 45 GWd, 20 yr
5%, 45 GWd, 40 yr

It is surprising that the spent fuel basis outperformed the pure isotopic basis. The reason for the difference in performance is unclear, but is likely due to the signal basis being derived from a single assembly. It is possible that the use of an isotopic basis from a single assembly does not fully account for differences in self-attenuation or contributions from other isotopes besides the 4 of interest.

The top S_{all} was approximately 400, which means that the prediction in the U-238 content is accurate to about 0.2%. Because the U-238 is the dominate component of the assembly fissionable content and score is measured against an absolute error, S_{all} is biased and primarily reflects the accuracy in the U-238 relative content determination. The fresh and spent fuel basis outperforms the pure isotopic basis by approximately 2 orders of magnitude, likely for similar reasons previously discussed. However, it also seems the de-convolution is insensitive to the U-238 fraction across different enrichments, and it may be accurate only because the original basis assemblies all contained roughly the same amount of U-238.

Spent Fuel Library 4 results

The results for Spent Fuel Library #4 are calculated using 16 peaks and the 5 fresh and spent fuel basis assemblies determined in the above optimization routines. Since the exact compositions are left unknown, the de-convolution only results are shown in Figure A7 for the 36 SFL#4 assemblies.
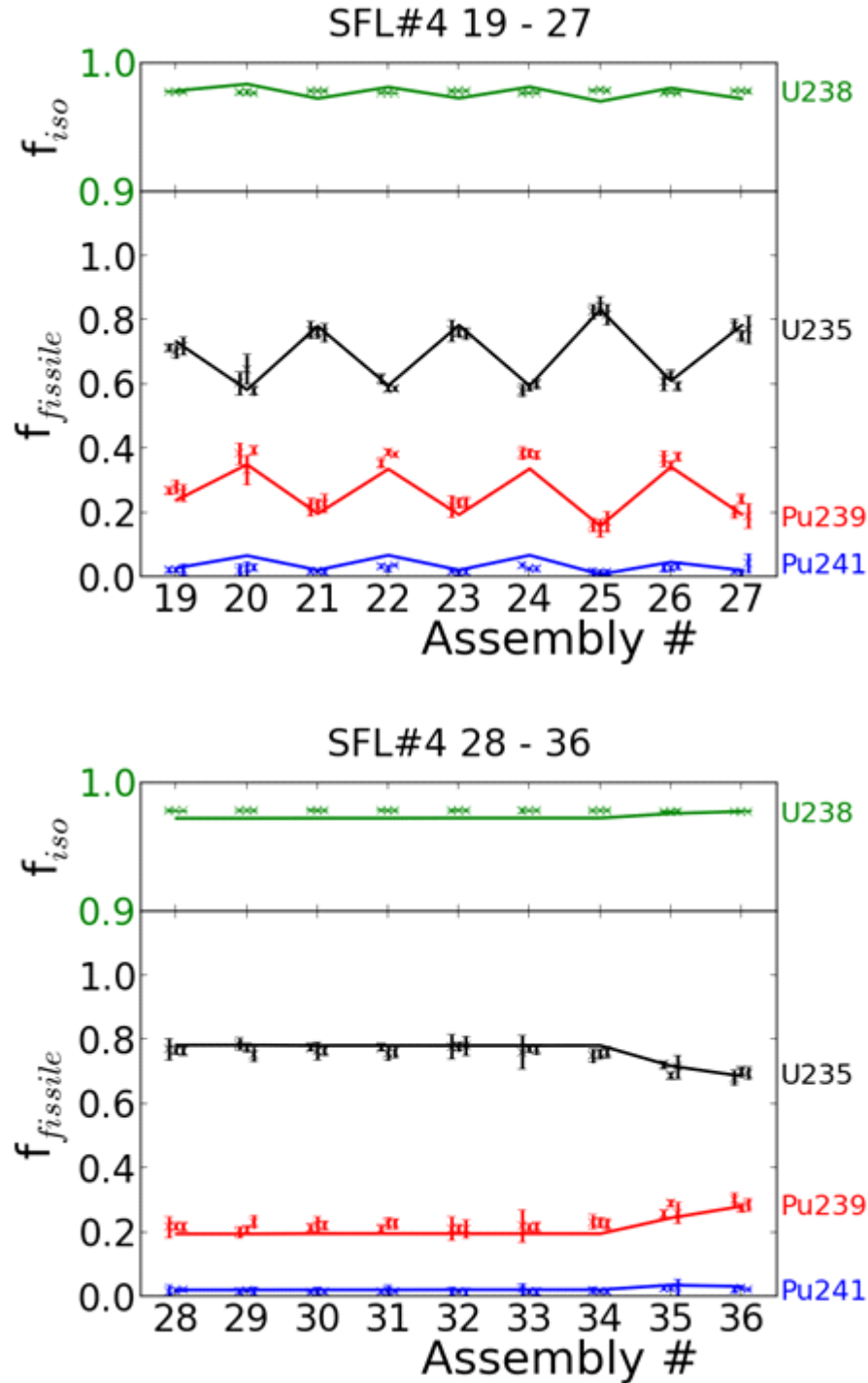
SFL#4 1 - 9

SFL#4 10 - 18

101
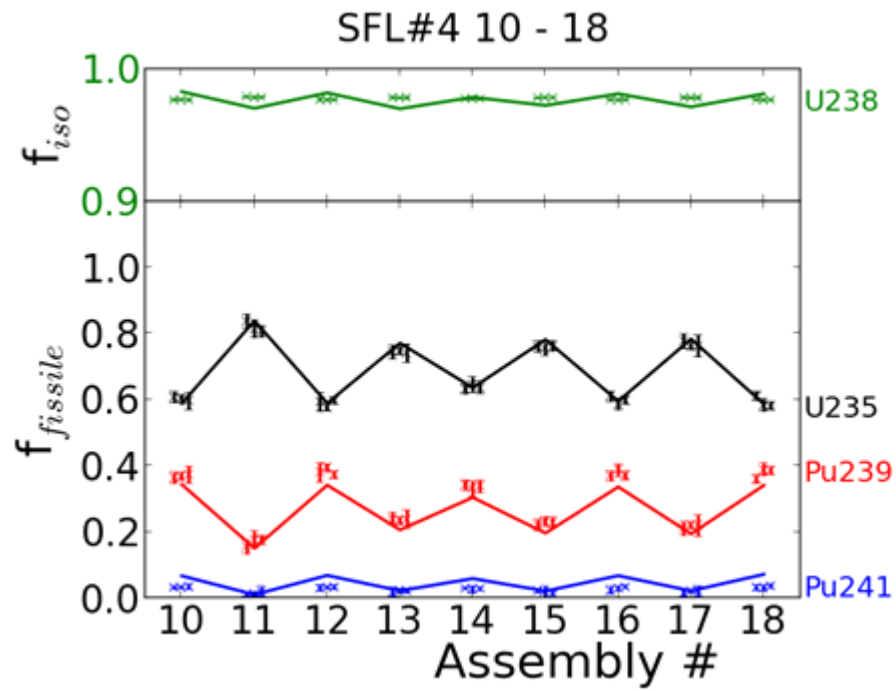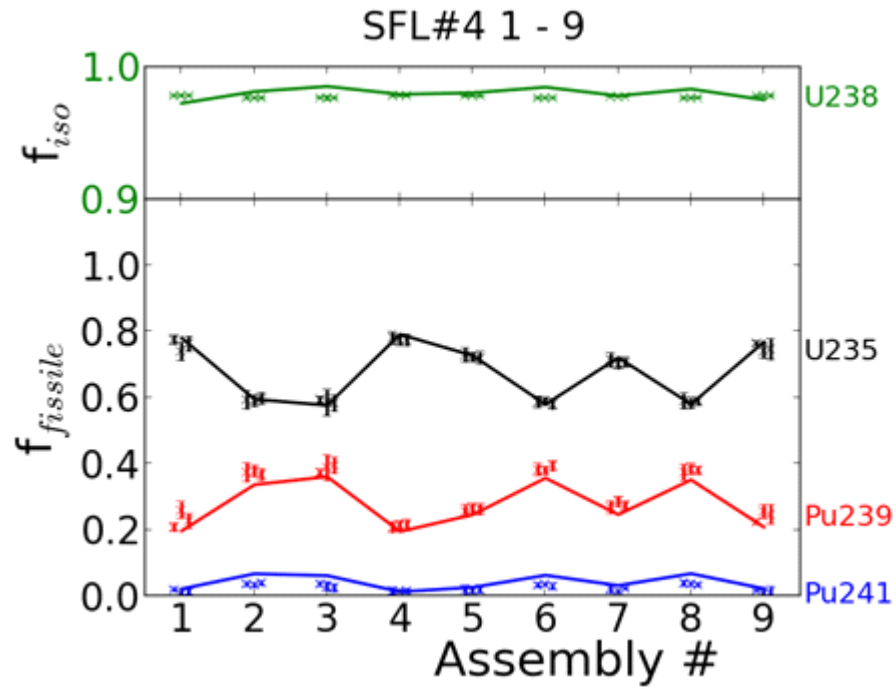
Figure A7. De-convolution results for the fissile isotopic fractions and U-238 fraction for each of the 36 assemblies in SFL#4.

References

[A1] H.W.Kuhn, A.W. Tucker, "Nonlinear programming," *Proceedings of 2nd Berkeley Symposium.* Berkeley: University of California Press. pp. 481–492, MR47303 (1951). Retrieved at http://projecteuclid.org/euclid.bsmsp/1200500249